

## Master Thesis

Thor Hvid-Olsen

# Hybrid Double-Nanowire Devices

Fabrication and characterization of Double-Nanowire Hybrid Devices

Supervisor: Associate Professor Kasper Grove-Rasmussen

Handed in: October 1, 2021

---

## Abstract

Parallel Double Nanowires coupled to superconductors could be applied for various experiments, including Majorana zero mode detection,<sup>25,68,71</sup> Cooper pair splitting,<sup>5,45,50</sup> and topological Kondo effect investigations.<sup>11</sup>

In this thesis, Parallel InAs Double Nanowires with epitaxially grown superconducting Al is used as the base of device fabrication, applying electron lithography in combination with metal deposition and selective Al etching. Following the fabrication, the devices are measured and analyzed. The thesis involves DNW Josephson Junctions, DNW Island Devices and DNW Little-Parks devices.

The measurements of the DNW Josephson Junction devices shows phenomena, such as multiple Andreev reflections (MAR) and Fabry-Pérot oscillations. Furthermore supercurrent is found to run through both of the parallel Nanowires in the Junction. From the MAR, the superconducting gap is estimated,  $\Delta = 150_{-50}^{+30} \mu\text{eV}$ .

The DNW Island devices are characterized, and shows superconductivity in terms of even-odd parity oscillations. The parity oscillations is found to be dependent on temperature and magnetic field. This dependency is attributed to quasiparticle excitations, and the parity oscillations are modelled, using a model from a similar device, based on a single nanowire, from Higginbotham et al.<sup>39</sup> From the model, a rough estimation of the superconducting gap  $\Delta = 180 \mu\text{eV}$ , the energy of the bound state, related to the quasiparticle excitations,  $E_0 = 30 \mu\text{eV}$ , and the lower bound for the poisoning time  $\tau_p > 1 \text{ms}$ , is extracted.

To conclude, this thesis adds to the understanding of the complexity in fabricating, and the physical phenomena in, DNW hybrid devices, a platform with promising perspectives.

---

## Acknowledgements

First of all, I would like to express my deepest appreciation to my supervisor, Kasper Grove-Rasmussen, for taking me in as a MSc student and supervising me throughout the thesis work. I would also like to extend my deepest gratitude to Alexandros Vekris, for being my primary teacher in the fabrication process and for always being available for questions and discussions, oftentimes with the appreciative start of the answer "That's a very good question".

I would like to extend my sincere gratitude to Jesper Nygård, for accepting me into his scientific group and always showing sincere interest in the current state of the thesis project. I also had a great pleasure working with Juan Carlos Estrada Saldaña, who were always ready to add ideas and share his own experience. Furthermore, I would like to acknowledge Thomas Kanne, for his work on Double Nanowire growth that laid the foundation for this thesis project.

In addition, I would like to thank Dennis V. Christensen, for always having a project ready if needed during my education, and my parents, for teaching me to enjoy learning. Lastly, I would like to thank my family, friends and Kirstine for their love and support.

---

## List of Abbreviations

A: Anisole	I: Insulator
ABS: Andreev bound state	InAs: Indium Arsenide
Al: Aluminum	IPA: Isopropanol
AR: Andreev reflection	JJ: Josephson junction
BCS: Bardeen–Cooper–Schrieffer	LPT: Local pair transport
CAR: Crossed Andreev reflection	MAR: Multiple Andreev reflections
CB: Coulomb blockade	MBE: Molecular Beam Epitaxy
CBE: Chemical Beam Epitaxy	MIBK: 4-Methyl-2-pentanone
CC: Corner to Corner	MZM: Majorana zero mode
CPS: Copper pair splitting	NDC: Negative differential conductance
DAC: Digital to analogue converter	NFL: Non-Fermi liquid
DMM: Digital multimeter	NMP: N-Methyl-2-pyrrolidone
DNW: Double nanowire	NW: Nanowire
DOS: Density of States	o: Odd
e: Even	PMMA: Poly(methyl methacrylate)
EBL: Electron Beam Lithography	QD: Quantum dot
EL: Ethyl lactate	S: Superconductor
EPR: Einstein-Podolsky-Rosen	SEM: Scanning Electron Microscope
FF: Facet to facet	SET: Single-electron transistor
FWHM: Full width half maximum	SNW: Single nanowire
GPIB: General Purpose Interface Bus	SO: Spin-Orbit
GS: Ground state	TEM: Transmission Electron Microscope
HQD: Hybrid quantum dot	TNW: Triple nanowire.

---

# Contents

<b>1</b>	<b>Introduction</b>	<b>7</b>
1.1	Double-Nanowire Motivation . . . . .	7
1.2	Thesis Outline . . . . .	7
<b>2</b>	<b>General Theory</b>	<b>9</b>
2.1	Semiconducting Nanowires . . . . .	9
2.2	Superconductors . . . . .	10
2.3	Quantum dots . . . . .	10
2.4	Hybrid Devices . . . . .	12
2.4.1	Superconducting Proximity effect . . . . .	13
2.4.2	Andreev reflections . . . . .	13
<b>3</b>	<b>Double-Nanowires</b>	<b>14</b>
3.1	The story of Double Nanowires . . . . .	14
<b>4</b>	<b>Fabrication &amp; Experimental setups</b>	<b>18</b>
4.1	The hybrid double-nanowire geometry . . . . .	18
4.2	Nanowire growth . . . . .	20
4.3	Nanowire deposition . . . . .	21
4.4	Electron Lithography . . . . .	24
4.5	Aluminum etching . . . . .	26
4.6	Metal deposition . . . . .	27
4.7	Imaging . . . . .	28
4.8	Sample loading . . . . .	29
4.9	Dilution refrigerator . . . . .	31
4.10	Measurements . . . . .	32
<b>5</b>	<b>Double-Nanowire Josephson Junctions</b>	<b>36</b>
5.1	Motivational perspectives in Double-Nanowire Josephson Junctions . . . . .	36
5.2	Introduction to DNW Josephson Junctions . . . . .	37
5.3	Status on the field of Josephson Junction Devices . . . . .	38
5.4	DNW Josephson Junction Devices . . . . .	40
5.4.1	Fabrication of DNW Josephson Junction Devices . . . . .	40
5.4.2	Characterization of DNW Josephson Junction Devices . . . . .	40

---

5.5	Conclusion on DNW Josephson Junctions . . . . .	44
<b>6</b>	<b>Double-Nanowire Islands</b>	<b>45</b>
6.1	Motivational perspectives in Double-Nanowire Island devices . . . . .	45
6.2	Introduction to SNW Island devices . . . . .	46
6.3	Status on the field of Island devices . . . . .	47
6.4	Quasiparticle excitations . . . . .	47
6.5	Majorana Islands . . . . .	53
6.6	Double-Nanowire Island Devices . . . . .	58
6.6.1	Fabrication of DNW Island Devices . . . . .	59
6.6.2	Characterization of a DNW Island Device . . . . .	59
6.6.3	Modelling of parity oscillations . . . . .	64
6.6.4	Information in the model . . . . .	68
6.6.5	The critical magnetic field . . . . .	71
6.7	Conclusion on DNW Islands . . . . .	72
<b>7</b>	<b>Conclusion and outlook</b>	<b>74</b>
	<b>Appendices</b>	<b>76</b>
A	Fabrication . . . . .	76
A.1	Recipes . . . . .	76
A.2	Fabrication steps . . . . .	84
A.3	Ready Decices . . . . .	87
B	Additional data on DNW Josephson Junctions . . . . .	88
B.1	Gatesweep of the Josephson junction . . . . .	88
B.2	Additional linecuts in 2-terminal voltage bias . . . . .	88
B.3	Additional 4-terminal current bias spectra . . . . .	89
B.4	Josephson junctions publication . . . . .	89
C	Additional data on DNW Island Devices . . . . .	99
C.1	Grouping of zero-bias conductance peaks by coupling . . . . .	99
C.2	Zero-bias peaks conductance peaks . . . . .	100
	<b>References</b>	<b>100</b>

---

# 1 Introduction

## 1.1 Double-Nanowire Motivation

Topological superconductivity is under extensive study, as it opens up for the new states of non-Abelian, thus not fermionic nor bosonic, behaviour. A wide range of systems capable of containing such topological superconductivity have been proposed, amongst these are hybrid systems, in the interface between semiconductors and superconductors.<sup>30</sup> Amongst such interfaces, semiconducting 1-dimensional nanowires (NWs) coupled to superconductors are predicted to access the topological phase and produce Majorana zero modes (MZMs),<sup>54,63</sup> which is one type of such non-Abelian states. A major complication in measuring MZMs however, are the similarities between their signatures and those of Andreev bound states (ABSs), which arise in very similar conditions.<sup>30</sup> This resemblance has made it difficult to conclude whether or not MZMs have actually been observed. Arising from the interest of transitioning into the topological phase, theoretical investigations into NW-superconductor interfaces has yielded how two parallel NWs coupled by a superconductor, results in destructive interference between direct and crossed Andreev reflections. Andreev reflections are explained in Sec. 2.4.2. This yields a decrease in the necessary conditions for entering the topological phase, the topological threshold.<sup>68,71</sup> Furthermore, supercurrent running in the superconductor coupling the two NWs was found to decrease the topological threshold event further.<sup>25</sup>

In addition to MZM experiments, other investigations are well-suited for the DNW hybrid setup. This includes Cooper pair splitting experiments, with the purpose of producing and isolating entangled states,<sup>5,45,50</sup> investigations into parafermions,<sup>47</sup> island devices potentially showing topological Kondo effect,<sup>11</sup> and Little-Parks fluctuations.<sup>84</sup>

Thus, I find the hybrid DNW setup relevant to study, why this thesis aim to gain further understanding of the different phenomena that can happen in these setups. This includes fabrication and characterization of different devices, based on such hybrid DNW structures, as well as further analysis of transport properties, such as AR phenomena and quasiparticle excitation.

## 1.2 Thesis Outline

**Chapter 2** introduce some background information necessary to have a thorough understanding of the concepts introduced in the following chapters. This includes theory about semiconducting NWs, superconductors, quantum dots and hybrid systems.

**Chapter 3** presents the state of the art of Double-Nanowires, including some theoretical perspectives, but mainly experimental accomplishments.

**Chapter 4** explain the processing pathways used to fabricate the devices that are measured and analysed in this

---

thesis. The chapter furthermore, explains the measurement setup and procedure.

**Chapter 5** describes the part of the thesis that focuses on DNW Josephson Junctions (JJ). First, a motivation for these sort of devices is presented, then a brief introduction to the JJ is described. Later a recent SNW JJ analysis is presented, followed by a description of how the DNW JJ were fabricated. At last, an analysis of the DNW JJ is presented and a conclusion of the important aspect extracted is described.

**Chapter 6** describes the part of the thesis that focuses on DNW Island devices. First, a motivation for this type of devices is presented, then a brief introduction to Island devices is described. Then the state of the art of Island devices is presented, followed by a description of how the DNW Island device were fabricated. At last, an analysis of the DNW Island device is presented and a conclusion of the important aspect extracted is described.

**Chapter 7** concludes the thesis, describing the central information gained during this thesis. Furthermore the chapter outlines perspectives that could be relevant for further studies.



---

## 2 General Theory

In this chapter I will introduce the theoretical background for the thesis. This includes Semiconducting Nanowires, described in Sec. 2.1, Superconductors, described in Sec. 2.2, Quantum dots, described in Sec. 2.3, and at last Hybrid Devices, described in Sec. 2.4.

### 2.1 Semiconducting Nanowires

Nanowires (NWs), as illustrated in Fig. 2.1a) are 1-dimensional structures, with two of the spatial directions being on the nanoscale and the the third extending far longer. This results in a structure, where charge carriers in the two short directions are altered by quantum mechanics, confined by the NW size relative to the de Broglie wavelength of the charge carrier, while they are free to travel in the third direction. In this thesis, the NWs are all made from semiconducting InAs.

The reason for a semiconducting material, such as InAs, to be well-suited for experimental use of NWs is the tunability of semiconductors, using an electrostatic gate. This allows one to define regions in the NW where transport of charge-carriers is blockaded or promoted. The standard hexagonal InAs NW are grown in a wurtzite structure along the [0001]-direction from an InAs [111]B substrate, they tend to be 60-100 nm in diameter and 5-10  $\mu\text{m}$  long.<sup>49</sup>

The choice of InAs for the NWs are based on multiple reasons. First, the effective mass of electrons in InAs is very low<sup>60</sup> resulting in a large spacing between energy levels,<sup>33</sup> second, the amount of lattice defects achievable is relatively low,<sup>88</sup> resulting in high mobilities,<sup>19</sup> third, relatively low contact barriers can be achieved,<sup>74</sup> fourth, the narrow bandgap<sup>59</sup> limits the amount of applied voltage necessary on the gates and last, InAs has a large spin-orbit (SO) coupling<sup>28</sup> and a high g-factor,<sup>17</sup> making it a good candidate material for topological phase transitions.<sup>30</sup>

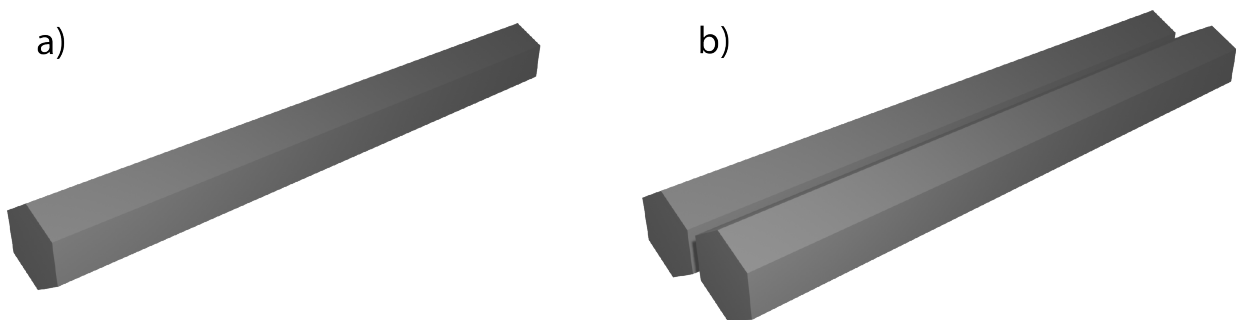


**Figure 2.1: From single to double nanowires.** a) displays a single nanowire. b) displays the parallel double nanowire system described in this thesis.

---

As depicted in Fig. 2.1b) however, the focus in this thesis is on the, to date, relatively new area of parallel double nanowire (DNW) systems.

## 2.2 Superconductors

Superconductivity is the phenomenon of electrical conductance without any resistance. The mechanism for this phenomenon, described by Bardeen, Cooper and Schrieffer,<sup>7</sup> is that two electrons, of opposite momentum and spin, couple into what is called Cooper pairs. The attractive force in-between the electrons, causing the coupling is originated in lattice interactions with the electrons.<sup>76</sup> This is illustrated in Fig. 2.2a). Conceiving the Cooper pairs as being particles, the sum of the electron spin equals an integer making them boson.

Thus, they do not obey Pauli's exclusion principle and they are allowed to group together at a single energy level, the Fermi level as illustrated in the density of states (DOS) plot in Fig. 2.2b). Here the distance to the continuum is the superconducting gap,  $\Delta$ . Thus to add a single electron to a superconductor the energy  $2\Delta$  is needed.<sup>10</sup>

To measure superconductivity one needs specific materials, such as Al used in this thesis, at temperatures below the critical temperature,  $T_C$ , of the material (for Al  $T_C = 1.2\text{K}$ <sup>16,26,57</sup>) as displayed in Fig. 2.2c), in relation to a normal metal. Additionally, if a magnetic field is applied, superconductivity is suppressed at critical magnetic field,  $B_C$ . The relation between the superconducting state and the magnetic field and temperature is visualized in Fig. 2.2d).

Decreasing the volume of superconductor penetrated by magnetic field, decreases  $B_C$ . Thus, a  $B_C$  parallel to a NW covered with superconductor will be larger than if it were applied perpendicularly, as less magnetic field lines penetrate the superconductor in the parallel configuration.<sup>78</sup> Additionally, limiting the thickness of such superconductor can increase  $B_C$  significantly.

Two types of superconductors exist, type I and II. Type I works as a perfect diamagnet, thus repelling the magnetic field by creating opposite spins, this is called the Meissner effect in superconductivity. In this thesis, only type I has been applied why I will not describe type II.

## 2.3 Quantum dots

A quantum dot (QD) is a conducting 0-dimensional entity, meaning that it is confined in all three spatial directions. These can be made by gating a 2-dimensional system, such as an electron gas, by patterning of metal, or by creating barriers in a 1-dimensional, such as in NWs using. Barriers in NWs is achievable through gating, by crystal-phase engineering of growth<sup>12,24,62</sup> or by introducing other crystal layers than the main NW structure, as InP barriers in InAs NWs.<sup>77</sup> To achieve, what is called a single electron transistor (SET), which is such a QD

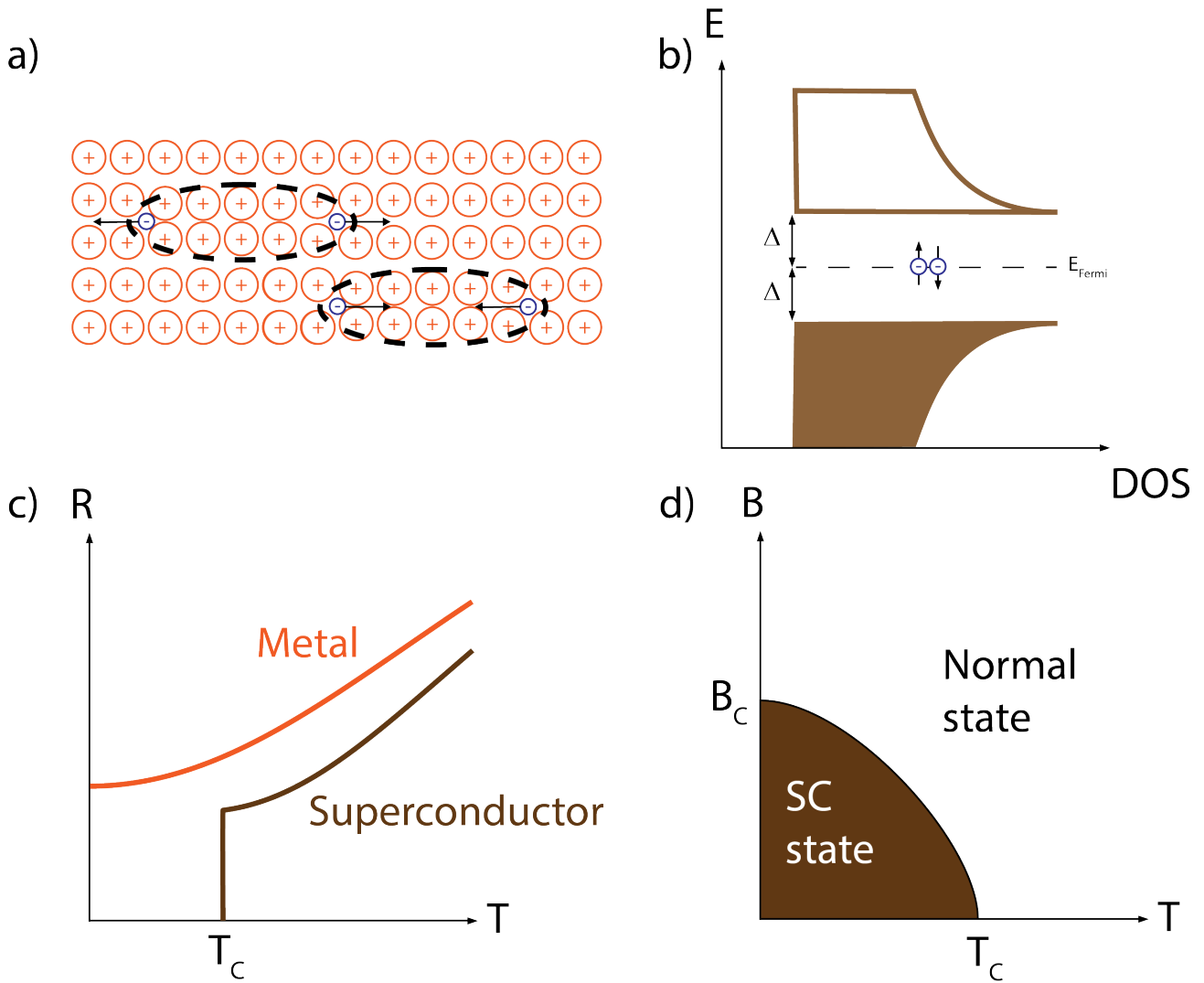


**Figure 2.2: Superconducting features.** a) is a schematic of the lattice effects giving rise to Cooper pairing. The positive ions in the lattice bends towards the electrons due to attraction, causing the electrons to attract each other through the local increase of positive charge in the lattice. b) is the density of states (DOS) of a superconductor with respect to energy.  $\Delta$  is the superconducting gap and  $E_F$  the Fermi energy. c) displays the resistance (R) as a function of temperature for a superconductor and a metals and d) shows the superconducting regime in temperature and magnetic field.  $B_C$  is the critical magnetic field and  $T_C$  is the critical temperature.

coupled to a metallic source and a drain capable of allowing a single charge to pass through, as displayed in Fig. 2.3, Coulomb blockade between the QD and the leads is needed. To have Coulomb blockade, as illustrated in Fig. 2.4, three demands are needed:

$$k_B T < E_{\text{Add}} \quad (2.1)$$

$$R > h/e^2 \quad (2.2)$$

$$V_{\text{SD}} < e/C \quad (2.3)$$

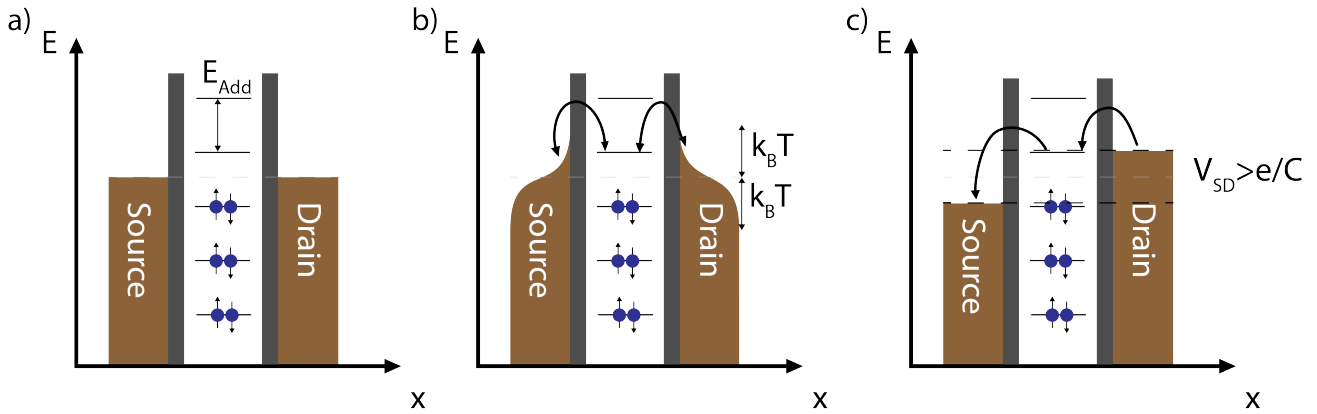


**Figure 2.4: Coulomb barrier conditions.** Schematic of the transport through a SET. a) displays the system in Coulomb barrier, with no transport. b) displays the system with the thermal energy exceeding the addition energy. c) is the system with resistances too low to uphold the second condition (Eq. 2.2 and d) displays the system with bias voltage exceeding the level spacing.

The first condition describes that the thermal energy must be much lower than the Addition energy,  $E_{Add} = E_C + \Delta\epsilon$ .<sup>36</sup> Here  $E_C$ , the charging energy depends on the self-capacitance,  $C$ , of the QD,  $E_C = e^2/C$  and  $\Delta\epsilon$  is the level spacing on the QD. Since  $C = C_C + C_g + C_D$ , as depicted in Fig. 2.3, this limits the size of the island to achieve a low capacitance. In semiconducting QDs, quantized levels, with level spacing,  $\Delta\epsilon$ , can arise. In metals, a continuum of levels are available, why these systems, called islands, does not have a  $\Delta\epsilon$  thus  $E_{Add} = E_C$ . The case where the first demand is not achieved is depicted in Fig. 2.4b), Here it is visible how the thermal energy distributes the DOS in the metal leads. Regarding the second condition, the charging of the island takes time  $\Delta t = RC$ . Given Heisenburg's uncertainty principle we know that  $\Delta E \Delta t > \hbar$ . Since  $\Delta E = E_C$  in this case, we get the condition.<sup>42</sup> Third and last, the bias potential should not exceed the elementary charge over the self capacitance of the island, as this would mean that the bias potential facilitates energy enough to add an electron to the island. This is shown in Fig. 2.4c)

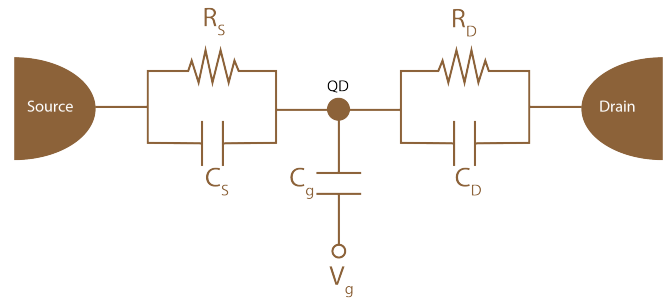


**Figure 2.3: Single electron transistor.** Schematic of the circuit of a single electron transistor. The QD in the middle are coupled to the source and drain through what can be understood as a capacitor and resistor in parallel.

## 2.4 Hybrid Devices

A device based on the combination of different classes of materials (metals, semiconductors, superconductors, etc.), is called a hybrid device. These hybrid devices is made to utilize the fusion of the attributes, from each class of material, into novel features.<sup>9,15</sup> A particularly interesting feature, that can arise in semiconductors

with strong spin-orbit coupling coupled to superconductors, is the topological superconductivity. Especially the predicted embodiment of Majorana zero modes (MZMs), that are predicted in the ends of NW-based topological superconductors is of great interest to prove or refute.<sup>30</sup> In this thesis the focus is on DNW hybrid devices, meaning DNW structures combined with superconducting segments.

### 2.4.1 Superconducting Proximity effect

The proximity effect takes place in the interfaces between superconductors and normal metals or semiconductors, where Cooper pairs can spread into the normal metal, effectively making it superconducting. Likewise, the inverse proximity effect takes place in the superconductor, where the superconductivity around the interface somehow weakens. This weakening can be seen as a lowering of the critical temperature in an superconducting film compared to that of the bulk superconductor.<sup>14</sup>

### 2.4.2 Andreev reflections

In a normal metal-Superconductor (NS) junction, transport with bias potential at  $eV_{SD} < \Delta$  is possible. Since this, however occurs within the superconducting gap of the superconductor, it cannot happen through single electron transport. The process oftentimes mediating this is called Andreev reflections (AR).

In AR, an electron with spin- $\uparrow$  and momentum  $= \hbar k$ , as respectively displayed in real-space and energy-space in Fig. 2.5a) and b), is moving from N to S. This results in a Cooper pair being produced in the S. However, since the Cooper pair is comprised by two electrons of opposite spin and momentum, another electron with spin- $\downarrow$  and momentum  $= -\hbar k$  is necessary for this transition to take place. This is solved by the analogue particle, a hole with spin- $\downarrow$  and momentum  $= -\hbar k$ , being retroreflected.<sup>10</sup>

In an NSN junction, crossed AR (CAR) can arise. This is a phenomenon where the Cooper pair is comprised in the superconductor from the electron, with energy  $eV < \Delta$ , from the first N, and a hole with energy  $-eV$  and opposite spin and momentum compared to the electron.<sup>58</sup>

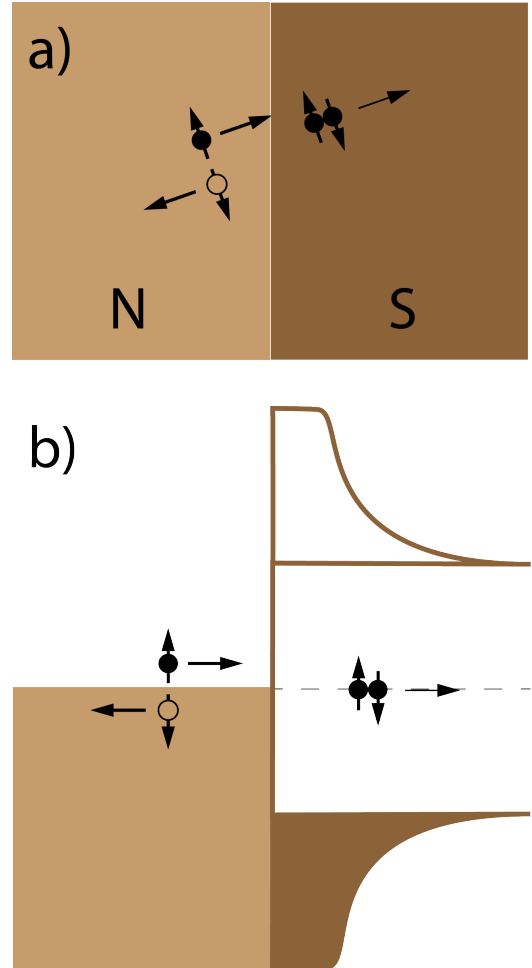


**Figure 2.5: Andreev reflections.** a) Real-space schematic of Andreev reflections. b) Energy-space schematic of Andreev reflections.

### 3 Double-Nanowires

In this chapter, I will chronologically present the research that has been conducted on parallel DNWs. I present both theoretical and experimental investigations, but focus mainly on the experimental ones.

#### 3.1 The story of Double Nanowires

Starting in 2014, Klinovaja et al.<sup>47</sup> presented a theoretical analysis, showing how dominating CAR, in a pair of parallel NWs coupled by a superconductor, supports pairs of parafermions.

In 2017, three studies on DNW systems were published. Baba et al.<sup>6</sup> reported on how they managed to fabricate and measure a device based on closely placed InAs NWs as depicted in Fig. 3.1. The device consisted of two parallel InAs NWs contacted with source and drain electrodes. They tuned it, using bottom finger gates, to form parallel double quantum dots with finite inter-dot coupling. By presenting the fabrication in this study, they laid the foundation for advanced experiments, that could potentially yield the observations of Majorana and Para Fermions.

The fabrication of the device by Baba et al.,<sup>6</sup> started by growth of the nanowire using Chemical Beam Epitaxy (CBE). The NW diameters ranged from 60 nm to 80 nm and the NW lengths from 2  $\mu\text{m}$  to 4  $\mu\text{m}$ . Using Transmission Electron Microscopy

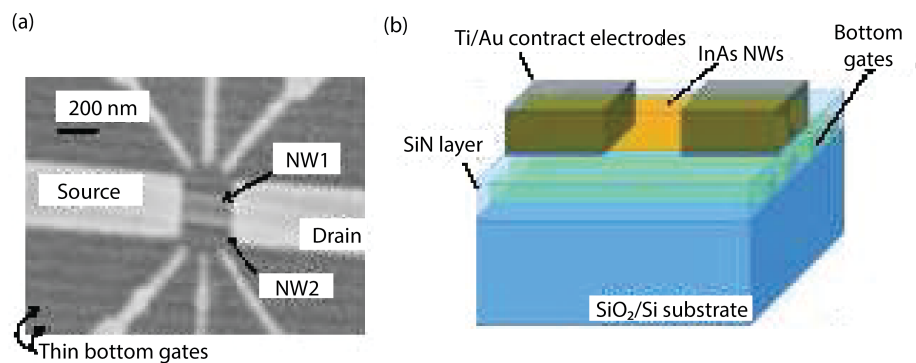


**Figure 3.1: Double-Nanowire device fabricated by Baba et al.<sup>6</sup>** SEM (a) and schematic (b) of a DNW double quantum dot junction device. The sidegates shown in (a) was not used in this particular study. Adapted from Baba et al.<sup>6</sup>

(TEM) they found a clean wurtzite structure structure of the DNWs, all grown along the  $\langle 111 \rangle$  direction perpendicular to the substrate surface.

The NW deposition step employed by Baba et al.,<sup>6</sup> started with transferring countless NWs, using a cotton bud, onto an intermediate substrate with layered PMMA on PVA films on top. On this intermediate substrate, bunched NWs were determinable as they exhibited a higher contrast in an optical microscope. Heating up the substrate allowed them to peel off the PMMA layer and attach it, NWs pointing downward, to a homemade micro manipulator. Then the film is contacted to the device substrate and precisely aligned, using the micro manipulator. Finishing the deposition, the sample was heated to 180 °C to improve the adhesion of the NWs and the PMMA film was removed using acetone.

In the last fabrication step, Ti/Au contacts were deposited after removing the insulating oxide layer on the InAs NWs by etching in  $(\text{NH}_4)_2\text{S}_x$  solution.

When measured, the charge stability diagram, as a function of applied voltage on the two finger bottom gates, showed resonance peaks of two different slopes. This indicated a parallel double quantum dot. Furthermore, greater tuning of the bottom gates yielded a regime displaying honey-comb like features, as a result of electrostatic coupling of the two quantum dots.

Reeg et al.<sup>68</sup> published a theoretical study on a parallel DNW system connected by a superconducting strip, yielding that direct AR and CAR interfere destructively. This, Schrade et al.,<sup>71</sup> in another theoretical study, found to cause a reduction in the topological threshold, corresponding to the magnetic field necessary to enter the topological phase, compared to the same situation for SNWs.

In 2018 Baba et al.<sup>5</sup> described an observation of Cooper pair splitting from a superconductor into two quantum dots each formed in one of two parallel DNWs.

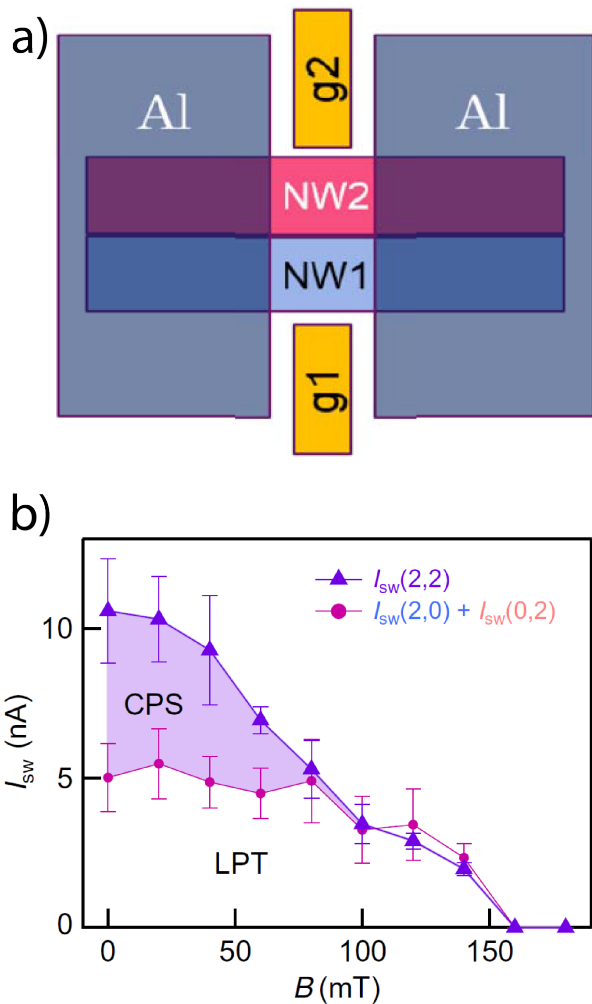


**Figure 3.2: Double-Nanowire Josephson Junction Cooper pair splitter.** (a) is a schematic of a DNW Josephson Junction device presented and (b) is the switching current,  $I_{sw}$  as a function of magnetic field,  $B$ .  $I_{sw}(2,2)$  emerge from both Cooper pair splitting and local pair transport,  $I_{sw}(0,2)$  and  $I_{sw}(2,0)$  emerge from only local pair transport through NW1 or NW2 respectively. Adapted from Ueda et al.<sup>45</sup>

The same year Thakurathi et al.<sup>56</sup> through a more microscopic theoretical approach, than done up until that point, verified the DNW hybrid system as a versatile platform for MZMs.

In 2019, Dmytruk et al.<sup>25</sup> published another theoretical study, providing information about how supercurrent, running through an superconductor that proximitizes two parallel NWs, lowers the topological threshold. This in addition to the destructive interference between CAR and direct AR, would lower this threshold significantly compared to SNW systems.

Furthermore, Ueda et al.<sup>45</sup> published a paper presenting data from a ballistic InAs/Al DNW Josephson Junction (JJ) device. In this paper they observed large Cooper pair splitting efficiency as a result of the electron-electron interactions connected with transport through only one wire. Furthermore, they found the relation between intra- and interwire superconducting gap to suggest the possibility of MZMs at zero magnetic field in the hybrid InAs/Al geometry.

Figure 3.2a) shows a schematic of the DNW JJ, fabricated by Ueda et al.<sup>45</sup> Here the two NWs, NW1 and NW2, are closely spaced and covered with Ti/Al on each of the NW ends, leaving just a small junction

bare. Beside each bare NW segment, a Ti/Au gate is deposited. Measuring this ballistic InAs/Al DNW junction yielded Fig. 3.2b), displaying switching current,  $I_{SW}$ , for three different conductance plateau regions of the NWs.  $I_{SW}(m,n)$ , is the switching currents, where the resistance becomes finite, for  $m$  conducting channels through NW1 and  $n$  through NW2. In  $I_{SW}(2,2)$  both Cooper pair splitting (CPS) and local pair transport (LPT) takes place, while in  $I_{SW}(2,0)$  and  $I_{SW}(0,2)$  only LPT through NW1 and NW2 respectively takes place. The  $I_{SW}(2,2)$  transport process seems to be larger than the other two until the magnetic field reaches  $B = 80$  mT, where the Cooper pair splitting seems to cease. Up until this point the LPT is unaffected, but from  $B=80$ mT it starts to decrease until it reaches 0 at  $B = 160$  mT.

Jumping to 2021, Kanne et al.<sup>44</sup> presented a method to grow DNWs with epitaxially grown Al on the surface in either half or full shell *in-situ*. Later in 2021, Kütössy et al.<sup>50</sup> presented a paper describing the hybridization of electrons in two individually tunable parallel artificial atoms (QDs), based on the DNWs grown by Kanne et al.<sup>44</sup> Around the same time, Vekris et al.<sup>85</sup> published a paper on the Little-Parks effect in full-shell DNWs and another paper about DNW JJ Devices,<sup>84</sup> both papers based on the DNWs grown by Kanne et al.<sup>44</sup> Figure 3.3 displays one of the DNW JJ devices presented in the second-mentioned paper. In Fig. 3.3(a), a False-color SEM is displayed with green InAs NW, gray superconducting Al and gold Ti/Au contacts and gates. B-field direction is shown too. The inset illustrates the half-shell cross-section

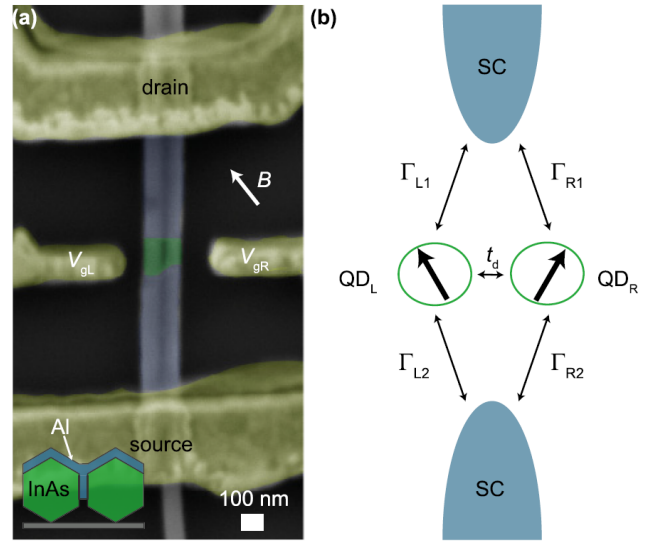


**Figure 3.3: Double-Nanowire Josephson Junction QD system.** (a) is a false-color SEM of a DNW Josephson Junction device presented and (b) is the corresponding model of the system in Coulomb blockade, with a left ( $QD_L$ ) and right ( $QD_R$ ) QD with interdot coupling  $t_d$  and QD-lead couplings,  $\Gamma_{L1,L2,R1,R2}$  between the dots and the superconducting leads. Adapted from Vekris et al.<sup>85</sup>

of the DNWs. Figure 3.3(b) shows the model they used to describe the system. Here two superconductors are separated with two parallel QDs,  $QD_L$  and  $QD_R$ , in between. Each superconductor is coupled to each QD, with coupling,  $\Gamma_{L1,L2,R1,R2}$ . In addition, the QDs have an interdot coupling,  $t_d$ .

Vekris et al.<sup>85</sup> found an effective tunability of the QD ground states as well as an upper bound on  $t_d \leq 50 \mu eV$  for the charge states they studied in one device and the same order of magnitude for the lower bound in another device. Thus providing the foundation to utilize the system for more advanced experiments, such as Cooper pair splitting and topological kondo effect measurements.<sup>85</sup>

From this overview of the research on parallel DNW hybrid devices, I find research into this sort of devices important, due to the potential features of the system. Adding to the foundation towards the technological utilization in Cooper pair splitting as well as the proof or refutation of Majorana zero modes, would be of great



---

interest for the scientific community. Thus, the potential application of *in-situ* grown DNW hybrid devices in experiments relevant for these two long-term goals, is studied.

## 4 Fabrication & Experimental setups

In this chapter I will first introduce the DNW hybrid device structure, then I will explain the general pathway used to fabricate the devices. Exact fabrication instructions are noted in Appendix A.2 and practical details are included in the chapter to help future students enter the field quickly. Furthermore, I will explain typical measurement tools applied in the extraction of data from same devices.

### 4.1 The hybrid double-nanowire geometry

The DNW geometry is described by multiple parameters. First thing to mention is that this thesis limits the focus on parallel DNWs. Thus, some of the important parameters is the diameter and length of the NWs, the distance between the NWs the relative orientation of the NWs, and, because we focus on hybrid structures, how much of the NWs the superconductor, in this thesis Al, cover. In Table 4.1, a list of the samples, chips with one or more devices, are presented. In the top row, multiple parameters are denoted, all of which I will start by explaining. Afterward, I will briefly introduce the different samples I have worked with. both in fabrication and in characterization.

Sample number	Sample name	Al coverage	Growth sample	Dot count	NW spacing (nm)	Orientation	Device type	Status
1	898 sample 9-3-20	Full-shell	Qdev898	Miscellaneous	Miscellaneous	Miscellaneous	Islands	Fabricated and measured, not conducting
2	Parks2	Full-shell	Qdev898	3-5	140-160	6 FF 4 CC	Little-Parks	Discarded
3	Parks3	Full-shell	Qdev898	4-5	140-160	CC	Little-Parks	Discarded
4	Parks4	Full-shell	Qdev898	4	160	CC	Little-Parks	Fabricated, ready for measurement
5	CC1	No Al	Qdev905	10 and 20			SNW Quantum dots	Discarded
6	CC2	No Al	Qdev905	16, 25, 50			SNW Quantum dots	Fabricated, teaching material
7	CC3	No Al	Qdev905	10, 13, 16, 20			SNW Quantum dots	Fabricated, teaching material
8	JJ1	Half-shell	Qdev939	20	200-250	FF	Josephson junction	Analysed in Chapter 5
9	Q2	Half-shell	Qdev939	20	200	FF	Island	Analysed in Chapter 6
10	Q3	Half-shell	Qdev939	20	200	FF	Island	Analysed in Chapter 6

**Table 4.1: List of fabricated samples.** This table lists the samples I have fabricated throughout the project. The Qdev905 growth sample, used for CC1, CC2 and CC3 were a SNW growth substrate, and the CC samples were intended for teaching purposes thus not mentioned throughout this project. Sample number 8, 9 and 10 were fabricated by A. Vekris but analysed in Chapter 5 and 6. The conversion from Dot count to diameter is displayed in Fig. 4.3 for half-shell DNWs and Fig. 4.2 for full-shell DNWs.

**Sample number** and **Sample name** are defined to keep track on the different samples.

**Al coverage**, is quantised by the number of facets on the hexagonal NW that are coated by superconductor. Generally however, this thesis works with half-shell, corresponding to three coated facets on each NW, and full-

---

shell, corresponding to all six facets coated.

**Growth Sample** are the sample name, on where the specific DNWs, used for one of the samples presented in this thesis, are grown.

**Dot count** determines the diameter and length of the NWs. These values are settled in the growth phase, which will be introduced in Sec. 4.2. The dot count, is the amount of holes made in the resist layer with Electron Beam lithography (EBL), introduced in Sec. 4.4, before depositing Au, which catalyses the growth. Thus, for a set time of growth, increasing dot count result in thicker, shorter NWs.

**NW spacing** is the distance between the NWs in the DNW structure, and are measured from the center of the one NW to the other. This value are determined from the pattern drawn in the resist before the growth, that effectively determines the location of the Au particles.

**Orientation** of the NWs, relative to each other, is split into two extremes, facet-to-facet (FF) and corner-to-corner (CC). In FF orientation one of the facets of each NW point towards a facet of the other, while in CC orientation one of the corner of each NW point towards the corner of the other.

**Device type** denotes the type of device fabricated on the sample.

**Status** describes where in the fabrication and experimental process the respective sample is situated at the day of handing in the thesis.

From the prepared DNWs, either half-shell or full-shell, the fabrication steps towards creating measurable structures is conducted followed by the measurement of the ones, that are successfully created through all the procedures.

Sample 1 is a batch of full-shell DNW Island devices, the individual DNWs has varied dot count and nanowire spacing as well as relative orientation. It was measured to be not conducting.

Sample 2, 3 and 4 are full-shell Little-Parks devices with relatively low dot count, thus long and narrow. The spacing of sample 2 and 3 vary between 140-160 nm and sample 4 is all 160nm spaced DNWs. Sample 2 has 6 DNWs in FF orientation and 4 in CC orientation. Sample 3 and 4 is all CC DNWs. Sample 2 and 3 were discarded due to alignment issues in EBL and zero DNW yield, using the micromanipulator as described in Sec. 4.3, respectively. Sample 4 is ready for measurement.

Sample 5, 6 and 7 are single nanowire quantum dot devices fabricated for teaching purposes.

Sample 8, 9 and 10 were fabricated and measured by A. Vekris, I however took part in discussing the measurements from home (due to Covid-19 access restrictions), as well as analysing the data. These comprises Chapter 5 and 6. Sample 8 are half-shell Josephson Junctions with a relatively large dot count. The NWs are in FF orientation. Sample 9 and 10 are FF half-shell Island devices also with a relatively large dot count. Sample 9 with side gates, and 10 with top gates.

## 4.2 Nanowire growth

The InAs NWs used in this project are all grown from Molecular Beam Epitaxy (MBE), a bottom-up process where catalysts, in our case pairs of gold nanoparticles, is deposited on an InAs (111)B substrate,<sup>44</sup> using electron lithography (see section 4.4). Following the Au particle deposition, the substrate is placed in a pressurised chamber where it is exposed to Indium and Arsenic flux. The two elements aligns itself under the Au particles in layers and starts growing into nanowires with wurtzite crystal structure in the [0001]B direction, until the flux is stopped. Compared to SNW growth, NWs in DNW growth have a smaller amount of accessible adatoms due to the other NW being in close adjacency. Since the In is stronger bound in the NW growth, this smaller amount of accessible adatoms results in a larger effective V/III-ratio that increase the growth speed of DNWs compared to SNW. This effect can be counteracted by changing the fluxes.<sup>44</sup> Due to the vacuum pressure in the chamber, the process facilitates a very high purity compared to other methods that uses carrier gas. Furthermore, slow injection of the flux lowers the probability of stacking defects. After NW growth, the substrate was transferred *in-situ* into a metal deposition chamber. In this chamber aluminum is evaporated onto the NWs either forming full or half shells. This is done at a substrate temperature,  $T_{\text{sub}} \sim 120$  K and a deposition rate on  $\sim 3$  Å/s. These parameters is optimized to ensure a pristine NW-superconductor interface in addition to conserve a smooth and stable morphology.<sup>44</sup>

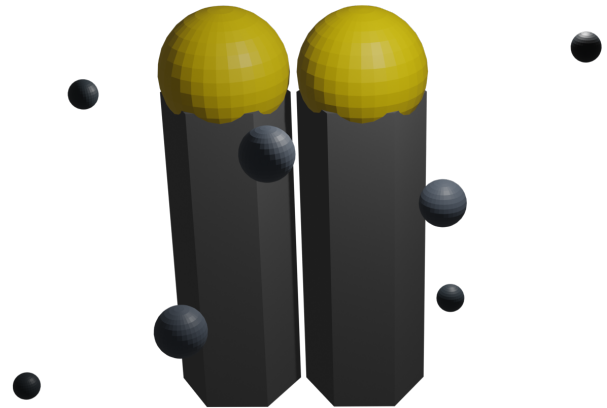


**Figure 4.1: Mechanism of MBE.** Graphical illustration of how In (bigger and lighter gray) and As (smaller and darker) builds themselves up into NWs under the Au particle.

In this project, two DNW growth substrates were used. One of the batches, the Qdev898, are full-shell wires and the other batch, the Qdev939, are half-shell wires. From the first-mentioned, Qdev898, we were handed a piece of the shape shown in Fig. 4.2a). As visualized in Fig. 4.2c) the repeating pattern is build up by two outer rows of five outer columns, with each cell consisting of four inner rows of three columns. Above the top outer row, to the left, are two rectangular areas that are used for navigation. The outer top row itself is defining the area where all DNWs are grown facet to facet, as shown in the right side of the row. Similarly, the outer bottom row is defining the areas of corner to corner DNW growth. In the first outer column, from the left, the DNWs are 1 dot, meaning that they were grown using one hole made with EBL before depositing Au for NW growth. The dot count increase by one for each column going to the right. In the inner rows and columns, a number is written in each cell. This number defines the NW spacing in nm. Thus, for the top inner row there's

---

three areas, one with 140 nm spacing, one with 150 nm spacing, and the last one with 160 nm spacing between the DNWs. Figure 4.2b) is a Scanning Electron Micrograph (SEM) of the upper left corner of the top repeating pattern found on the piece of growth substrate. In the top of the image a rough line is visible. Along this line the growth substrate broke late into the project, why one can only find the substrate without the top arch if needed again. In the figure, the different areas of the repeating pattern, including the areas used for orientation, and the 1 dot 130-160 nm spacing areas are found.

In Fig. 4.3a) the shape of the half-shell Qdev 939, with Al on three facets, growth substrate piece are illustrated containing the pattern repeated multiple places around the original growth substrate. Figure 4.3b) is a graphic representation of the repeating pattern with different sections of different growth. The wide NW placed in front of all the other NWs are used to shadow the smaller NWs when Al is epitaxially grown onto the surface. Since the wider NWs access the same amount of In and As in the growth chamber, they will not grow as tall as the smaller ones, which results in the small ones getting covered with Al in the top of the wires, but not in the bottom. Furthermore, the shadowing NWs can be grown in other structures making them shadow different sections of the other NWs. Thus, this shadowing technique can be used to selectively deposit Al, or other materials, onto different areas up the NWs. While this technique is interesting, for different NW-Superconductor junctions, we have not pursued it in this thesis.

The right column of the repeating pattern is facet to facet and the left column is corner to corner. Each of the different spatial growth setup sections are distributed into subsections of different dot count and NW spacing. Figure 4.3c) displays a SEM image of the area around the uneven parallel DNW facet to facet 20 dot middle and right columns. The white ellipse fully incloses the 300 nm and 150 nm spacing sections. The inset shows a zoom-in SEM image of standing DNWs. In Fig. 4.3d) the subsections of the uneven parallel DNWs facet to facet section is shown. Here the corresponding area to Fig. 4.3c) can be found in the upper right corner.

Another detail about the growth geometry, is that, as described by Kanne et al.,<sup>44</sup> some DNWs grow in what they call "Eiffel tower" configuration, where the van der Waals forces makes the top of the wires clamp together, while others grow in "train track" geometry, keeping the NWs separated. More information about DNW growth is described by Kanne et al.,<sup>44</sup> and additional studies on such DNWs are reported by Vekris et al.<sup>84,85</sup> and Kürtösy et al.,<sup>50</sup> and briefly described in Chapter 3.

### 4.3 Nanowire deposition

After the inspection of the DNWs, they are picked up individually and deposited onto a blank 5x5 mm<sup>2</sup> substrate of highly doped Si with 200 nm thick SiO<sub>2</sub> surface. This is conducted, using an *Eppendorf TransferMan 4r* micromanipulator, which basically is a movable needle capable of picking up micrometer-sized items and wiping them off again. The needle, controlled in x-, y- and z-direction, by a joystick, utilizes Van der Waals forces to

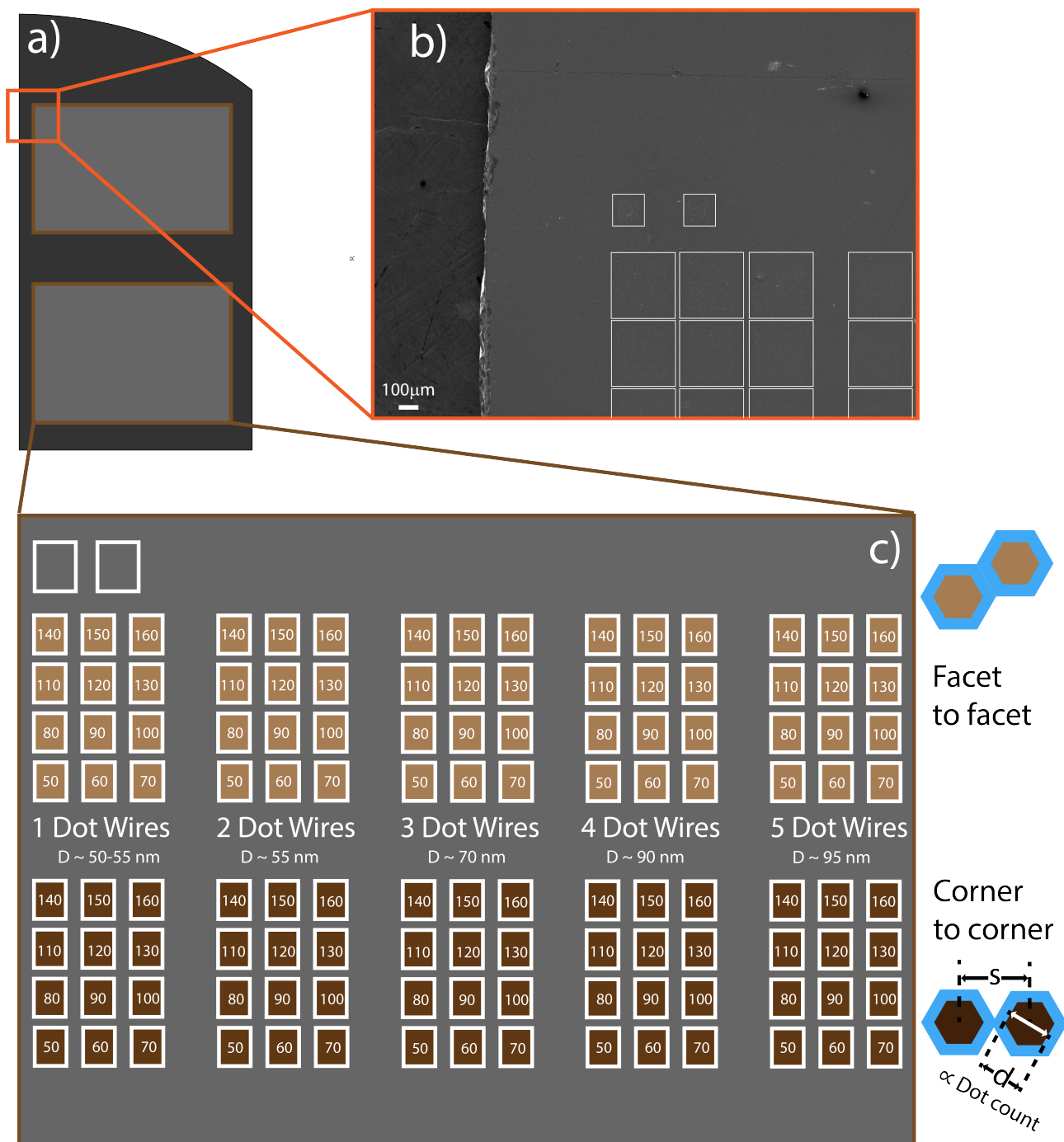


**Figure 4.2: Qdev 898 Map.** a) Is an illustration of the piece of the sample, Qdev 898, used for fabricating the full-shell devices in this projects. b) is a zoom-in on the top 1 dot facet to facet area. The white squares outlines where the DNW growth areas are. The SEM image is taken at  $V_{Acc} = 5\text{kV}$ . c) is a graphical representation of the standard design that are copied onto multiple areas of the original substrate, two of which are placed on the piece accessible to us. Dot count is the amount of holes that are made with EBL for later Au deposition. The more dots, the shorter and broader the wires. The top row is facet to facet DNWs, and the bottom row corner to corner as illustrated to the right. The two empty areas in the top right corner, were used to navigate.

make the DNWs stick, as it picks them up. Thus, to make the deposition as easy as possible, a specific method to pick up the DNWs is favourable. First, one pushes the needle into the side of the DNW to make it bent. Second,

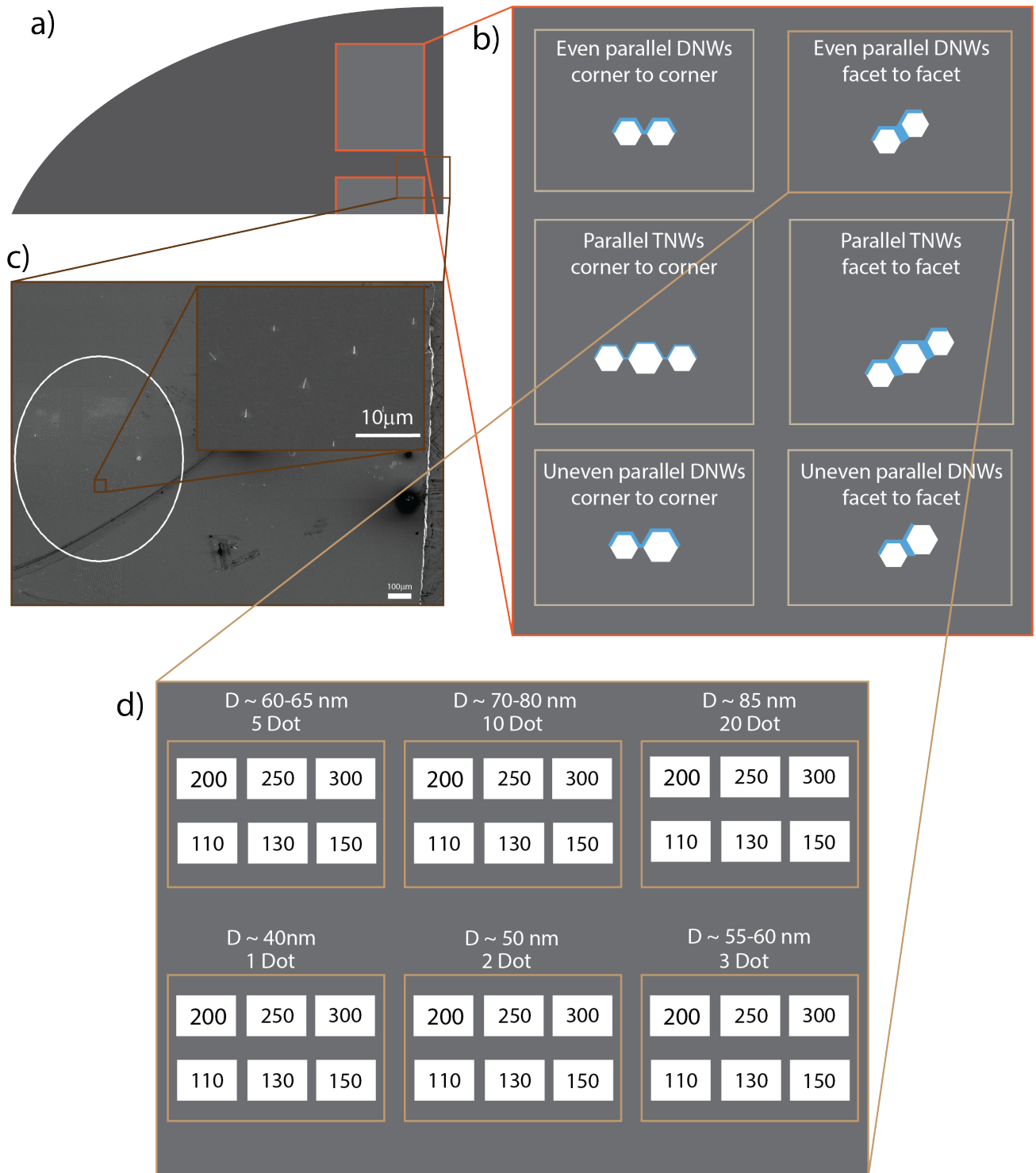


**Figure 4.3: Qdev 939 Map.** a) Is an illustration of the piece of the sample, Qdev 939, used for fabricating the half-shell devices in this projects. b) is a graphical representation of the standard design that are copied onto multiple areas of the original substrate. TNW means triple nanowire. c) is a zoom-in on the even parallel DNW facet to facet 20 dot 300 nm and 150 nm spacing sections. Image taken by A Vekris. The inset is a zoom-in on one of the growth regions, showing DNWs in a standing position. d) is a graphically illustrated zoom-in on the uneven parallel DNW facet to facet area. Dot count is the amount of holes that are made with EBL for later Au deposition. The more dots, the shorter and broader the wires. The numbers in the white boxes in each specific dot area, determines the center to center distance between the NWs. Both SEM images are taken at  $V_{Acc} = 5kV$ .

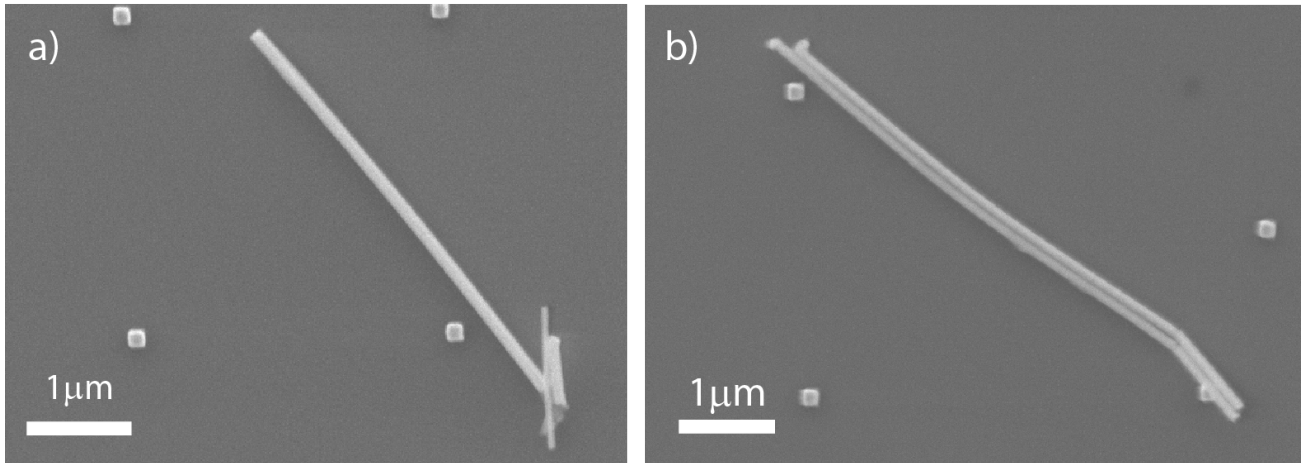


**Figure 4.4: DNW vs. SNW yield.** a) is a electron micrograph of a SNW deposited on Sample 3. b) is a electron micrograph of a DNW deposited on Sample 4. Both NW structures are grown on Qdev898 as displayed in Table 4.1. The SEM images are taken at  $V_{Acc} = 5\text{kV}$ .

the needle is lowered down into the DNW, increasing the strain on the connection to the growth substrate until it breaks apart and the DNW falls to the surface. Third, the needle is lowered down onto one of the DNW ends to pick it up, with as little interaction area between needle and DNW as possible, making it easier to wipe off later in the process.

Next the needle is moved to the blank substrate. Here it is gently transferred moving the needle in a straight in-plane motion, while lowering it down. Thus, the tip of the DNW, hanging from the tip of the needle, reaches the surface first and the rest of the DNW is then wiped of the needle, maximizing the DNW-surface interaction. In this step, one realizes how crucial the DNW structure is. As a matter of fact, having DNWs with too high spacing/dot count ratio, causes the NWs to split up into SNWs, when moved around by the micromanipulator, decreasing the DNW yield substantially. This was what happened under the fabrication of Sample 3, in Table 4.1, as  $\sim 20$  SNWs, one of which are displayed in Fig. 4.4a), were deposited onto the blank substrate resulting in a sample that would be better suited for other projects. This was solved by an inspection of the growth substrate, using SEM as described in Sec. 4.7, followed by the deposition of actual DNWs on, what became, sample 4, one of which are displayed in Fig. 4.4b). One may think that the easiest solution however, would just be to find at small spacing to make sure the NWs stick together. Unfortunately, this was not a proper solution in this thesis, since we also needed to minimize the interwire coupling for the transport measurements later on, in order to describe the system as a DNW structure instead of a large SNW system.

#### 4.4 Electron Lithography

When the DNWs are deposited, they need to be manipulated, either by etching something away from, or by depositing something onto the DNWs. The method used throughout this thesis to control the geometrical areas of such manipulations is Electron Beam Lithography (EBL). Figure 4.5 illustrates how the method works.



First, in fig. 4.5a) the blank Si/SiO<sub>2</sub> substrate is shown. Using spin-coating, a resist is evenly deposited onto the substrate as illustrated in fig. 4.5b), using a low acceleration program to avoid the DNWs being tossed around or even completely off the substrate. The typical resist used here is Poly(methyl methacrylate) (PMMA) in solution with Ethyl lactate for etching or Anisole for metal deposition. The reason to use this as a resist is that electron exposure weakens the polymer chain, and thus, one can focus a beam of electrons onto the areas where patterning is desired. Figure 4.5c) displays a quadratic pattern exposed by an electron beam. The patterns applied in this thesis is drawn in the *KLayout* software and translated to the language of the *Elionix EBL system* using *Beamer - GenISys-GmbH* software (Beamer). Now, when the resist is locally weakened, one can remove the weakened regions, using a developer solution. In this case, the typical developer solution used is 4-Methyl-2-pentanone (MIBK):IPA 1:3. This removal is illustrated in fig. 4.5d), where a cast can be seen. This cast can, as mentioned before,

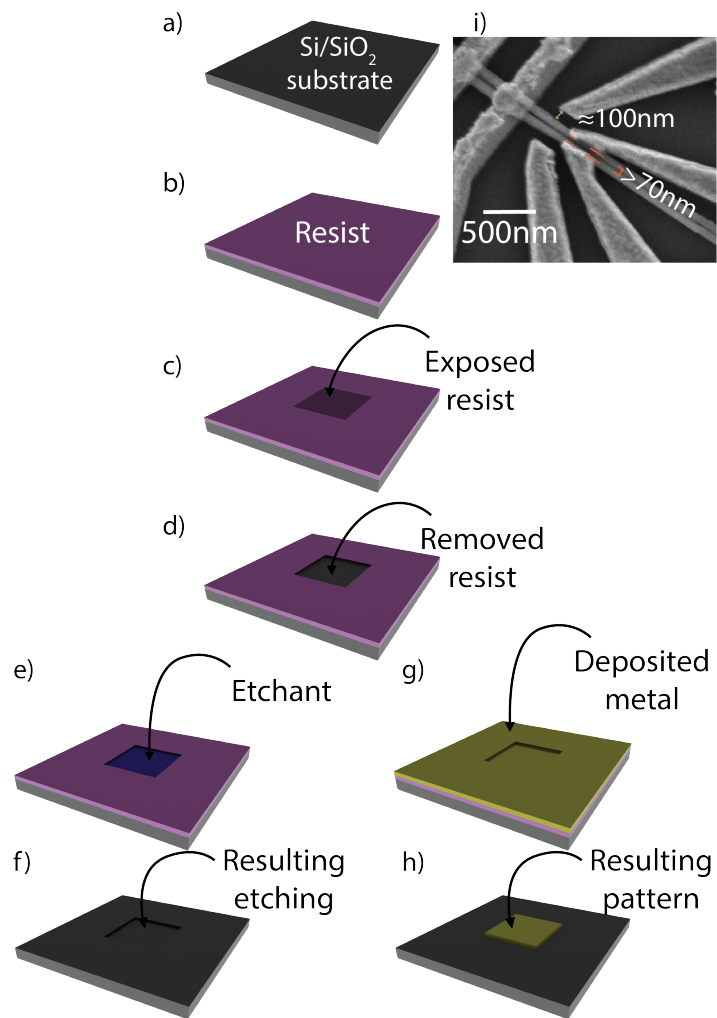


**Figure 4.5: Mechanism of EBL.** In a) the blank substrate is shown, then the resist is spin-coated onto the substrate resulting in b). Using a focused electron beam one can weaken the resist specific geometrical areas, yielding c), and by the use of a suitable developer the weakened resist is removed in d). From here, one can either etch in the area that are not protected by the resist as shown in e), leaving a pattern as in f) after resist removal. The other opportunity from d) is to deposit another material, typically a metal as in g). The metal deposition leaves a pattern as in h) after lift-off. i) is a SEM image, taken at  $V_{Acc} = 5kV$ , showing some of the important distances in the design. The image is of a device on sample 4 in Table 4.1

either be used for selective etching, as further described in Sec. 4.5 or for metal deposition as further described in Sec. 4.6.

The use of EBL instead of photon-based lithography, as UV lithography, allowed us to create considerably finer patterning, due to the diffraction limit of light being substantially larger than that of electrons. However, there is limits to this resolution of patterning. Thus, we have some guidelines regarding the patterning in specific situations. This includes, that the distance between the edges of contacts on each NW in a DNW device, must be at least 70 nm, distances between electrostatic gates and the item they are gating should be around 100 nm, as

---

illustrated in Fig. 4.5i), and distances between all metallic parts should generally be maximized. Furthermore, corners should be designed rounded rather than sharp, since that is expected to increase the liquid flow under lift-off, as further described in Sec. 4.6. In addition, the width of the patterns for metal deposition should be maximized as well up until a width of  $2\ \mu\text{m}$ , which in relation to the maximization of distance between the metallic parts can be quite difficult to optimize for advanced structures, where one often does not have space enough close to the DNWs to allocate the width on  $2\ \mu\text{m}$  to each metallic part. For patterns that are meant for etching, the etching can exceed the pattern by up to almost 300 nm, and even further if the sample are left in the etchant for too long. This happens as the etchant moves under the resist, why the patterns generally should cover a smaller area than what is actually intended to etch. Changing the field size and the pixel number in the Elionix System, called write field and dots respectively in Beamer, allows us to tune the resolution between 30 nm and 0.3125 nm. This should be tuned such that we at least have 10 pixels in the smallest feature we would like to pattern. When exposing, Elionix splits the whole area of exposure up into small squares with side length = field size, during its process it moves from field to field. Within each field, the pixel number is the amount of pixels that the Elionix deflects its beam to, without moving. Thus the increase in pixel number equals an increase of pixels each field is separated into, and the decreasing field size increase the amount of fields, and thus pixels, that the whole exposed area is separated into.

Working with these tiny structures demands a very high precision. This is usually achieved by aligning the SEM images to the design, that are drawn in Klayout. To do so, alignment marks are deposited on the wafers that are later cleaved into smaller pieces, denoted in this thesis as a "blank substrate" or "blanks". To sustain the alignment pattern, leads and contact pads on the wafer while cleaving, a layer of AZ1505 resist are spinned onto the wafer before cleaving. This resist are removed from the individual blank, before NW deposition. From there, to have the correct design-file for the blank substrate is crucial for the ability to align the following patterns correctly. Sample 5, as described in Table 4.1, were discarded as a result of lack of access to the correct design-file. However, having the right design-file is not necessarily a promise of correct alignment. Indeed Device 2 were discarded due to an alignment problem, causing an offset on 50 nm, when depositing metal contacts. During the fabrication of Device 4, the alignment became harder by each fabrication step, as the alignment marks used in the ELB system, started to become covered by metal. This was caused by the scanning of the alignment marks breaking down the resist, such that the following metal deposition covered the segment of the alignment mark that had been scanned.

## 4.5 Aluminum etching

In this project, selective etching of aluminum were applied in the fabrication of sample 1, 2, 8, 9 and 10. An Island Device from sample 1 is shown in Fig. 4.6. In this device all the Al, but that in the false-colored blue

area is removed. The principle of the selective etching mechanism is shown in Fig. 4.5e-f). Here the resist is protecting the area that are covered, but the developed areas is exposed the the etchant. After removal of the resist, one can see a hole in the substrate, where the resist was not covering. Similarly, in these studies, wells for the aluminum etchant, typically acid Transene - D at 50°C, were produced by EBL. This was the most difficult step of the fabrication process due to the etching speed. The etching were done throughout 8.5 seconds, to neither under- or over-etch. Over-etching happens, as the etchant is not optimally confined, in the PMMA wells, but tend to slide under the resist etching a larger area than intended. This can, however, be minimized by using a resist solution with a greater adhesion, in our case PMMA in solution with Ethyl-Lactate instead of Anisole.

Figure 4.6 is over etched by  $\sim 40$  nm, while usual values in this thesis extend up to 270 nm for Device 4 with a normal value at  $\sim 180$  nm. In the case of device 4 however, we did plan for over etching and designed the following parts based on the extend of this.

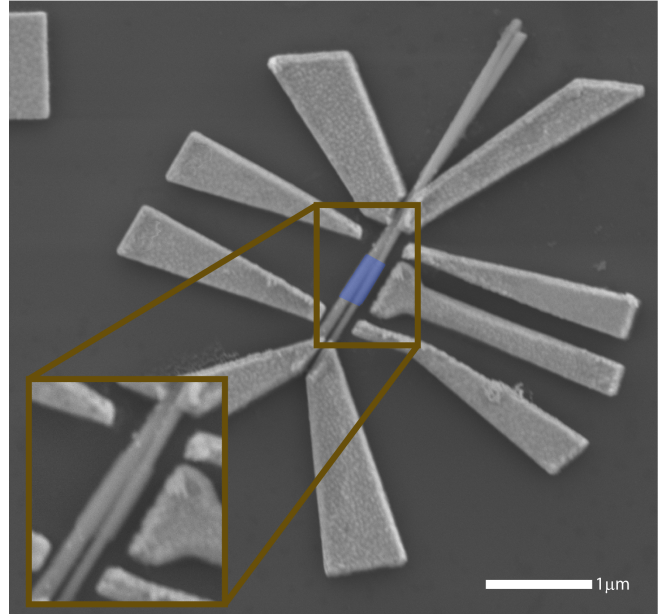


**Figure 4.6: Island device.** SEM image of and Island device fabricated by selective etching of all aluminum on the DNWs but that in the false-colored blue region. This image furthermore provide an understanding of the distances in between the contact. The device is from sample 1 on Table 4.1. The inset is a zoom-in showing the region covered with Al, without coloring. The SEM image is taken at  $V_{Acc} = 5kV$ .

## 4.6 Metal deposition

After the aluminum etching, contacts and gates needs to be deposited, as illustrated in Fig. 4.6. This demands another EBL circle. In this case however, the mechanism is shown in Fig. 4.5g-h). Here a layer of metal is deposited onto the substrate and cast, followed by resist removal, here called lift-off. The metal deposition process can be quite challenging, as the removal of excess metal is a vital step in the fabrication to avoid shorts, while not being too invasive towards the devices. The challenge of this is mainly due to the very close distances between the contacts on the individual NWs, but also due to the rather specific distances of the gates to the DNWs and at the same time, the maximization of the distance in-between the metallic parts.

When the cast is finished the sample is loaded into a vacuum chamber of an apparatus named *AJA Orion*. Here, argon milling is first used to remove the oxide layer that has formed on the NW in the contact with the air. Following the milling process 5 nm titanium and usually  $\sim 200$  nm gold is deposited onto the substrate, to firmly connect to the NWs at least 185 nm of metal should be deposited.<sup>83</sup> Furthermore, to increase the chances for a

functional connection one can deposit with an angle of  $3^\circ$  for the first half of the Au deposition and  $-3^\circ$  for the second half. The angle makes it more likely for the Au to climb up onto the NWs. The reason for the Ti to be deposited first is to serve as a sticking layer between the substrate and Au, creating a stable metallic piece.

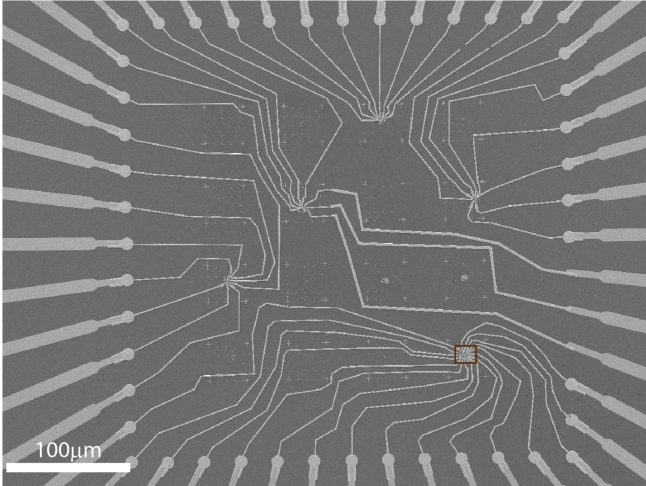


**Figure 4.7: Connections between the devices to the outer leads.** SEM image of the sample area on a substrate. Here five areas with devices has been connected to the outer leads using electron lithography in combination with metal deposition. This is Sample 4 in Table. 4.1. A zoom-in of the brown square is displayed in Fig. 4.8. The SEM image is taken at  $V_{Acc} = 5kV$ .

wards towards the NMP surface. Furthermore, flushing the samples with acetone and isopropanol after blowing all the visible metal away in the NMP, adds to the chance of removing all excess resist and metal. This whole process is usually repeated, in multiple steps ending with depositing metal that connects the device gates and contacts to the outer large leads on the substrate as shown in Fig. 4.7. The leads connects the six DNW Little-Parks full-shell devices to the outer leads.

## 4.7 Imaging

Throughout the fabrication process the samples were imaged, using both optical microscopy and SEM. The SEM, which utilizes the smaller wavelength of electrons compared to visible light to create very high resolution images, used in this project is a *JEOL JSM-6320F*. To avoid too much charge building up in the NWs, we try to limit the imaging times. Furthermore, the acceleration voltage,  $V_{Acc}$ , should be minimized, as we expect this to be less invasive. Figure 4.8 is a SEM images of the fabrication of two of six tunnel probe devices, that are ready for measurements. The rest of the devices, ready for measurement on Sample 4, can be seen in Appendix Fig. A.3.

## 4.8 Sample loading

From this step and onward I have not taken any part in the practical work in person, due to Covid-19 access restrictions. I did however, follow the measurements of Josephson Junctions Devices (see Chapter 5) and Island Devided (see Chapter 6), while doing some data analysis on both, which I extended later. Nonetheless, it is still relevant to describe the sample loading and measurement setups.

When the fabrication of the device is finished, the sample is glued onto a "daughterboard", a standardized sample holder for low-temperature measurements. This is the first step of adapting the device inputs and outputs to the measurement setup. Next, the sample needs to be electrically connected to the daughterboard. This is done using a wire-bonder. A wire-bonder is essentially a sewing machine, capable of sewing with metallic wires such as Al

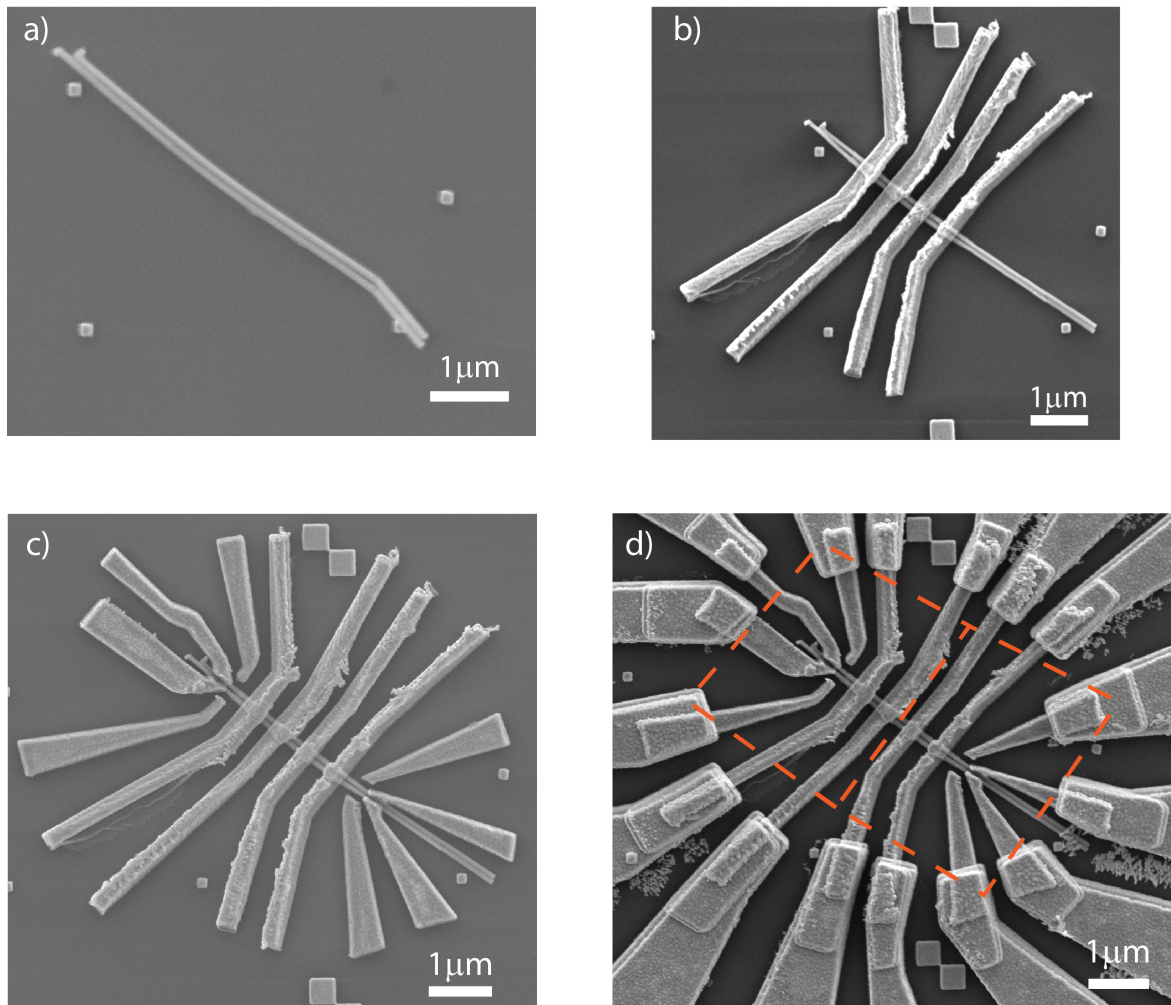


**Figure 4.8: Little-Parks tunnel probe device fabrication.** SEM images, taken at  $V_{Acc} = 5kV$ , of two devices being fabricated on one DNW. First the DNWs are deposited on the sample, Sample 4 in Table. 4.1, as shown in a), then aluminum is etched away from the ends and Ti/Au contacts are deposited on the Al left in the middle b). Following this, gates and contacts on the NWs are deposited c). And finally, the device is connected to the outer leads d). Each device based on the DNW is outlined by the dashed box. The devices are ready for measurement. The images is zoom-in of the brown square is displayed in Fig. 4.7

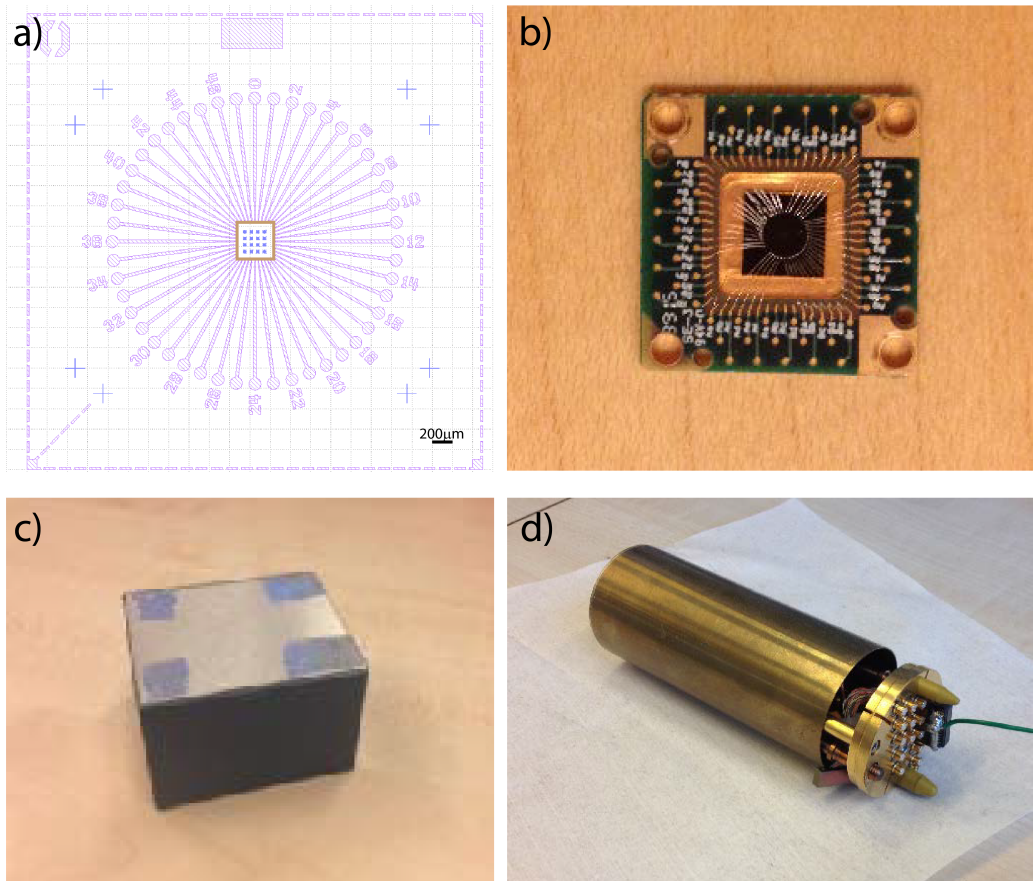


**Figure 4.9: Equipment for the sample preparation.** a) Is the design that are printed onto the blank substrates. In the middle, marked with a light brown square, is the sample area. Surrounding the sample area is the outer leads that merge out into the circular bonding pads. The crosses in each corner are alignment marks. The square in the top is used to rotate the substrate correctly when loading it into the different apparatus. b) is a photograph of a bonded sample on a daughterboard, the wires are Al. c) is a photograph of a box, used as a Faraday cage to transport the bonded substrate safely from the wire-bonder to the loading puck that are shown in d). b,c & d are adapted from Vekris<sup>83</sup>

wire that are used in this project. The wire-bonder connects the bonding pads of the outer leads in the sample, as seen on Fig. 4.9a) to the pins of the daughterboard using the gold pads that is shown, placed in a square, around the sample on Fig. 4.9b). Throughout the bonding, grounding of the devices are important. This is an effect of using NWs as semiconducting channel, since they are fragile and delicate to abrupt changes in voltage. Thus, it is important to keep the instruments, that one uses to handle the devices, as well as oneself, grounded. If the device itself is floating, the opposite of grounded, it can accumulate charge from the surroundings. After such an accumulations, the mounting of the device into the measurement apparatus will place it close to another potential, which can cause a sudden current to run through the NWs and damage or destroy the device by joule heating.

After bonding, the sample needs to be transported to the loading puck that holds the sample in the dilution refrigerator. Figure 4.9d) is a photograph of such a loading puck. This transport process however, is another risk of damaging the device. Thus, to increase the yield, the sample are placed in a Faraday cage that protects

---

it against external electromagnetic fields, when transported from the wire-bonder to the loading puck. This Faraday cage, essentially a box made of metal, is shown in Fig. 4.9c). The last precautionary step to savour the most devices, happens during the loading process where the same grounding is used for both sample mounted on the loading puck and load lock. This further minimize the risk of abrupt voltage changes. All these steps, striving towards keeping the potential as low as possible, increases the yield.

## 4.9 Dilution refrigerator

For many quantum effects to be measurable, one needs to work at a low temperature. The explanation for this is the different energies that affects a system. In condensed matter physics and in this work in particular, a lot of the interesting energies are of the order of a few meV. This could, for instance be the superconducting gap of a superconductor that usually is below 1meV. If the thermal energy,  $k_B T$ , exceeds the energy of the superconducting gap, the individual electrons starts getting excited by the thermal energy and breaks down the superconducting Cooper pairing. For reference the thermal energy at  $22.0\text{ }^\circ\text{C} \sim 25.5\text{ meV}$ . Thus, to even study known quantum effects such as superconductivity one needs the possibility to cool down a sample to at least a few K.

Luckily, we had the possibility of using an Oxford Triton  $^3\text{He}/^4\text{He}$  dilution refrigerator allowing us to do all the experiments, presented in this thesis, at 30mK. The whole instrument are based on the principle, that  $^3\text{He}$  dilutes in  $^4\text{He}$ , draining heat and thus supplying cooling power. This process happens since it facilitates an increase in entropy. This process has an equilibrium at 6.6 volume-% diluted  $^3\text{He}$ . However, to push this equilibrium into a continuous cooling Fig. 4.10a) displays a schematic of what happens in such a dilution refrigerator. Starting up in the right corner,  $^3\text{He}$  is pumped into the system, where it first meet a heat exchanger. The heat exchanger precool the  $^3\text{He}$  before it continues to the impedance that cinches the condensing pressure is high enough to liquefy the  $^3\text{He}$ . The pressure should be  $\sim 2.5\text{ bar}$ . Furthermore the impedance cools the  $^3\text{He}$  even further, due to the Joule Thomson effect, as the  $^3\text{He}$  is compressed. This adds even further to the condensation. Then the  $^3\text{He}$  passes past a couple more heat exchangers were after it reaches the mixing chamber, where it cools down through the dilution process. Here the the pressure is  $\sim 0.5\text{ bar}$ , due to lower circulation rate. In the mixing chamber, the  $^3\text{He}$  is driven upward, by osmotic pressure, past some heat exchangers that heats it up and into the still where it is heated and thus separated from the  $^4\text{He}$ . On the way up into room temperature the  $^3\text{He}$  flow past a heat exchanger that heats it further up before reaching the room temperature gas handling system, that are used to recycle the  $^3\text{He}$  back into the system.

In Fig. 4.10b), a dilution refrigerator without its radiation shield is shown. The approximate temperatures at the different plates are marked as well as the location of the still, heat exchangers and mixing chamber. The actual base temperature is 25 mK, even though the theoretical one in Fig. 4.10b) says  $\sim 10\text{ mK}$ . Lower values than

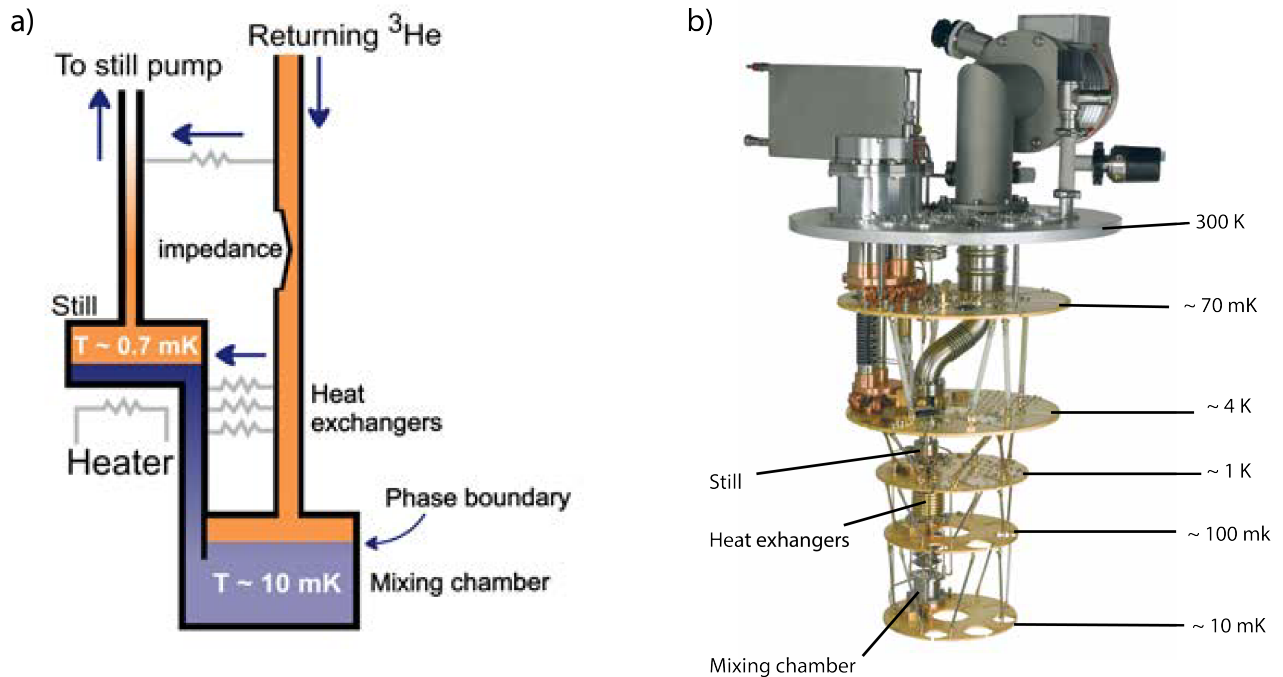


**Figure 4.10: Dilution refrigerator.** a) Is a schematic of the dry type of dilution refrigerators used in this project. The  $^3\text{He}$  travels from the top right down into the mixing chamber, dilute in  $^4\text{He}$  dissipating cooling power, and runs up through the left part of the system. Back at room temperature it is pumped to around and prepared to be recycled into the top right part again. b) Is an image of a dilution refrigerator without its radiation shield. The different plates are marked with their approximate temperatures as well as the locations of the Still, Heat exchangers and Mixing chamber are. Adapted from Oxford Instruments.<sup>8</sup>

25mK are virtually unattainable to access, since the Kapitza resistance, between the helium and metals, increase with a cubic dependence with temperature, preventing heat transfer withing the refrigerator.<sup>8</sup>

## 4.10 Measurements

The typical experiments that were conducted during this project were current and differential conductance measurements at low temperature,  $T = 30\text{mK}$ . To run these experiments a combination of instruments were applied to send current through the DNW devices and measure the following outputs as well as control the gates. Figure 4.11 display a complete instrument setup. Starting from the Source unit, there is a lock-in amplifier and a digital to analog converter (DAC). The first-mentioned produce an AC signal, that are divided by  $10^4$  by a voltage divider before being passed on, while the second-mentioned produce a DC signal, that are divided by  $10^3$ . This division of the voltage, is executed in order to create an excitation that exceeds the thermal noise  $k_B T$ , while increasing the resolution of the DC signal. In this way, the source unit allows us to study the devices with voltages up to 10meV. The AC and DC signals are combined in the voltage divider as displayed in Fig. 4.11. For the 4-terminal measurements on the DMW Josephson Junctions, described in Chapter 5, a 100 k $\Omega$  resistor were then applied to change the input from voltage bias to current bias. Then when the signal reach the breakout box, it is send out into one of the gold contacts on the DNW device. Before reaching the device however, the



---

signal is passed through an RC filter, a component that provides an upper bound for the frequency of the AC signal that arrive to the device. The RC filters are situated in the cryostat. After passing through the device, the signal enters another RC filter, whereafter it continues into the breakout box.

From the breakout box, the signal runs to the current amplifier, shown in the red measurement unit in Fig. 4.11, that amplifies the voltage by  $10^8$  and converts current to voltage. It is a substantial advantage to apply this amplification, as the signal before this is very indistinct and quite challenging to differentiate from noise. From there the signal is distributed to another Lock-in amplifier, capable of measuring the AC component and a digital multimeter (DMM) capable of measuring the DC component. The first of which is used to extract the differential conductance.

To control the gates a DAC is connected, one connection for each gate which is six for the island device and three for the Josephson Junctions in Fig. 4.11, to the breakout box, which is further connected to the individual gates. Thus the DAC controls the gating. The resolution of the DAC used in this project were  $300 \mu\text{V}$ , due to it being a 16 bit DAC. One would oftentimes want the highest possible resolution as it allows the tuning of very sensitive devices.

For the 4-terminal Josephson Junction measurements, the experiment were changed to current bias, by applying a  $100\text{k}\Omega$  resistor between the voltage divider and breakout box, as displayed in the bottom of the source unit (blue tint) in Fig. 4.11. The voltage difference between the two superconducting segments is measured. This is done by the brown measurement unit in Fig. 4.11, that records the difference between the two dark brown contacts and amplifies this with 100. Then this difference is measured in a lock-in, for the AC component, and a DMM, for the DC component.

The lock-in amplifier is one of the most key parts of this setup. The lock-in amplifier of the source units sends out a signal with frequency  $f_{\text{init}}$ . However, during the measurement, a multifold of waves, originating from noise, with different frequencies can interfere. When the waves arrive to the lock-in of the measurement unit only a specific frequency is detected. This is caused by the utilization of orthogonality of sinus functions as the lock-in has a set frequency,  $f_{\text{set}}$ , that is multiplied with the received frequency,  $f_{\text{rec}}$ , and integrated over a certain time. From that, only the product when  $f_{\text{set}} = f_{\text{rec}}$  will be finite, the rest will be zero and effectively discarded.

Matlab-qd, the software running the instrumental setup is capable of controlling the most of the equipment including the dilution unit, DACs and the superconducting magnet that are places around the cryostat. It is designed at University of Copenhagen, and were used in this project to run the experiments as well as extract data from the instruments.

To facilitate the communication between the computer and the instruments, General Purpose Interface Bus (GPIB) were applied. GPIB is a protocol that provides the communication between two or more devices.<sup>27</sup> To quickly and easily plot data along the acquisition, the programmes "Folderbrowser" and "InSpectra Gadget" were applied. Thess makes it easier to navigate in what data showed relevant features for the experiment and

---

what did not.

Information about the quality of the gates is usually accessed in the beginning of the measurement of a new device. Serving this purpose gate sweeps is usually the first thing measured. These reveals information such as gate leakages or other effects on the conductivity of the device as well as a map over potentially interesting features.

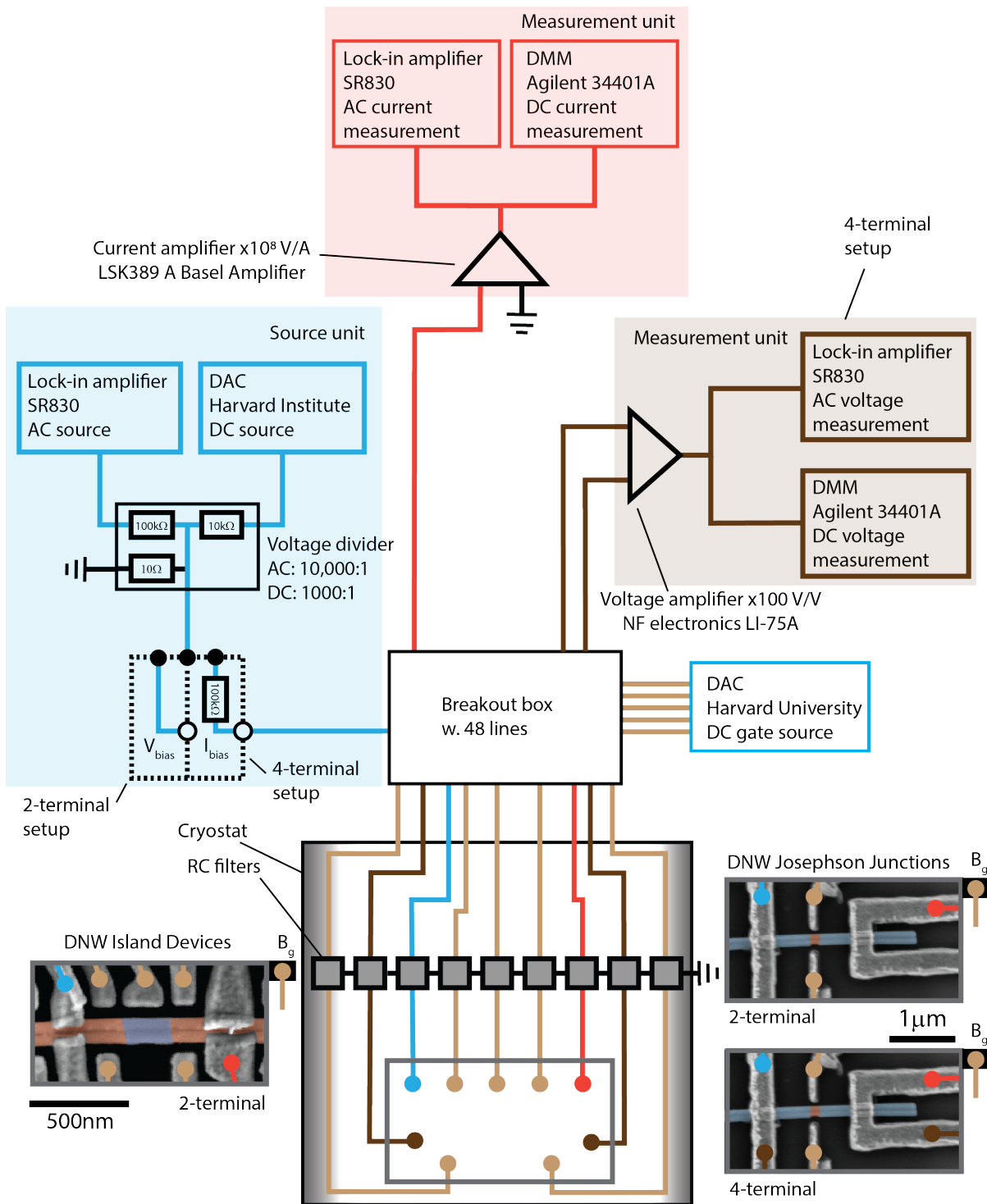


**Figure 4.11: Measurement setup.** In the bottom of the figure, Island devices or Josephson junction were situated in 2-terminal  $V_{\text{bias}}$  setups or, only for the Josephson junctions, the 4-terminal I-bias setup, in the dilution refrigerator. Above the device location, RC filters are situated. Over the cryostat a breakout box is located, this is connected to all the leads from the devices and distribute the signals to the measurement units (red and brown tint). The source unit (blue tint) sends out the signals to the breakout box that passes them on in through the sample. The DC gate source provides the potential applied on the gates in the device. The red tinted measurement unit measures current and the brown one voltage difference, the last of which is only applied in the 4-terminal setup. The SEM image of the devices is taken at  $V_{\text{Acc}} = 5\text{kV}$ .

## 5 Double-Nanowire Josephson Junctions

In this chapter I will first describe the motivational perspectives of studying DNW Josephson Junctions, including a description of Cooper Pair splitting conducted by Deacon et al.<sup>20</sup> Then I will introduce some important aspects in SNS-junctions, including mixed Andreev reflection (MAR) and supercurrent as well as the different accessible regimes. Following this, I will present an article by Heedt et al.<sup>38</sup> representing a modern characterization of an SNS junction. Afterwards, a description of the fabrication and an analysis of the measurements of a DNW Josephson Junction are presented. At last it is concluded that MAR and supercurrent are detected, as well as both NWs being transmitting individually. During the investigation presented in this chapter I followed the measurements of the devices fabricated by Alexandros Vekris, without taking actual part in doing the measurements due to access restrictions associated with the Covid-19 pandemic. Furthermore I have done the theoretical descriptions and data analysis described in the chapter.

### 5.1 Motivational perspectives in Double-Nanowire Josephson Junctions

Quantum entanglement is one of the most counter-intuitive phenomena in quantum mechanics, as it allows the information about two entities as a whole to be less uncertain than the information of the individual entity. As a matter of fact, entanglement allows two completely unknown states to have a completely known shared state. This enables negative entropy in quantum information theory,<sup>82</sup> since a measurement of the first individual state, being uncertain, will result in entropy, while the following measurement of the second state, yielding the certain shared state will result in the withdrawal of the entropy

Entanglement has additionally been found to serve as an order parameter in quantum phase transition characterization,<sup>64</sup> and topological quantum phase transitions as a rearrangement of the constellation of entanglement.<sup>13,46</sup> Furthermore, the global entanglement of the whole state in a topological phase constitutes a promising rigidity for encoding of quantum information, since it makes it stable against local parameters. This means that no local noise is capable of removing the topological state from its subspace, since there is a finite gap between the ground state and the excited state.<sup>82</sup>

In 2015, Deacon et al.<sup>20</sup> managed to confirm the spatial separation of two spin-entangled electrons, a Cooper pair, followed by their recombination. This was an exciting finding, as Cooper pairs in the BCS superconductor can be seen as maximally entangled Einstein-Podolsky-Rosen (EPR) states. The preparation and isolation of

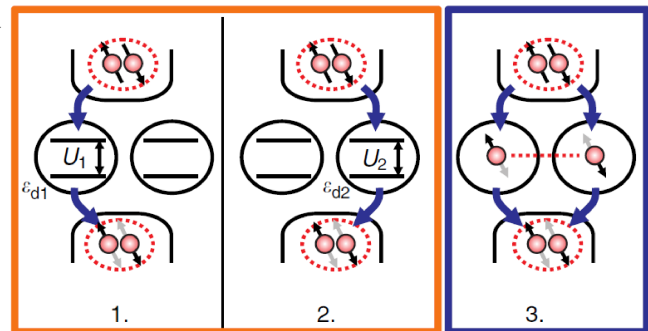


**Figure 5.1: Cooper pair tunnelling processes in a parallel double QD Josephson Junction.** Schematic of the three lowest order Cooper pair tunnelling processes through a parallel double QD Josephson Junction. 1 and 2 are through one of the QDs called local coupling and 3 are through both called non-local coupling. Process 3 utilizes EPR states. Adapted from Deacon et al.<sup>20</sup>

EPR-states is highly attractive in solid state physics, since EPR states can be used to teleport qubit states around a chip. To achieve this Deacon et al.<sup>20</sup> measured the supercurrent through a Josephson Junction (JJ) inhabiting two parallel self-assembled InAs quantum dots as illustrated in Fig. 5.1. From the setup they observed an enhancement of supercurrent when the Cooper pairs from the first lead are split between the QDs and recombined after traveling to the second lead.

The experimental setup introduced by Deacon et al.<sup>20</sup> should be applicable using DNWs as it is relatively easy to form QDs in semiconducting NW segments longer than 100 nm. Thus, this allows us to study the Cooper pair splitting phenomena in depth, using DNWs with epitaxially grown superconductor.

## 5.2 Introduction to DNW Josephson Junctions

JJs are typically created by placing a thin superconducting weak link in-between two superconductors. The weak link can be made from insulator (SIS) or normal metal (SNS). Depending on the coupling,  $\Gamma$ , of the JJ multiple regimes are achievable, amongst these are the open and the Coulomb blockaded (CB). In the open regime,  $\Gamma$  is large enough,  $> \Delta, U$ , to be better described as a transmission,  $t$ . In this regime the device operates like a gateable JJ. In a JJ supercurrent can run from one superconductor to the other through the weak link, this is an effect of the proximity effect. In contrast, the CB regime is described by  $\Gamma$  being weak,  $< \Delta, U$ , resulting in another range of smaller regimes (sub-regimes) depending on the parameters,  $\Gamma, \Delta, U$ , as well as the accessible QD states.<sup>34</sup>

The DNW JJs can be modelled as displayed on Fig. 5.2a) for the open regime and on Fig. 5.2c) for the CB regime. In the open regime the resonant transmissions,  $t_{1,2}$ , quantifies the amount of supercurrent running through the JJ in respectively the top and bottom wire. This is illustrated by the black barriers in Fig. 5.2a). The interwire coupling,  $\Gamma_{NW}$ , determines how much the charge carrier wave functions of the two NWs overlap. In contrast in the CB regime, there's two parallel QDs, one in each NW, coupled to the first lead with coupling  $\Gamma_1$  for the upper dot and  $\Gamma_3$  for

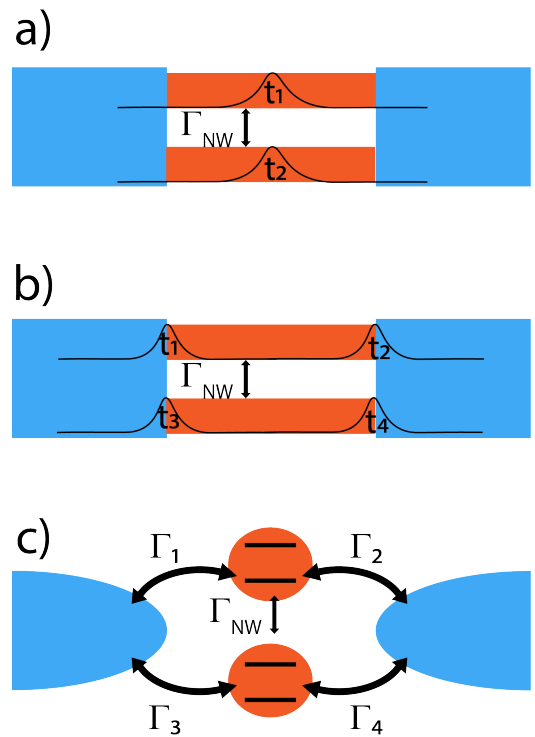


**Figure 5.2: DNW Josephson Junction devices.** a) Model of a DNW Josephson Junction device in open regime, with  $t$  being the resonance dependent transmission between the two superconducting leads. b) Model of a DNW Josephson Junction device in Fabry-Pérot regime, with  $t_{1,2,3,4}$  being the resonant tunneling between the each superconducting leads and NW. c) Model of a DNW Josephson Junction device, with  $\Gamma_{1,2,3,4}$  being the couplings between the superconducting leads and the two quantum dots that have arisen in the Coulomb blockaded regime. c) is a false-color SEM of the first device studies in this chapter, Device 3. Magnetic field direction,  $B$ , is indicated as well as gate potentials  $V_{g1,g2}$ . Image is taken by A Vekris.

the lower dot. From the QDs the couplings to the next lead is  $\Gamma_2$  for the upper dot and  $\Gamma_4$  for the lower. The couplings is here a measure of the extend of which the charge carrier wave functions in the respective lead and QD overlap.

Furthermore, in-between the open and the CB regime, another regime can be found. This is the Fabry-Pérot regime as illustrated in Fig. 5.2b). In this regime the NW-Superconductor interfaces creates barriers, illustrated by the black barriers in Fig. 5.2b), but too small to be in the CB regime, but too large to be in the open regime. Here Fabry-Pérot resonances can arise as the charge carriers can be reflected back and forth the barriers after tunneling through the first one. During these back and forth reflections they have a finite probability of tunneling through the second barrier and another probability to tunnel back through the one they came from. Thus, the total tunnelling through the top-wire,  $T_{up}$ , and the down-wire,  $T_{down}$ , is mediated by the barriers and the gates affecting the respective NW,  $V_{g1}$  and  $V_{g2}$ :  $T_{up}(t_1, t_2, V_{g1})$ , and  $T_{down}(t_3, t_4, V_{g2})$ .

This description is however, a very simplified model for our system, as the mean free path of the electrons are smaller than the length of the JJ.<sup>17</sup> Thus we have scattering events instead of a ballistic system, that is the more ideal description of the Fabry-Pérot regime.

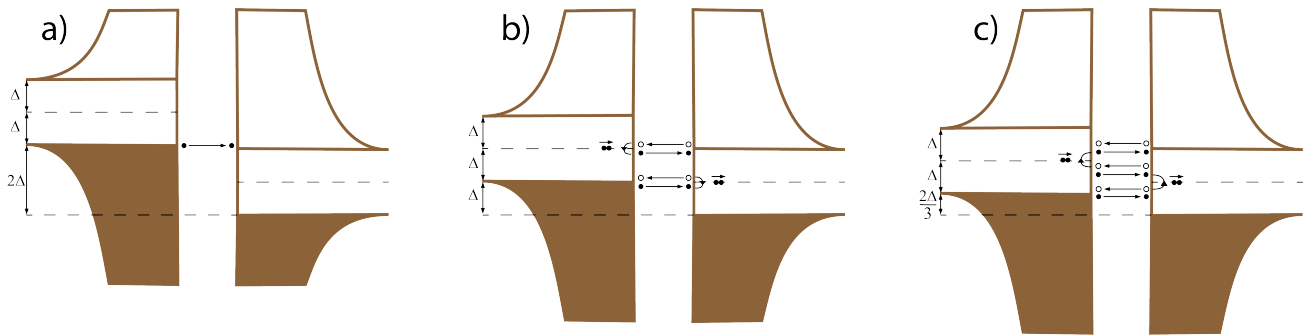


**Figure 5.3: Multiple Andreev reflections in a Josephson Junction.** Schematics of transport through a JJ with a) being direct quasiparticle tunnelling, and b-c) being multiple Andreev reflections with  $n = 2$  and  $3$  respectively. The open circles indicates quasi-holes and the solid quasiparticles. Created with inspiration from Sand-Jespersen<sup>69</sup> et al. and Buitelaar.<sup>10</sup>

The Fabry-Pérot resonances can modulate as multiple Andreev reflections (MAR) for  $|V_{SD}| < 2\Delta/e$ .<sup>29</sup> The allowed processes are only found bias potential,  $V_{SD} = 2\Delta/ne$ , with  $n = \pm 2, 3, 4, \dots$  where  $n$  is the amount of AR processes taking place in the transport through the junction<sup>69</sup> as illustrated in Fig. 5.3. Here a) is quasiparticle tunnelling at  $V_{SD} = 2\Delta/ne$ , b) is MAR with  $n = 2$  and c) is MAR with  $n = 3$ . The measurable effect of MAR is a structure of conductance peaks located at every point in  $V_{SD}$  defined by the formula above.

### 5.3 Status on the field of Josephson Junction Devices

In August 2021, Heedt et al. published a paper investigating the transport properties of a JJ based on a a new

fabrication technique called the Shadow-wall method. As illustrated in Fig. 5.4a), the InSb NW is selectively placed behind the pre-patterned shadow-walls and on top of bottom gates. Following the placement, Al is deposited, with an angle of  $30^\circ$ , onto the NW on the areas not screened by the shadow-walls creating an untouched JJ with regards to fabrication steps, such as lithography, metal deposition and etching that can harm the NW-interface. Applying this fabrication method Heedt et al.,<sup>38</sup> measured ranges of observable supercurrent considerably larger than for other reports on InSb JJs.<sup>52,61</sup>

Figure 5.4b) displays conductance as a function of bias potential,  $V_{SD}$ , for two of such shadow-wall JJ devices. They both show subharmonic conductance peaks as a result of MAR. The green traces are theoretical fits of the conductance peaks, yielding the induced superconducting gap-values on  $\Delta = 235 \mu\text{eV}$  for device 1 and  $\Delta = 229 \mu\text{eV}$  for device 2.

Device 2 is further investigated in Fig. 5.4c), where the parallel magnetic field dependence,  $B_{||}$ , of the conductance is plotted as a function of  $V_{SD}$ . This furthermore displays the MAR evolution as the magnetic field increases, until superconductivity is broken at critical field,  $B_C \sim 1.2\text{T}$ . Outside the gap, small conductance peaks is visible with an average spacing on  $\sim 30 \mu\text{V}$ . Due to their g-factor on  $\sim 20$ , being in-between that of Al,  $|g_{Al}| = 2$ , and that of InSb,  $|g_{InSb}| = 30\text{-}50$ , Heedt et al. expected the conductance peaks to arise from discrete states in the InSb hybridized with the ones of Al. The visibility of these structures, they anticipated, could be a result of their gentler atomic hydrogen surface treatment of the NW, compared to the more invasive chemical and physical etching methods often used in similar investigations, such as the argon milling applied in this project.

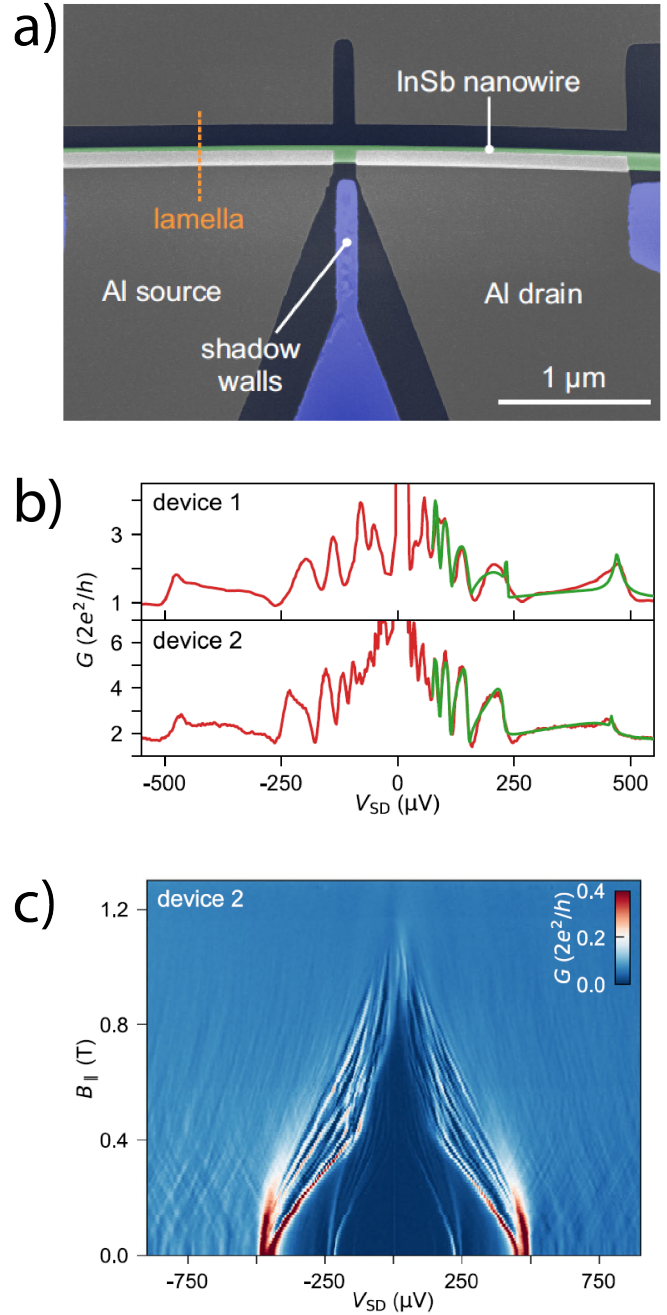


**Figure 5.4: Shadow-wall method based Josephson Junctions.** a) A false-color SEM of a shadow-wall JJ. The lamellar is a cross-section further investigated in the article<sup>38</sup> b) is the differential conductance as a function of bias potential,  $V_{SD}$  for two devices, device 1 in top panel and device 2 in bottom panel. Device 1 and 2 respectively is measured at backgate voltage,  $V_{BG}$  5.1 V and 3.0 V. The green traces are theoretical fits of the transmissions. c) is the conductance as a function of parallel magnetic field,  $B_{||}$  and bias potential,  $V_{SD}$ , for device 2. Adapted from Heedt et al.<sup>38</sup>

## 5.4 DNW Josephson Junction Devices

To achieve the long term goal to have a EPR reservoir in a DNW system, some conditions apply. First, the growth of hybrid DNWs must be achieved. This was done by Kanne et al.<sup>44</sup> before the onset of this thesis. Next step, and our short-term goal, is to confirm superconducting properties in the hybrid DNWs. The fabrication of a JJ is chosen for this short-term goal, as it is a well-known junction, with plenty of phenomena to observe depending on the regime.

### 5.4.1 Fabrication of DNW Josephson Junction Devices

Multiple devices as the one shown in Fig. 5.5 were fabricated. The devices were made from two parallel DNWs with Al epitaxially grown on three facets, taken from the uneven parallel corner to corner 10 dot (Diameter,  $D \sim 70-80$  nm) 250 nm spacing and facet to facet 20 dot ( $D \sim 85$  nm) 200-250 nm spacing areas as displayed in Fig. 4.3. First, the aluminum were selectively etched as described in Sec. 4.4-4.5, followed by deposition of the displayed gates and contacts using selective deposition as described in Sec. 4.4 and 4.6. The contacts covering each superconducting lead, diverge into two normal leads enabling a four-terminal measurement configuration.  $V_{g1,g2}$  allows the tuning of the weak links of each NW, while a backgate is applied to tune the coupling regime over the whole JJ, thus shifting between the Coulomb blockaded and open regime as well as the sub-regimes that can be found in the CB regime. The length of the JJ in Fig. 5.5,  $L \sim 140$  nm.

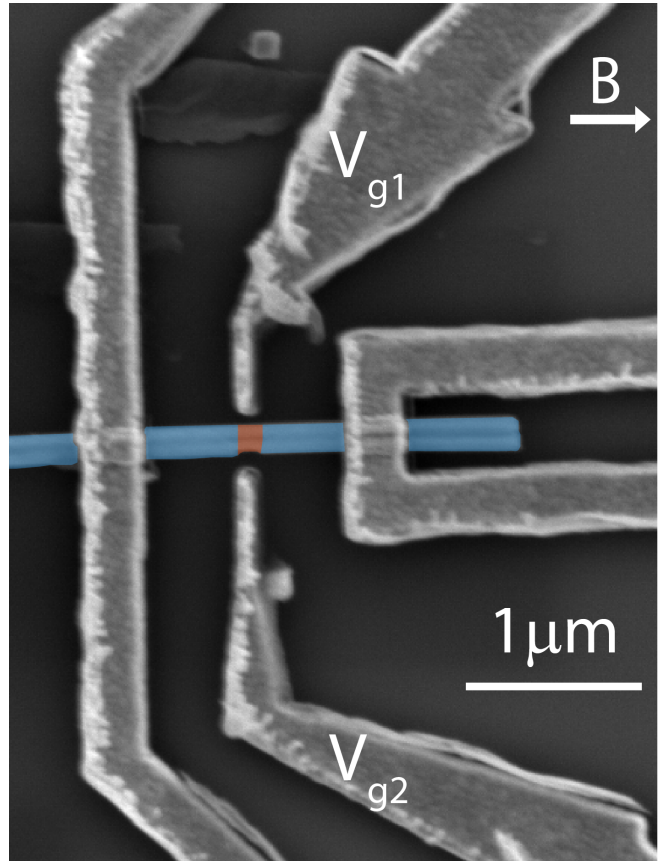


**Figure 5.5: DNW Josephson Junction device.** False-color SEM of the first device studies in this chapter, Device 3 from sample 8 in Table 4.1. Magnetic field direction,  $B$ , is indicated as well as gate potentials  $V_{g1,g2}$ . Image is taken by A Vekris at  $V_{Acc} = 5$  kV.

### 5.4.2 Characterization of DNW Josephson Junction Devices

In this chapter I will focus on an analysis on the Fabry-Pérot regime for the device depicted in Fig. 5.5. I have, however, taken part in an analysis of the Coulomb blockaded regime resulting in the publication *Josephson junctions in double nanowires bridged by in-situ deposited superconductors* from Vekris et al.<sup>85</sup> This paper can be found in Appendix B.4.



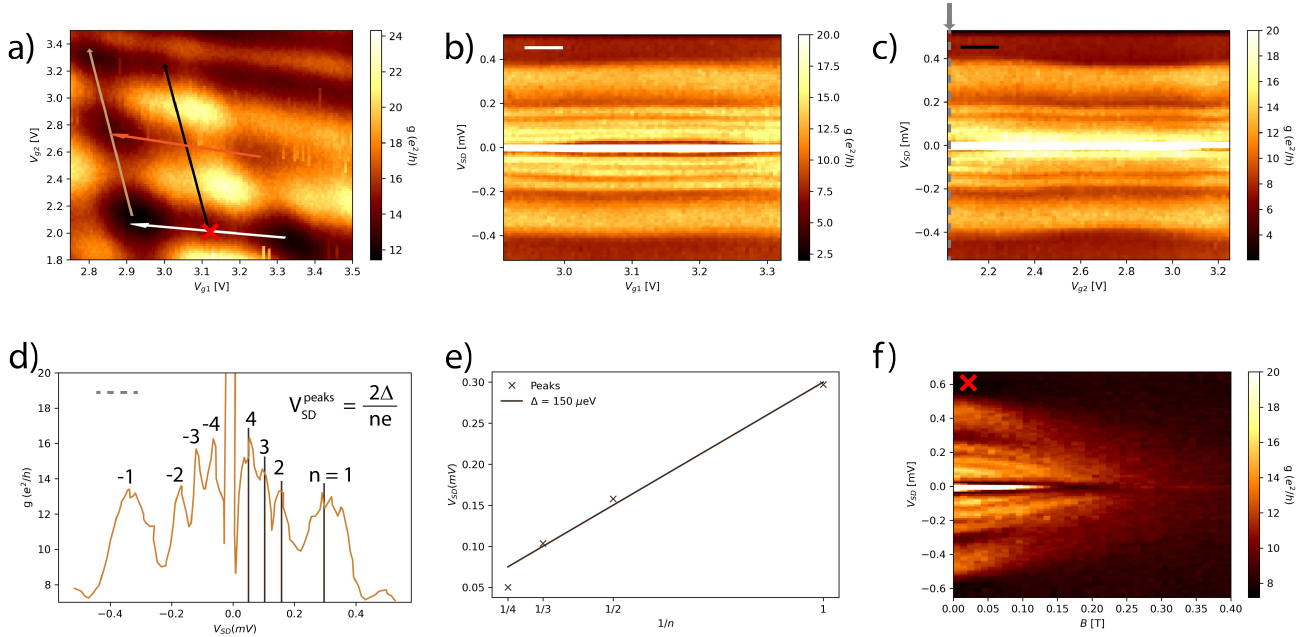


**Figure 5.6: Voltage biased 2-terminal measurements of a DNW Josephson Junction.** a) is the conductance through the JJ as a function of gate potentials,  $V_{g1}$  and  $V_{g2}$ . The arrows depict the linecut corresponding to the bias spectra shown in b and c) as well as in Appendix Sec. B.2. It is measured at  $V_{SD} = 0.3 \mu\text{V}$ . b and c) is the differential conductance,  $g$ , as a function of bias potential,  $V_{SD}$ , and gate potentials,  $V_{g1}$  for b) and  $V_{g2}$  for c). The color in each upper left corner refers to the color of the corresponding arrow in a). d) is the differential conductance,  $g$ , as a function of bias potential, corresponding to the linecut depicted by the grey dashed line and the arrow above it in c). The peaks arise from MAR with the position in  $V_{SD}$  determined by the formula shown in the top right corner. To limit the noise, every tree values in f) was averaged after the peak localization. e) shows the extracted peak positions from d) (crosses) and the theoretical peak positions (line) for  $\Delta = 50 \mu\text{eV}$ , as a function of  $n^{-1}$ .  $n$  is the number of Andreev reflections when  $n \geq 2$ . For  $n = 1$ , quasiparticle transport is the main process. f) is the differential conductance,  $g$ , as a function of magnetic field,  $B$ , and bias voltage,  $V_{SD}$ . The features seems to approach zero-bias with increasing  $B$ -field. Measured at  $T = 30\text{mK}$ .

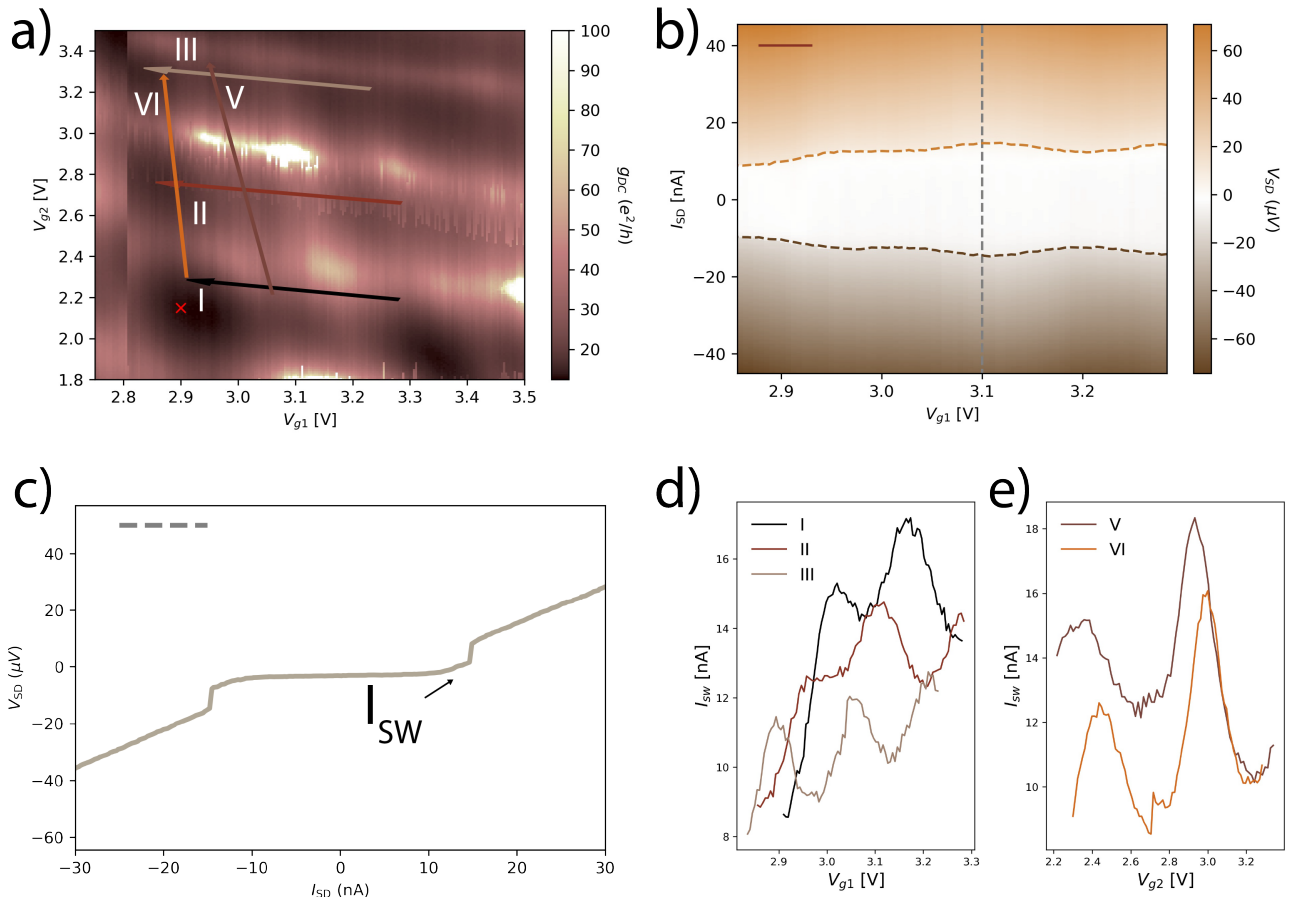
The device were brought into normal state, by applying a magnetic field on  $B = 400 \text{ mT}$ , a value that has shown to be the critical magnetic field,  $B_C$ . Here the differential conductance,  $g$ , were plotted as a function of gate potentials,  $V_{g1}$  and  $V_{g2}$ , to map out interesting regions. The gate map is displayed in Fig. B.2, where different regimes can be located.

Figure 5.6a) displays the conductance,  $g$ , through the JJ as a function of  $V_{g1}$  and  $V_{g2}$ , another gate map located just beside the one shown in Fig. B.2. This gate map is taken at  $V_{SD} = 0.3 \mu\text{V}$ . Resonances are visible as a function of  $V_{g1}$ , displayed as horizontal lines of current. The same tendency is visible as a function of  $V_{g2}$ , however in a more subtle degree. This indicates transmission through each NW, thus finite  $t_{1,2,3,4}$  and  $t_{1,2,3,4} \gg \Gamma_{NW}$ . However, since the resonance lines are not completely horizontal nor completely vertical,  $\Gamma_{NW}$  must be finite as the individual gate affects both  $t_1$  and  $t_2$ . Nonetheless, we can conclude that the two NWs acts separately and the system is indeed comprised by two parallel weak links. From the conductance-values, we can clearly refute the device being in the CB regime as there is clearly conductance even off resonance.

In Fig. 5.6b and c) the differential conductance,  $g$ , is plotted as a function of bias potential,  $V_{SD}$ , and gate potential, respectively  $V_{g1}$  and  $V_{g2}$ . The bias spectra corresponds to the white and black arrows on Fig.5.6a) is

displayed. Two similar plots are presented in Appendix Fig. B.3, corresponding to the brown and orange arrows in Fig.5.6a). One feature present in all four plots is a sharp peak at zero bias. We expect this to be supercurrent, and note that it is present in both NWs. Another feature, visible here is the high background conductance further emphasizing that we are definitely not in the Coulomb blockaded regime. Furthermore, what looks like multiple resonances in  $V_{SD}$  is visible in all the bias spectra. A linecut of Fig. 5.6c), illustrated by the grey dashed line by under the grey arrow, is shown in Fig. 5.6d). Here a Fabry-Pérot conductance peak structure looking very similar to those of Fig. 5.4b is shown, this is attributed to multiple Andreev reflections, the exact number of ARs determined by  $n$ . From the peaks the superconducting gap can be estimated,  $\Delta = 150_{-50}^{+30} \mu\text{eV}$ .

Figure 5.6e) displays the peak locations, of the peaks  $n = 1,2,3,4$ , in  $V_{SD}$ , extracted from Fig. 5.6d), as a function of  $n^{-1}$ . The crosses are the extracted peaks, while the line is the theoretical fit that can be found from



**Figure 5.7: Current bias of a DNW Josephson Junction.** a) is the differential conductance,  $g$ , through the JJ as a function of gate potentials,  $V_{g1}$  and  $V_{g2}$ . The red cross illustrated the point in gate voltages that Fig. ?? illustrates. The arrows depict the linecut corresponding to  $I_{SD}$  spectra as shown in b) from where the switching currents,  $I_{SW}$ , shown in d) and e) are extracted. It is measured at  $I_{SD} = 20$  nA. b) is the current bias,  $I_{SD}$ , spectra corresponding the linecut II depicted in a). The dark and light brown dashed lines in the spectra is traces of the  $I_{SW}$  for negative and positive  $I_{SD}$  respectively. The positive one is plotted in d) together with the corresponding horizontal traces from the other linecuts depicted in a). c) shows a linecut illustrated by the grey dashed line in b). In c) the  $I_{SW}$  is denoted. d) is the  $I_{SW}$  of the linecuts, I, II, and III shown as arrows in a) as a function of  $V_{g1}$ . e) is the  $I_{SW}$  of the linecuts, IV, V, and VI shown as arrows in a) as a function of  $V_{g2}$ . Measured at  $T = 30\text{mK}$ .

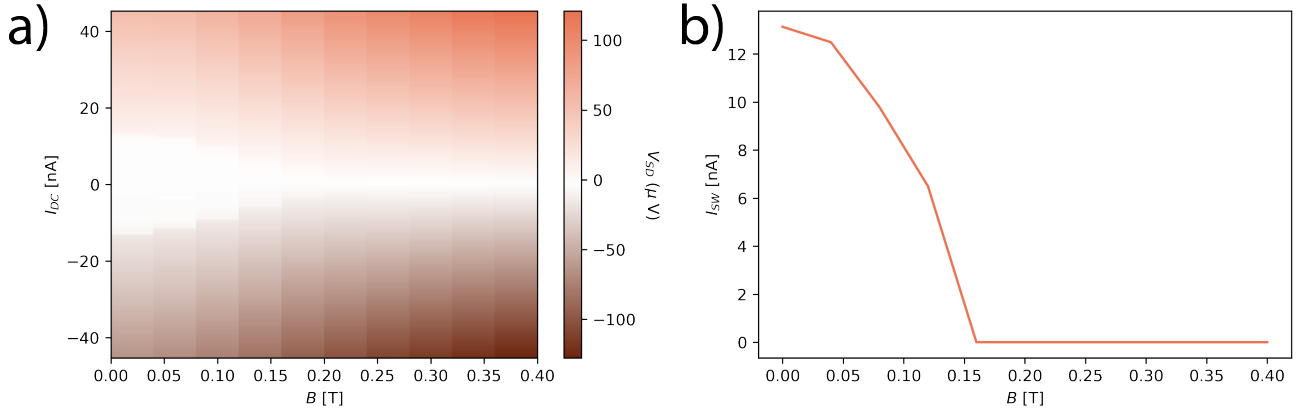


**Figure 5.8: Magnetic dependency of a DNW Josephson Junction.** a)  $V_{SD}$  as a function of  $I_{DC}$  and magnetic field,  $B$ . b) Extracted  $I_{SW}$  from a) as a function  $B$ . Measured at  $T = 30\text{mK}$ .

$\Delta = 150\mu\text{eV}$ . This correlation between the theoretical fit and the peak locations, adds to the verification that the JJ indeed shows superconductivity and MAR.

The differential conductance,  $g$ , is plotted as a function of bias potential,  $V_{SD}$ , and magnetic field,  $B$ , in Fig. 5.6f). Here, the same pattern as showed in 5.6b and d) can be seen at low  $B$ -values, but as  $B$  increase, the features are moving towards  $V_{SD} = 0$ . This is another sign of superconductivity, as the superconducting gap inhabiting the MAR states. At  $B \sim 0.16$  T, the superconductivity zero-bias peak appears quenched.

Figure 5.7a) shows the differential conductance as a function of gate voltages,  $V_{g1}$  and  $V_{g2}$ , for the same region in gate potential as in Fig. 5.6a). This was done with  $I_{SD} = 20$  nA, yielding greater conductances than in the voltage bias measurement. Here the resonances is visible again, but not as obvious as for the former figure. The arrows displays linecuts used to extract  $I_{SW}$  displayed in Fig. 5.7d and e) for respectively the horizontal I, II, III and vertical IV, V. In Fig. 5.7b), the voltage bias as a function of  $V_{g1}$  and  $I_{SD}$  is plotted for the II linecut. The grey dashed linecut, corresponds to the IV-curve (Voltage as a function of current) plotted in Fig. 5.7c). Here,  $I_{SW}$  is marked as the point in  $I_{SD}$  where the resistance,  $R$ , turns finite. The observation that  $R = 0$ , while  $I_{SD} \neq 0$ , is a clear sign of superconductivity. The  $I_{SW}$ -values from the Fig. 5.7b) and the four spectra, shown in Appendix Sec. B.3, corresponding to the other arrows in Fig. 5.7a), is extracted. The positive and negative  $I_{SW}$  for linecut II is plotted as the light and dark brown dashed lines in Fig. 5.7b).

All the positive  $I_{SW}$ -values are plotted in Fig. 5.7d and e) as a function of  $V_{g1}$  and  $V_{g2}$  respectively. In Fig. 5.7c) the resonances in  $T_{up}$  is quite apparent for segments of all three linecuts. Likewise Fig. 5.7d) displays resonances in  $T_{down}$ . Comparing the to plots, the resonance peaks in Fig. 5.7e) is sharper, indicating that  $T_{up}(t_1, t_2, V_{g1}) < T_{down}(t_3, t_4, V_{g2})$ .

In Fig. 5.8a) the potential over the JJ is plotted as a function of  $I_{DC}$  and magnetic field,  $B$ . A decrease in the zero-resistance area as the  $B$ -field increase is visible. Extracting  $I_{SW}$  and plotting it as a function of  $B$ -field, yield Fig. 5.8b). Here the  $I_{SW}$  is decreasing with increasing  $B$ -field until the superconducting gap is closed at  $\sim$

---

0.16 T. This further adds to the understanding that the JJ is indeed transporting supercurrent.

## 5.5 Conclusion on DNW Josephson Junctions

In conclusion, the production of a DNW Josephson Junction showing supercurrent has been achieved. This paves the way toward the isolation of EPR states applicable for teleportation of qubit states. In addition, the individual NW were found to transmit supercurrent with an induced superconducting gap at  $\Delta = 150_{-50}^{+30} \mu\text{eV}$ , determined by the conductance peak localization of MAR signatures in bias voltage.

Further studies could investigate the splitting of the Cooper pairs, inspired by the paper from Deacon et al.,<sup>20</sup> in the DWN JJ system. Additionally, subsequent transport of the electrons comprising the Cooper pair, increasing the spatial distance would be of major interest as well. This could potentially be achieved by combining the methods of Deacon et al.<sup>20</sup> with the Y-junction ideas applied by, amongst others, Hoffstetter et al.<sup>40</sup> An interesting experiment, could use DNWs in "Eiffel tower configurations, where one end of the DNW branch out for Cooper pair splitting. Then by increasing the distance between contacts, deposited on the individual NW, and the interface of the superconductor and observe at what distance the splitting efficiency dropped one could get an estimate of the entanglement distance between separated electrons in the Cooper pairs. This could be done on multiple devices with different superconductor-contact distances, or on a single device with multiple contacts deposited onto each out-branching leg. Then the intermediate contacts should just be left floating.

Another interesting perspective could be the optimization of such DNW Josephson Junction devices, applying the shadow-wall fabrication method presented by Heedt et al.<sup>38</sup>

---

## 6 Double-Nanowire Islands

In this chapter I will first describe the motivational perspectives of studying DNW Island devices, including a description of the topological Kondo effect as a smoking gun signature for the non-local dynamics of Majorana zero modes proposed by Béri and Cooper.<sup>11</sup> Then I will describe some important aspects in island devices, including charging energy and couplings. Following this, I will present some of the research representing a modern analysis of a superconducting island. Afterwards, a description of the fabrication and an characterization of the measurements of a DNW island device are presented, followed the modelling of quasiparticle excitations. At last it is concluded that the island is superconducting, and different approaches for optimization of the devices are proposed. During the investigation presented in this chapter I followed, and discussed, the measurements of the devices fabricated by Alexandros Vekris, without taking actual part in doing the measurements due to access restrictions associated with the Covid-19 pandemic. Furthermore I have done the theoretical descriptions and data analysis described in the chapter. Additionally, I also fabricated similar island devices as the ones shown in this chapter, but based on full-shell DNWs. However, as denoted in Table 4.1, they, the device on sample 1, were found to be not conducting.

### 6.1 Motivational perspectives in Double-Nanowire Island devices

The superconducting island geometry, also called a Cooper pair box, is expected to be a feasible platform for exotic phenomena such as Majorana braiding, which is a pairwise exchange of Majorana fermions, quantum computing and fusion-rule detection.<sup>1,37,51,86</sup>

Additional possible capabilities anticipated is magnetic tuning of the braiding,<sup>37</sup> detection of topological qubits,<sup>1</sup> and furthermore, performing teleportation-based measurements of topological qubits.<sup>86</sup> Thus, the development of the island devices as a Majorana platform would comprise a major step towards quantum computing and information processing. For instance a validation of a topological qubit would be a substantial step towards these goals as well as a demonstration of the non-Abelian braiding would.<sup>1</sup>

In 2012, Béri and Cooper<sup>11</sup> published an investigation showing how the nonlocal spins of Majorana fermions would give cause for a novel *topological Kondo Effect*. The Kondo Effect is the effect of coupling between lead electrons and quantum spin with degenerate



**Figure 6.1: Illustration of a topological Kondo Effect setup.** Graphical illustration of the simplest setup for detection of the topological Kondo Effect outlined by Béri and Cooper. In the middle, two parallel NWs are placed onto a superconducting Island. Three of the four NW ends are connected to normal leads and gates are used to tune the transport through the transparent parts of the NWs. A gate is meant to tune the levels of the island. At each part end of the NW-Island interface a Majorana state is formed giving rise to the topological Kondo Effect.

energy levels. The degenerate levels can arise from symmetries and fine tuned parameters resulting in fragile non-Fermi liquid (NFL) behaviour,<sup>66</sup> but in the topological regime the more robust degeneracy appear from the nonlocal attribute of the Majorana fermions. To calculate this topological Kondo Effect, the authors outlined a representation of the simplest potential setup, consisting of three normal leads, coupled to a superconducting island using parallel deposited semiconducting NWs, with Majoranas in each end of the Island-NW interface, as illustrated in Fig. 6.1. The state of the island as well as the lead-island couplings is tuned by gates not shown in the figure. An interesting feature of this setup is that since it needs all three NWs in the system, decoupling of one will result in the disappearance of the Kondo effect. Furthermore the analysis included the situation where more than four Majoranas were present, these stray Majoranas would not participate in the Kondo Effect as they are affiliated with uncoupled spins. The authors found the simple case to give rise to robust NFL behaviour concerning perturbations. Granted the signature of the disappearing topological Kondo effect by decoupling of a single out of three contacts, the study provides a clear test of the nonlocal Majorana fermion dynamics.

## 6.2 Introduction to SNW Island devices

An isolated piece of metal will give rise to a Coulomb potential, due to the electron-electron interactions in the metal. This limit the charge, that can be added through transport experiments to some integer of the elementary charge.<sup>48</sup> The Coulomb blockade arising from this phenomena is well-known and have been extensively studied in metallic islands as well as superconducting ones, the Cooper pair boxes.<sup>4,79</sup> The demonstration of  $2e$  quantisation in Al islands, indicating that the even-parity superconducting GS did not experience poisoning by quasiparticles on the time scale of measurement, was a breakthrough.<sup>32</sup> A few years later, the transition of  $2e$  quantisation to  $e$  quantisation as an effect of applied magnetic field were shown.<sup>53,80</sup> The magnetic field causes the Al to break down into the normal state.

From a bias spectra of a a superconducting island at zero magnetic field, as shown in 6.2, one can extract the addition energy,  $E_{\text{Add}}$ . This is the energy demanded to add one extra electron to the island, while situated in the Coulomb valley. Thus Coulomb diamonds have to be visible. Having even-odd parity Coulomb diamonds can make it necessary to extract the  $E_{\text{Add}}$  from two consecutive peaks. However, as we utilize in this chapter,

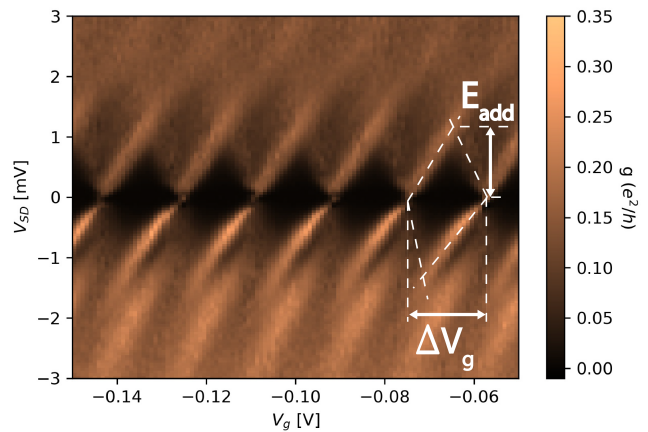


**Figure 6.2: Bias spectra analysis of a superconducting island.** Bias spectra of a superconducting island, at  $T = 30\text{mK}$ .  $E_{\text{Add}}$  is the addition energy and  $\Delta V_g$  the peak spacing.

for even-odd parity Coulomb diamonds with a very small difference in size, the charging energy can be roughly estimated by  $E_C \sim E_{\text{Add}}$ .

The coupling, a measure of how much the wave functions of the leads, involved in the specific configuration, and the island overlap, for a given measurement of an island is analogue to the Full Width Half Maximum (FWHM) in eV,

$$\text{FWHM}(\text{eV}) = \text{FWHM}(\text{V}) \alpha \quad (6.1)$$

Here the  $\text{FWHM}(\text{V})$  is that of a conductance peak in normal state measured in voltage and  $\alpha = \frac{E_{\text{Add}}}{\Delta V_g e}$  is the gate lever arm. The gate lever arm can be estimated from a bias spectra as shown in Fig. 6.2, where  $E_{\text{Add}}$  is the addition energy and  $\Delta V_g$  is the peak spacing. This applies for  $k_B T \ll \Sigma$ , which is the case in this chapter, where all measurements, except when noted, is taking place at  $30\text{mK} = 2.6\mu\text{eV}$ .

### 6.3 Status on the field of Island devices

Here, I will outline some interesting aspects of recent Island device research. This will be separated into two sections. The first section is about Quasiparticle excitations, because this, and especially the first paper presented, is very relevant for our analysis. The second section is about Majorana Islands, since this is highly debated subject in the field due to the MZM, that have exciting perspectives but are very difficult to validate.

### 6.4 Quasiparticle excitations

In September 2015, Higginbotham et al.,<sup>39</sup> presented how they managed to identify bound states in the semi-conducting part of a semiconductor-superconductor structure, using bias spectroscopy. Additionally, they determined the characteristic temperatures and magnetic fields for quasiparticle excitations, as well as eliciting a lower bound on poisoning time of the bound state in the semiconductor.

To achieve this they measured an NSN device, as depicted in Fig. 6.3a), consisting of a hexagonal InAs NW with Al on two facets in the device center, and Au contacts connected to each end of the NW. Gating was used on either side of the Al ( $V_{R,L}$ ) and global backgating to form Al-InAs hybrid quantum dot (HQD) in Coulomb blockade regime. Using bias spectroscopy, an obvious Coulomb diamond pattern in the conductance as a function of source-drain voltage difference and gate voltage as seen in Fig. 6.3b). The Coulomb diamonds witness about the single-charge addition happening in the HQD.

At low bias, a difference in even-odd Coulomb diamonds can be seen. Here negative differential conductance (NDC) is shown as the dark lines pointing in towards the diamonds showing that the island is occupied by an odd number of electrons. This parity-depending inverting subgap pattern at finite bias was a feature that, at the time, had not been presented before. From the repetition of the even-odd patterns, a parity-dependent bound state seemed to be continually filled and emptied with the addition of single electrons to the HQD. Due to

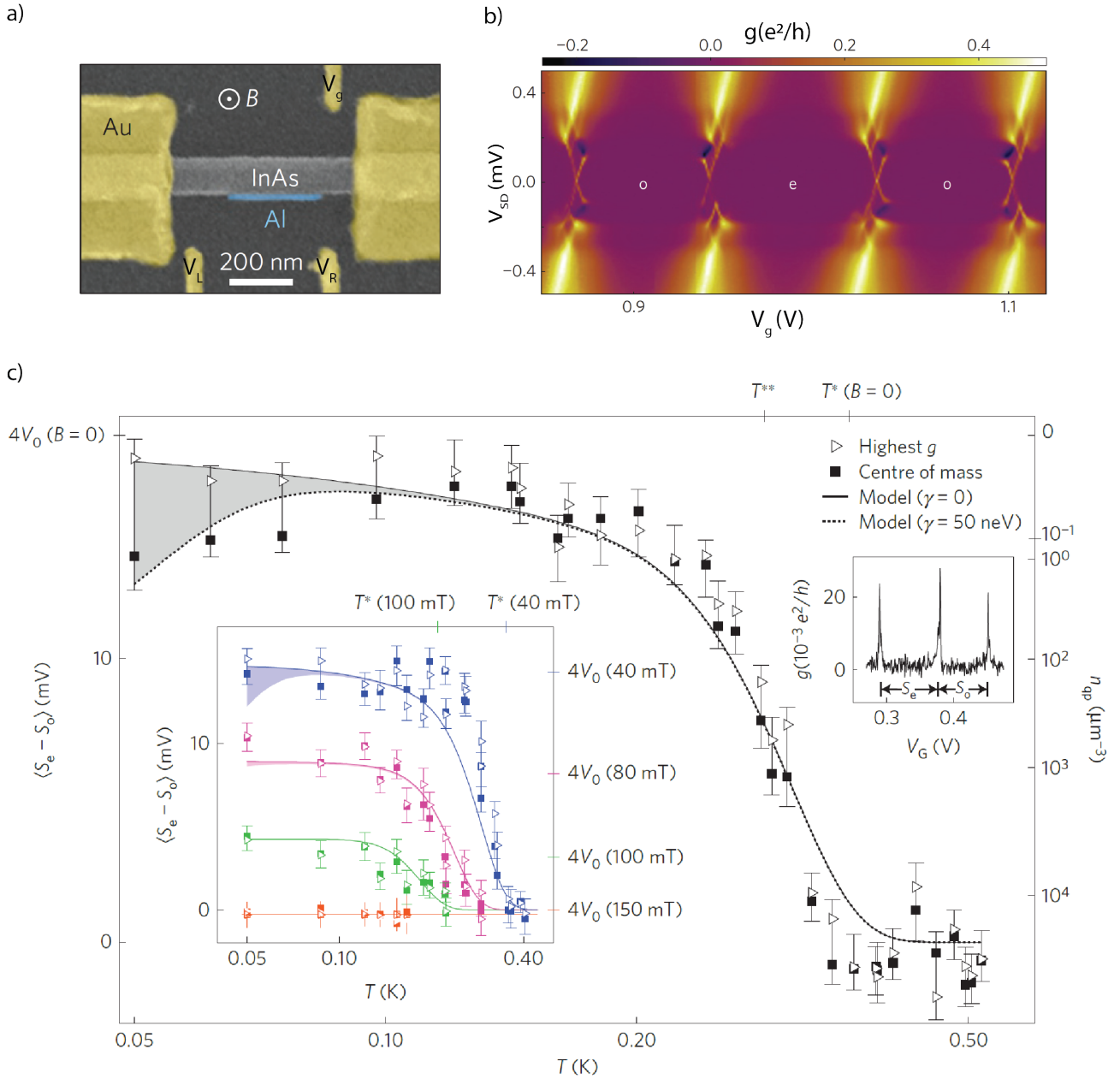


**Figure 6.3: Bond state analysis of a hybrid quantum dot (HQD).** **a)** SEM image of the HQD device, **b)** Differential conductance of the device as a function of bias and gate voltage.  $e = \text{even}$ ,  $o = \text{odd}$ . **c)** Average spacing between even and odd conductance peaks as a function of temperature. The  $\triangleright$  denotes the maxima of the peak and the  $\blacksquare$  the centroids with error bars being the standard deviation of the peak maxima. The solid line is found from Eq. 6.2 fitted to the centroid data with  $\Delta = 180 \mu\text{eV}$ ,  $E_0 = 58 \mu\text{eV}$ ,  $\alpha = 0.013$  and  $V = 7.4 \times 10^4 \text{ nm}^3$ . The dotted curve include a 50 neV discrete state broadening, fitted to the centroid data. The right axis visualizes the quasiparticle density of Al and the temperatures for quasiparticle activation ( $T^*$ ) and crossover ( $T^{**}$ ) is indicated on the top axis. Furthermore, the spacing expected from lower Zeeman-split bound state,  $4V_0(B)$ , is indicated on the left axis. The left inset is the same as the main figure, but for magnetic fields  $B = 40, 80, 100$  and  $150$  mT. The curves are fitted with  $g$ -factor,  $g = 6$ , and superconducting critical field,  $B_c = 160$  mT, as shared parameters and the other parameters fixed from the main figure. The right inset is a conductance plot as a function of gate voltage,  $V_G$ , illustrating the origin of the peak spacings. Adapted from Higginbotham et al.<sup>39</sup>

the conductance happening in narrow patterns showing symmetry around zero bias, transport through a bound state was deduced and a simple model, based on transport through a single state in the InAs coupled with a



Bardeen-Cooper-Schrieffer (BCS) continuum in the Al, were proposed. In this model, multiple simplifications were applied. First, a fixed-energy bound state, based on the repetitive Coulomb diamond pattern, second, symmetric couplings between the leads and the bound state as well as continuum. Additionally, transition rates were calculated from Fermi's golden rule and state occupancies were found from steady-state Pauli master equations. The energy of the state where found, using finite bias spectroscopy, to be  $E_0 = 58\mu\text{eV}$ . From the onset of NDC, the superconducting gap ( $\Delta = 180\mu\text{eV}$ ) were estimated using that  $eV_{\text{SD}} = \Delta - E_0$ . Furthermore, the coupling to the leads ( $\Gamma_0 = 0.5\text{ GHz}$ ) and the normal state conductance from each lead to continuum ( $g_{\text{Al}} = 0.15e^2/h$ ), was estimated. A feature that the model were unable to describe was the broadening at high bias, the enhancement of same feature correlated with NDC, as well as peak-to-peak changes in the slope of NDC patterns.

The NDC is a result of slow particle escape in a blockade caused by electron tunneling into the BCS continuum. As the electron is placed in the BCS continuum it blocks for transport until it itself escapes through the leads. As it can be expected from this, the authors found that the NDC was only compatible with the model for long quasiparticle relaxation times ( $\tau_{\text{qp}} > 0.1\mu\text{s}$ ).

At zero bias, alternations between large and small spacing in-between the peaks were observed. Both elevated temperatures and magnetic field, tended to erase the peak spacing alternations. The magnetic field dependence were consistent with the aluminum transition from superconducting to metal. In contrast, the temperature dependent disappearing, of the peak spacing alternations, took place at  $T > 0.4\text{K}$ , considerably lower than the superconducting critical temperature ( $T_c \sim 1\text{K}$ ). This dependence is comparable to that of metals, and can be described as thermal activation of quasiparticles in the HQD. To further describe the evolution of the peak spacing alternation, they applied a model including thermal quasiparticle excitations, based on a discrete subgap state and the BCS continuum. In this model the peak spacing could be described as:

$$S_e - S_o = \frac{4}{\alpha e} (F_o - F_e) \quad (6.2)$$

Here  $F_o$  &  $F_e$  is the free energies of the odd and even occupancies respectively and  $\alpha$  is the gate lever arm. The difference in free energy can be written in as a function of partition functions,  $Z$ :

$$F_o - F_e = -k_B T \ln \left( \frac{Z_o}{Z_e} \right) \quad (6.3)$$

The ratio of the partition functions depends on the density of states in the HQD,  $D(E)$ ,

$$\frac{Z_o}{Z_e} = \int_0^\infty dE D(E) \ln \coth \left( \frac{E}{2k_B T} \right) \quad (6.4)$$

Where  $D(E)$  is one subgap state and the continuum. If  $\Delta \gg k_B T$ , the free energy difference can be written as:

$$F_o - F_e \approx -k_B T \ln(N_{eff} e^{\frac{-\Delta}{k_B T}} + 2e^{\frac{-E_0}{k_B T}}) \quad (6.5)$$

With  $N_{eff}$  being the effective number of continuum states for Al, with volume  $V_{Al}$  and electron density of states  $\rho_{Al}$ ,

$$N_{eff} = \rho_{Al} V_{Al} \sqrt{2\pi k_B T \Delta} \quad (6.6)$$

In this model two characteristic temperatures,  $T^* \sim \Delta/[k_B \ln(N_{eff})]$  &  $T^{**} \sim \Delta - E_0/[k_B \ln(N_{eff}/2)]$  can be identified.  $T^*$  is the temperature, smaller than the gap and  $E_0$  independent, above which the peak spacing alternation should disappear. The lower  $T^{**}$ , is the temperature at where the bound state affects the even-odd alternation, leading to saturation at lower temperatures.

The model including the two characteristic temperatures is visualized in Fig. 6.3c). Here the experimental values are found by averaging over a set of 24 sequential peaks spacings. A drastic drop in spacing difference is initialised at around 0.2K until 0.4K where the spacing difference is gone. The saturation amplitude is close to the measured bound state energy,  $4V_0 = 4E_0/(\alpha e)$ . The model itself, based on Eq. 6.2, shows quite good agreement with the data. In this fit they used a independently determined density of states, determined from the data while they applied the volume as fitting parameter, consistent with the micrograph in 6.3a). Due to asymmetry in the peak shapes, the centroids ("Centre of mass" in the figure) were more regularly spaced than the maxima ("Highest g"). This is visible in Fig. 6.3c) with the centroid points, decreasing with decreasing temperatures for around  $T < 0.16K$ , whereas the maxima points remain flat. The dip in the centroid point could be explained as thermal broadening of the bound state, but the authors could not however, explain how this is connected with the centroid-maxima difference. In Fig. 6.3c) the broadening is shown as the dotted lines with a value on  $\gamma = 50neV$ , considerably close to the estimated coupling to the leads ( $(\hbar\Gamma_0)^2/\Delta = 20neV$ ).

Applying a magnetic field perpendicular to the plane of the device, as drawn in Fig. 6.3a), reduces the temperature at which the alternating even-odd spacings starts to occur ( $T_{onset}$ ) as well as the temperature at which they are saturated ( $T_{sat}$ ). Additionally the amplitude of the alternations is decreased as well by the magnetic field. To include this into the model, field dependence by Zeeman splitting of the bound state as well as orbital reduction of the gap were accounted for. Here the g-factor ( $g = 6$ ) was used as fitting parameter. This value is in the typical range for InAs NWs, a fact that further reinforce the rationalization that the bound state is located in the InAs. The results of these field dependence inclusions is shown in the inset in Fig. 6.3c).

The consistency between data and the model imply that the array of even-odd spacings can facilitate a measure

of the equilibrium quasiparticle density found as

$$n_{qp}(T) = \frac{N_{eff}^2}{V_{Al}} e^{-2\Delta/k_B T} \quad (6.7)$$

for large charging energies. In Fig. 6.3c), the quasiparticle density is shown on the right axis. Below  $T_{sat} \sim 0.2K$  however, the spacing saturates, making the quasiparticle density difficult to decipher. Thus, the authors took the conservative value  $n_{qp}(T_{sat}) \sim 0.1\mu m^{-3}$  to be the upper cap of the quasiparticle density for small temperatures. Due to the small aluminum volume, the upper cap of the number of quasiparticles is correspondingly small. At last, the authors located a lower cap of the poisoning time ( $\tau_p$ ). The physical meaning of poisoning is the relaxation of a quasiparticle into the InAs from the Al, preserving the general parity of the HQD, but not the one of the bound state. Finding the quasiparticle relaxation time from quantitative analysis of the NDC at finite bias, led to the lower cap on the poisoning time of the bound state,  $\tau_p > 10ms$ .

Later that year, in December 2016, Albrecht et al.<sup>3</sup> published a paper on quasiparticle poisoning in a Majorana Island with  $L \sim 400$  nm as seen in Fig. 6.4a). In the experiment magnetic fields were applied perpendicular to the NW axis, in both in-plane ( $B_{tr}$ ) and out-of-plane ( $B_{\perp}$ ) directions. The critical fields in the two directions were found to be  $B_{c,\perp} \sim 0.7$  T and  $B_{c,tr} \sim 0.2$  T. The island was gated by  $V_G$  and the other gates depleted the  $\sim 50$  nm regions of the NW, without Al, between the island and the contacts. Taking the density of state to consist of a single subgap state at energy  $E_0$  and a Bardeen-Cooper-Schrieffer (BCS)-like continuum, Albrecht et al.<sup>3</sup> defined the total number of charges,  $N$ , on the island as:

$$N = 2N_{cp} + N_{\Delta} + N_0 \quad (6.8)$$

Here,  $N_{cp}$  is the number of Coulomb pairs on the island,  $N_0 = 0, 1$  the occupancy of the subgap state and  $N_{\Delta}$  the number of quasiparticles in the BCS continuum. However this is only for thermal energies lower than the charging energy,  $E_C$ . The charge state energies of the corresponding

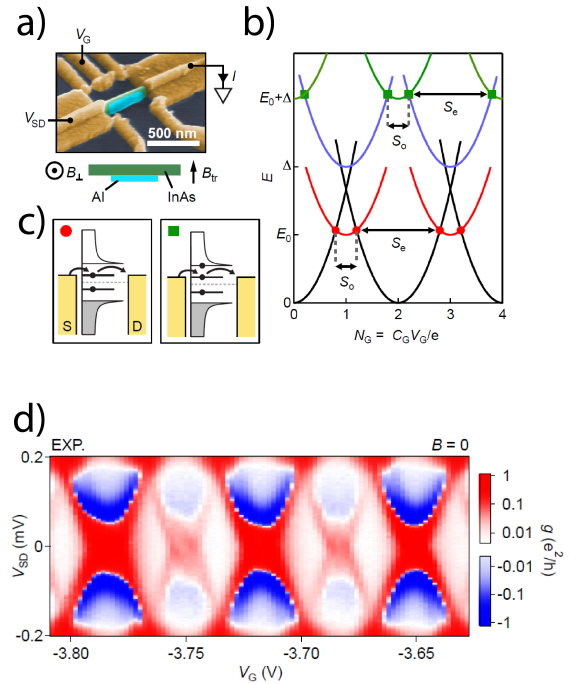


**Figure 6.4: Quasiparticle excitations in a Majorana Island.** a) Shows a false color electron micrograph of the device on top with illustrated materials and magnetic field directions below. b) is the island charge-state energies as a function of charge induced by the gate,  $N_G$ . Degeneracy spacings are indicated as  $S_e$  and  $S_0$ . c) is the schematics of the processes of same color and sign in b). d) is the experimentally measured differential conductance,  $g$ , as a function of  $V_{SD}$  and  $V_G$  at zero magnetic field. The spectra reveals a set of  $2e$ -periodic Coulomb diamonds with a weaker set of diamonds offset  $1e$  from the main diamonds. Adapted from Albrecht et al.<sup>3</sup>

charge occupation numbers were defined as:

$$E(N_{cp}, N_{\Delta}, N_0) = \frac{E_C}{2}(N_G - N)^2 + N_{\Delta}\Delta + N_0E_0 \quad (6.9)$$

where it is assumed that all quasiparticles in the BCS-continuum are relaxed to gap energy  $\Delta$ .  $N_G = C_G V_G/e$  is the gate-induced charge on the island with  $C_G$  the capacitance between the side gate and the island. Assuming that  $E_0 < E_C/2 < \Delta$ , the spectrum is displayed in Fig. 6.4b) as a function of  $N_G$ . Having even  $N$ , the pure condensate state  $(N_{cp}, 0, 0)$ , displayed in black, is the lowest available charge state followed by the green-colored state,  $(N_{cp}, 1, 1)$ , with an occupied subgap state and a single quasiparticle in the BCS continuum. Having odd  $N$ , the red and blue states corresponding to respectively  $(N_{cp}, 0, 1)$  and  $(N_{cp}, 1, 0)$ .

In Fig. 6.4b) low-temperature transport without quasiparticle poisoning is occurring at the charge-state degeneracies denoted by red circles. These processes are illustrated in the left panel of Fig. 6.4c) and corresponds to:

$$(N_{cp}, 0, 0) \rightleftharpoons (N_{cp}, 0, 1) \ \& \ (N_{cp}, 0, 1) \rightleftharpoons (N_{cp} + 1, 0, 0) \quad (6.10)$$

As it can be seen on Fig. 6.4b), the even and odd peak spacings are dependent on  $E_0$ , and such, the even odd spacing is proportional to  $E_0$ . This can be used for tracking of subgap states into the Majorana regime as showed in the before-mentioned article from Albrecht et al.<sup>2</sup>

Having quasiparticle excitations, the green and blue parabolas of Fig. 6.4b) come into play. This scenario corresponds to  $N_{\Delta} = 1$  and with transport at the green squares in Fig. 6.4b) and the transport cycles, as depicted in Fig. 6.4c), described as:

$$(N_{cp}, 1, 0) \rightleftharpoons (N_{cp}, 1, 1) \ \& \ (N_{cp}, 1, 1) \rightleftharpoons (N_{cp} + 1, 1, 0). \quad (6.11)$$

For the island to return to the unpoisoned state several processes can take place including Cooper pair recombination  $(N_{cp}, 1, 1) \rightarrow (N_{cp}, 0, 0)$ , relaxation of a quasiparticle into a subgap state  $(N_{cp}, 1, 0) \rightarrow (N_{cp}, 0, 1)$ , as well as quasiparticle tunneling to a lead  $(N_{cp}, 1, N_0) \rightarrow (N_{cp}, 0, N_0)$ . The poisoning rates, relaxation rates and the coupling of the subgap states to the source and drain leads,  $\Gamma_{S,D}$ , affects how high a conductance that should be measurable from Eq. 6.11. Thus, the conductance height can yield information of quasiparticle poisoning and relaxation rates. In addition, it can be predicted from Fig. 6.4b) that the peak spacing for the poisoned states will be equal to the ones for the unpoisoned states, but with a  $1e$  shift in gate voltage.

To see these poisoning conductance signatures, Albrecht et al.<sup>3</sup> lowered the barrier between the island and the source and drain leads compared to the experiment from March the same year.<sup>2</sup> The result of this tweak is an increase in  $\Gamma_{S,D}$  and quasiparticle poisoning rates. Thus, the conductance signatures should increase as well.

Just as predicted, Fig. 6.4d) shows the differential conductance,  $g = dI/dV_{SD}$ , as a function of  $V_G$  and  $V_{SD}$  at

zero magnetic field. Here, two sets of Coulomb diamonds can be seen. One set of high conductance diamonds ( $g_m \sim 0.5 e^2/h$ ) and another set with lower conductance ( $g_s \sim 0.03 e^2/h$ ) shifted  $1e$  from the high-conductance diamonds. The high-conductance diamonds shows obvious even-odd occupancy alternations as well as NDC at finite bias. The almost vanished odd diamonds witness about the energy of the subgap state,  $E_0$  being only slightly smaller than  $E_C/2$ . Albrecht et al.<sup>3</sup> expected these low-conductance diamond to be an attribute of quasi-particle poisoning. Comparing the data with at rate-equation model yielded a poisoning time,  $\tau_p = 1.2 \mu s$ , for electron- ( $(N_{cp}, 0, N_0) \rightarrow (N_{cp}, 1, N_0)$ ) and holelike ( $(N_{cp}, 0, N_0) \rightarrow (N_{cp}-1, 1, N_0)$ ) excitations in the BCS continuum.

## 6.5 Majorana Islands

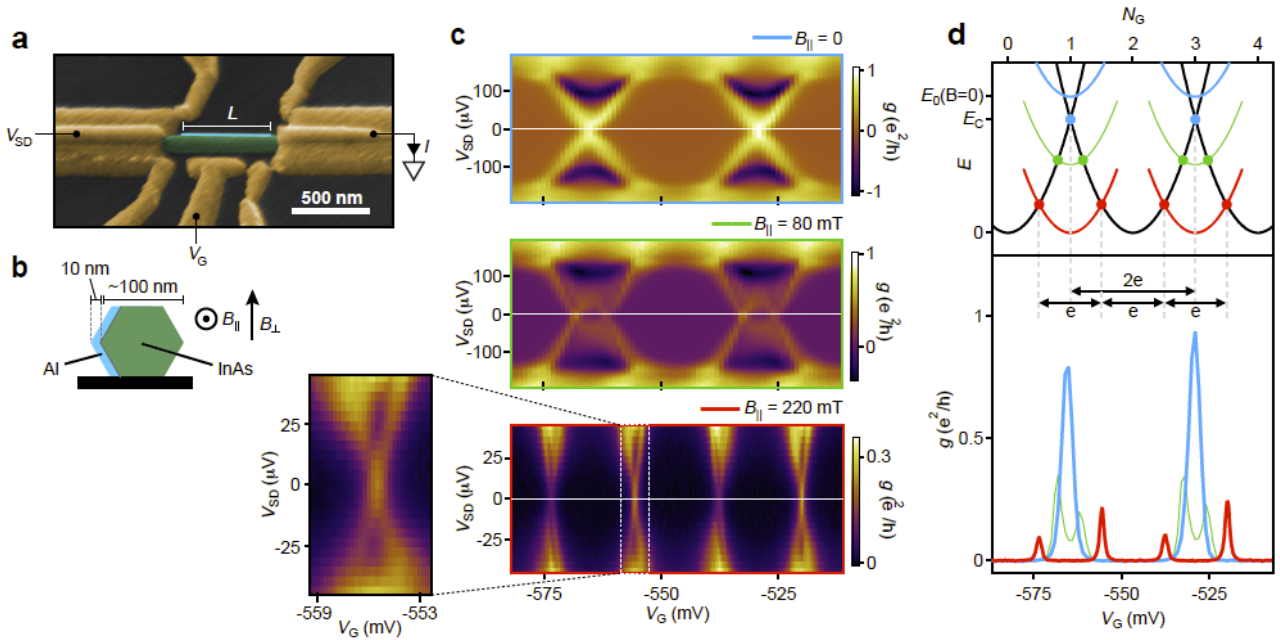
In March 2016, Albrecht et al.<sup>2</sup> published an investigation on InAs NWs with a thin (8-10 nm) aluminum island on two facets as shown in Fig. 6.5a. The thin aluminum increase the critical fields, along the wire axis,  $B_{C,\parallel} \sim 1$  T, and roughly in-plane with the Al-covered facets,  $B_{C,\perp} \sim 700$  mT. Both directions are illustrated in Fig. 6.5b. The magnitude of these critical field values qualifies the NWs as a platform for investigations into topological superconductivity.

Figure 6.5c displays three differential conductivity,  $g$ , maps as a function of source-drain voltage,  $V_{SD}$ , and gate voltage,  $V_G$ , for at device with  $L = 790$  nm. The positions of the applied voltages is indicated in 6.5a. The upper  $g$ -map is made without any magnetic field applied and shows diamonds consistent with Cooper pair charges, as they have a gate voltage period proportional with  $2e$ . Applying a moderate magnetic field leads to shrinking of the diamonds, creating a second set of diamonds in an even-odd occupancy pattern, as shown in the middle  $g$ -map. Further increasing the magnetic field strength yields the  $g$ -map in the bottom. Here,  $1e$  periodic Coulomb diamonds is visible with resonance structures indicating transport through discrete resonant levels at low bias while transport through continuum at high bias as enhanced in the magnification. These high magnetic field Coulomb blockade conductance peaks at zero bias with half the zero field periodicity in addition to a discrete subgap spectrum could be a signature of electron teleportation by Majorana end states, Albrecht et al. mentions.<sup>2</sup> Thus, they designate ungrounded tunnel devices in high magnetic field with subgap states near zero energy, isolated from the continuum, that shows  $1e$  periodic Coulomb blockading in conductance as "Majorana Islands" (MI).

The mechanism of the change from  $2e$  to  $1e$  periodicity, can be explained by a simple zero-temperature model, as illustrated in the top of Fig. 6.5d. Here we see the even ground state (GS) energies as the black parabolas and the odd as the colored parabolas. At zero magnetic field, the GS energy of the odd occupancy (blue parabolas) are higher than the intersection between the even GS energies (defining the charging energy). Thus, the current only runs in the even-even transitions and thus the conductance peaks with  $2e$  parity as illustrated in the panel

below. Increasing the magnetic field however, decrease the GS energy of the odd occupancy, yielding the even-odd regime, where the distance, in gate voltage, between conductance peaks for odd occupancies is smaller than that of the even occupancies. Further increasing the magnetic field, leads to a zero-energy GS for the odd occupancies, and thus an equal distance between conductance peaks transitioning from odd or even occupancies. This yields the  $1e$  periodicity. The blue, green and red plots in the bottom panel of Fig. 6.5d, correspond to the line cuts through zero-bias in Fig. 6.5c and have conductance peaks consistent with the model in the upper panel.

Looking further for Majorana signatures, Albrecht et al.<sup>2</sup> now investigated a device with  $L = 0.9 \mu\text{m}$ . They found the conductance as a function of  $V_G$  and  $B_{\parallel}$ , to identify the splitting of 10 consecutive peaks. These peaks, they averaged separately for even and odd occupation to produce the plots shown in Fig. 6.6a. Here it is visible that the splitting starts to occur at around 110 mT, leaving a difference in magnetic field on  $\sim 500\text{mT}$  before the critical magnetic field on  $\sim 600\text{mT}$ . This indicates a near zero energy state within the superconducting regime in the range of  $\sim 500\text{mT}$ . Another feature that can be seen in Fig. 6.6a, is the oscillations in even-odd peak spacing around the  $1e$  periodic value, as a function of magnetic field. This is consistent with a oscillating GS energy caused by hybridized Majorana modes.<sup>18,67,75</sup> Figure 6.6b shows the oscillation amplitude, measured as shown in Fig. 6.6a, for devices with five different  $L$ -values. This follows the expected exponential tendency as characteristic for the topological protection of Majorana modes.



**Figure 6.5: Characterization of a Majorana Island Device.** **a** SEM image of the MI device, **b** Schematic of the cross-section of the hexagonal NW, with indications of magnetic field directions, materials and dimensions. **c** Differential conductivity maps as a function of  $V_{SD}$  and  $V_G$ . The parallel magnetic fields increase from the top to the bottom map,  $B_{\parallel} = 0, 80, 220$  mT. Be aware of the changes in range of the  $V_{SD}$  axis in the bottom plot. **d** shows the energy,  $E_N$ , as a function of normalised gate voltage,  $N_G$ , in the top panel, and differential conductance,  $g$ , as a function of gate voltage,  $V_G$ , in the bottom panel. Adapted from Albrecht et al.<sup>2</sup>

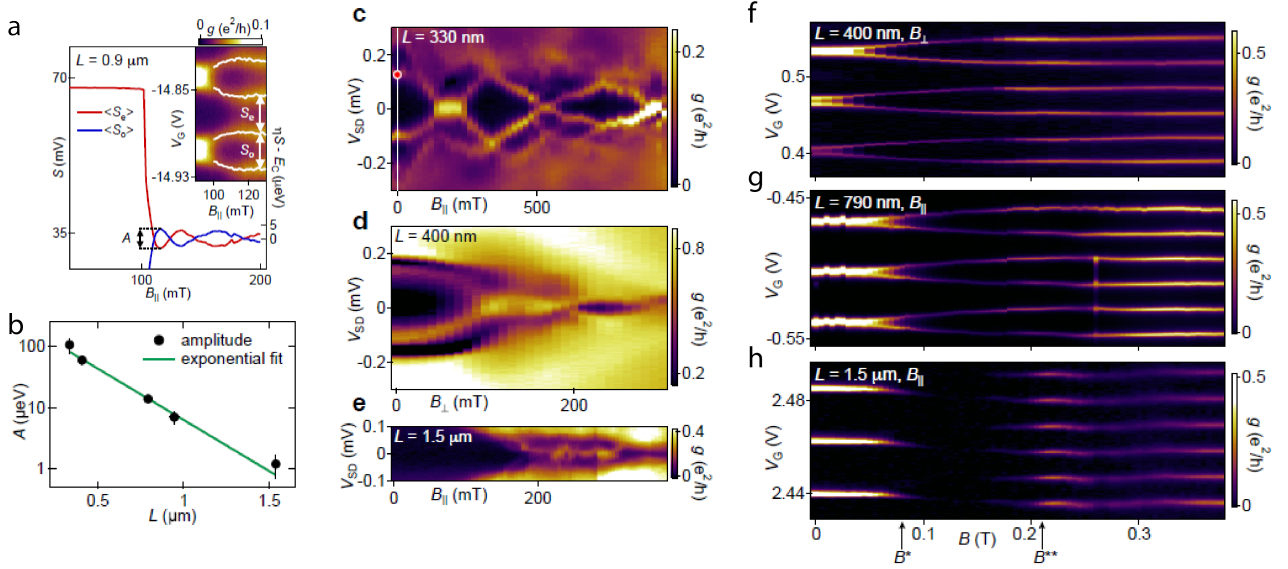


**Figure 6.6: Length dependencies of Majorana Island Devices.** **a** Average even and odd peak spacing of Coulomb valleys as a function of  $B_{\parallel}$ . The spacing becomes  $\langle S_e \rangle = \langle S_o \rangle$  at  $B = 110$  mT, whereafter it oscillates around that spacing. The right axis is energy in terms of  $E_0 \propto \eta S - E_C$  with  $\eta$  being the gate lever arm, **b** Amplitude of the first oscillation,  $A$ , as indicated in **a**, as a function of Al shell length,  $L$ . The black data points resembles data from 5 devices of  $L$  between 330 nm to  $1.5 \mu\text{m}$ , the green line is an exponential fit  $A = A_0 \exp(-L/\xi)$ , where  $A_0 = 300 \mu\text{eV}$  and  $\xi = 260$  nm. Error bars indicate uncertainties from lever arm measurements and fits to peak maxima. **c** Conductance as a function of magnetic field,  $B_{\parallel}$ , and source-drain voltage for a device with  $L = 330$  nm **d** Same as **c** but with magnetic field  $B_{\perp}$  and  $L = 400$  nm. **e** Same as **c** but with  $L = 1.5 \mu\text{m}$ . **f-h** Conductance as a function of gate voltage magnetic fields,  $B_{\perp}$  for **f** and  $B_{\parallel}$  for **g** and **h**. From **f** to **h**, the devices measured has  $L = 400$  nm, 790 nm, 1.4  $\mu\text{m}$ . The Coulomb peaks decrease in height at  $B^*$  and increase in height  $B^{**}$ , especially for the longest device. Adapted by Albrecht et al.<sup>2</sup>

Figure 6.6c-e shows bias spectra, as a function of magnetic field, for three devices with different  $L$ -values. The short one, Fig. 6.6c, shows the discrete states moving linearly in magnetic field. The states pass through zero and merge with a continuum at  $V_{SD} \sim 100 \mu\text{eV}$ . Due to unprotected parity crossings and state intersections at high energy as a result of spin-orbit coupling being quenched, this merging of the states and continuum is expected for Majorana systems in the short-length limit. Increasing  $L$  to medium length, Fig. 6.6d, shows the subgap state bend back towards zero after the crossing through zero. Again, this is expected Majorana behavior as the system length is increased. The long device, Fig. 6.6e, shows a bias spectra with a zero-energy state isolated from the continuum at higher bias. This state is displayed for a range in magnetic field of 120 mT.

The increase of device length, leading to the change from unprotected parity crossing to a fixed zero-energy state through energetically isolated oscillating states, is consistent with the crossover expected from a strongly overlapping precursor of split Majoranas to a Majorana state locked at zero energy by topological protection.<sup>67,75</sup> However one unexpected thing within the simple Majorana description, is the disappearance of the discrete state above  $B_{\parallel} = 320$  mT in Fig. 6.6e. The measured gap at high field, between the near-zero-energy state and the continuum,  $\Delta_T \sim 30 \mu\text{eV}$  is consistent with topological superconductivity. So is the coherence length,  $\xi \sim 260$  nm, extracted from the exponential fit in Fig. 6.6b,  $A = A_0 e^{-L/\xi}$ .

At last, Albrecht et al.<sup>2</sup> changed their focus to the Coulomb blockade peak heights as a function of magnetic field, as displayed in 6.6f-h. Here they showed that until  $B^*$ , the peaks were uniform in heights and started splitting from  $2e$  periodicity. Between  $B^*$  and  $B^{**}$  the peak height decreased rapidly, especially for longer islands (Fig. 6.6h). Above  $B^{**}$ , marking the  $1e$  periodicity, the peak heights recovered.

This onset of uniform spacing and rematerializing of the peak heights from  $B^{**}$ , indicates the appearance of one or more zero-energy states with strong wave function support at the ends of the wire. These phenomena are consistent with teleportation of electrons from one end to the other of the wire, by a Majorana mode.<sup>31,41</sup> It is however, not necessarily a signature of this,<sup>70</sup> and such, the investigations by Albrecht et al.,<sup>2</sup> cannot rule out the opportunity of other end-localized zero-energy states appearing above the critical field.

In the paper published by Albrecht et al.<sup>3</sup>

in December 2016 they also reported on the magnetic field dependence of the transport through the MI, Fig. 6.7a) shows the zero-bias differential conductance as a function of  $B_{\perp}$  and  $V_G$ . Here both low- and high-conductance peaks displays an increase in odd Coulomb valley spacing until  $B_{\perp} \sim 0.16$  T, at what point the mean even and odd spacings are equal and the two sets of peaks merged. Figure 6.7b) furthermore shows how the direction of the field affects the MI. In the top left, the zero-bias differential conductance as a function of  $B_{\perp}$  and  $V_G$  is shown again, but for a broader range of  $B_{\perp}$ . In the top right, it is the same thing but with  $B_{tr}$  instead. Here the merging of the high- and low-

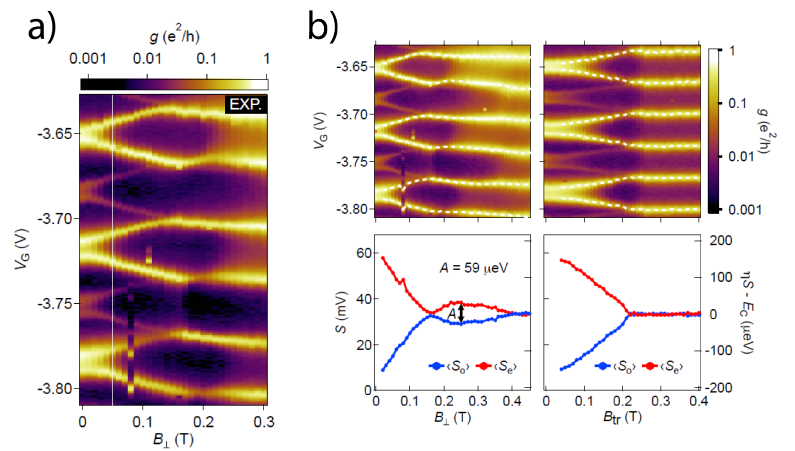


**Figure 6.7: Magnetic dependence on the Coulomb peak spacings.** a) Shows the perpendicular Magnetic field and gate potential dependence on the differential conductance. Showing a set of strong Coulomb peaks spaced by  $2e$  and a weaker set of peaks shifted by  $1e$  with respect to the strong peaks. b) Top panel: Shows the differential conductances as a function of gate potential and magnetic field in perpendicular and traversal direction respectively to the left and right. The white stripes in the center of the conductance peaks, indicates the fit positions used to calculate the average Coulomb peak spacings for the two sets of even and odd valleys. Bottom panel: Mean peak spacings for even and odd Coulomb valleys as a function of the same magnetic field as the spectra above. The left y-axis is gate potential and the right is the associated energy scale  $\eta S - E_C \propto E_0$ . Adapted from Albrecht et al.<sup>3</sup>

conductance peaks seems to happen at  $B_{tr} \sim 0.22$  T, a substantially stronger field than for  $B_{\perp}$ . Since this merging takes place in the range of the critical field of this direction, the merging, and simultaneous transition from  $2e$  to  $1e$  periodic spacing, is likely to be caused from destruction of superconductivity. Under each field map, the corresponding valley widths are plotted. Here, the left one shows oscillation after the merging of the conductances, with an amplitude,  $59 \mu\text{eV}$ , close to the expected value for devices of  $L = 400$  nm with hybridized Majorana modes, estimated from the exponential function presented in the before mentioned article from earlier the same year.<sup>2</sup> Thus, hybridized Majorana modes are indicated even though the data was part of the data pool



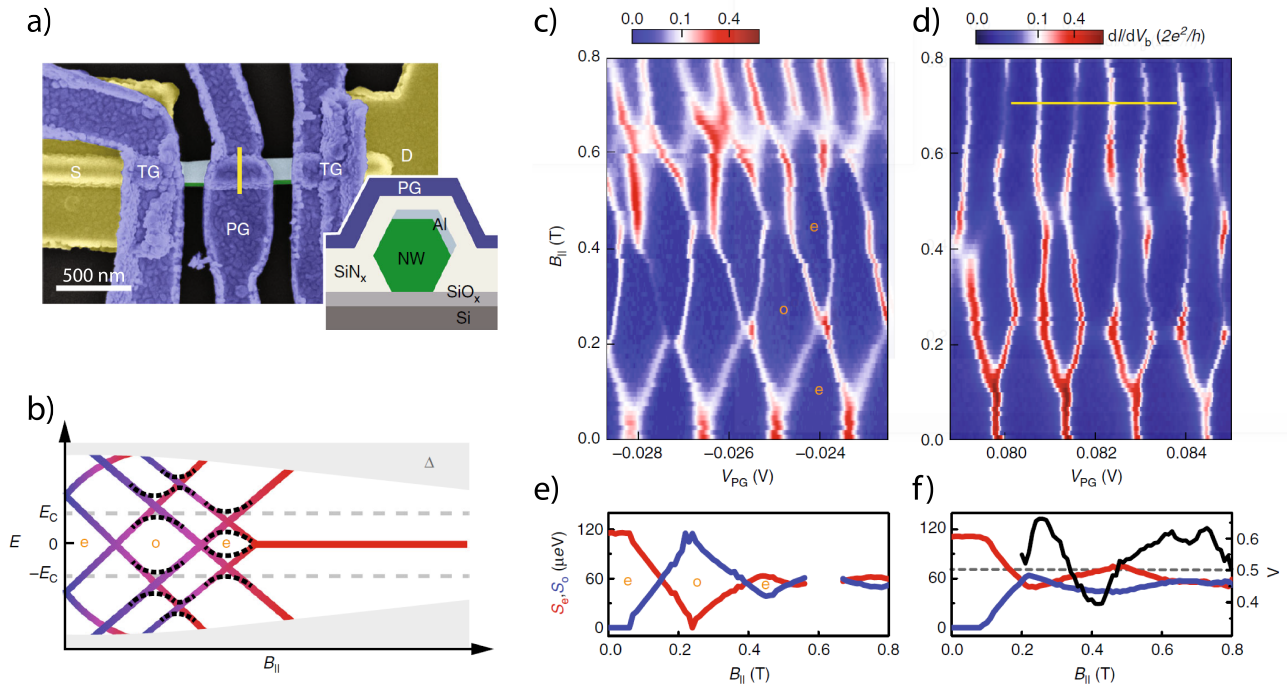


**Figure 6.8: Magnetic dependencies of multiple subgap states.** a) is a false color SEM image of the InSb NW based device, the cross-sectional illustration in the lower right corner is illustrating the area indicated by the yellow line in the SEM image. b) is a schematic of the magnetic field dependence of three subgap states with even-odd parity transition in the GS for every zero-energy crossing. The dashed line indicates the level repulsion between the subgap states, that leads to  $E_0$  oscillations. c-d) shows two different scenarios of differential conductance as a function of gate voltage and magnetic field reflecting b) in c) the even (e) and odd (o) are labelled. e) is the extracted peak spacings of the valleys labelled in c). f) is the average peak spacings (red and blue) and the average height ratio (black) over the three periods in d). Adapted from Shen et al.<sup>73</sup>

yielding the original exponential function. In the lower right, there is no oscillation after the merging of the peaks, further indicating that this scenario is describing the destruction of superconductivity. The bending of the average even and odd spacing furthermore yields information. In the upper parts of Fig. 6.7b), the left plot shows outwards bending before the merge, while the right plot shows inward bending. The outward bending tendency is consistent with theoretical models of subgap states as they approach the topological phase transition towards Majorana modes.<sup>18,67,75</sup> In contrast, the inward bending suggests closing of the superconducting gap. In 2018, Shen et al.<sup>73</sup> published an investigation revealing distinct types of fermion parity transitions, in this case in an Coulomb blockaded InSb-Al island, as displayed in Fig. 6.8a). Similar to the formerly described cases, this was happening as a function of gate voltage and magnetic field. The reason for the use of InSb is the large  $g$ -factor  $\approx 50$ , which should cause the induced gap in the semiconductor to close and re-open long before the closing of the original superconducting gap in the superconductor. This yielded additional transitions induced by the magnetic field.

Through varying the top-gate,  $V_{PG}$ , located above the Al island, the authors found three phases. The first phase, with even-parity GS, was found by applying a negative voltage on  $V_{PG}$ , pushing the wave functions against and

in some degree into the AI. This results in a robust induced gap with only a faint sensitivity to the B-field. Thus, there's no parity change. The second phase was found by turning to a positive voltage on  $V_{PG}$ , broadening the wave functions further into the InSb. An indication of this were the estimated g-factor of InSb  $\sim 7-15$ . This resulted in a parity-change from even-parity to a novel odd-parity GS as the magnetic field were increased. Ramping up the positive voltage on  $V_{PG}$  even further, the third phase were revealed. In this phase the g-factor were found to be  $\sim 10$ . As the magnetic field were increased, a robust zero-energy mode were found at B-fields substantially lower than the critical field of the AI. They attribute this to be either an Andreev bound state stabilized at zero bias or a MZM.

Larger numbers of GS transitions as a function of magnetic field for the third phase are illustrated in Fig. 6.8b). Here several zero-energy crossings happens at lower values of  $B_{\parallel}$  succeeded by a stable zero-energy state at elevated  $B_{\parallel}$ . Real examples of this is shown in Fig. 6.8c-d), where large oscillations is shown for  $B_{\parallel} < 0.6$  T, whereafter they for c and d stabilize in  $1e$ -periodicity above 0.7 T and 0.6 T respectively. Figures 6.8e) and 6.8f) each visualizes this oscillations even more distinct, corresponding to the respective subfigure located above it. The authors furthermore found, that the low B-field signatures was often tunable by  $V_{PG}$  to a quite precise degree, while the high B-field signatures tended to be very weakly dependent on  $V_{PG}$ . Thus the  $1e$ -periodicity seemed to originate from a state with a high robustness against gate variations. Furthermore, the alternation in conductance peak heights, shown as the black line in Fig. 6.8f) and defined as  $\Lambda = \frac{G_{e \rightarrow o}}{G_{e \rightarrow o} + G_{o \rightarrow e}}$ , is clearly visible in both  $2e$  and  $1e$  regime in Fig. 6.8d). This feature is a result of different tunneling probability of holes and electrons in the subgap states. An interesting feature of  $\Lambda$  in Fig. 6.8f) is that according to an idealised model on Majorana Zero Modes (MZMs) in a wire of finite length,  $\Lambda$  should have a minimum or maximum at  $S_e = S_o$ , and should be  $\Lambda = 0.5$  at  $|S_e - S_o|$ .<sup>35</sup> In the figure, the spacing and conductance oscillations indeed are similar in number and period suggesting a connection between the two.

## 6.6 Double-Nanowire Island Devices

The realization of detecting MZMs in DNW island devices are expected to demand multiple parameters to be fulfilled. First, the DNWs, with large g-factors and strong spin-orbit coupling, should be grown. This was realized by Kanne et al.<sup>43</sup> already before the onset of this Masters project. Second, the achievement of producing a strongly coupled superconducting island on the DNW structure needs to be achieved, since Majorana states are edge states living in the interface between some super- and semiconductors. Additionally, the NWs must not be interacting with each other. Third, a substantially large critical magnetic field strength,  $B_C$ , is needed to provide the opportunity of closing the induced superconducting gap in the part of the semiconductor, that are experiencing proximity effect from the superconductor, using an external magnetic field. Fourth, and last, the large g-factor should be utilized to close the induced gap before the original gap of the superconducting material,

followed by reopening of the induced gap utilizing the spin-orbit coupling of the semiconductor. This reopening is supposed to be the transition into the topological superconducting phase. The topological phase is expected to contain pairs of MZMs, harbouring either one or zero fermions allowing both odd- and even-parity ground states.

### 6.6.1 Fabrication of DNW Island Devices

To investigate whether a superconducting DNW island device were feasible, multiple devices of the design seen in Fig. 6.9a) were fabricated. As illustrated, the devices were made by two parallel DNWs with Al epitaxially grown on three facets, taken from the even parallel facet to facet 20 dot (diameter,  $D \sim 85$  nm) 200 nm spacing area as displayed in Fig. 4.3. The aluminum were selectively etched as described in Sec. 4.4-4.5, followed by deposition of the displayed gates and contacts using selective deposition as described in Sec. 4.4 and 4.6. Figure 6.9c) displays an electron micrograph of one of such

DNW Island devices.  $V_G$  is used to tune the levels of the island of length,  $L \sim 315$  nm, while the other gates upholds Coulomb blockade.

### 6.6.2 Characterization of a DNW Island Device

As visualized in Fig. 6.9b), we can model the island devices as a spatially confined superconducting island, with four couplings,  $\Gamma_{1,2,3,4}$ , each to one of the four NW ends. However, we have another type of coupling too, the NW interlead coupling,  $\Gamma_{\text{left},\text{right}}$ , for each side of the island.

During measurement of a DNW Island device, six different 2-terminal measurement configurations were used, as illustrated in the insets of Fig. 6.10. Note that the terminals, when not applied, were left floating.<sup>1</sup>

The arrows indicate the idealized electron paths, of which the differential conductance as a function of gate potential, plotted in the main figures, is measured. In reality, it is expected that the electrons is more spread out into the Al, and in some extend, capable of tunneling straight through one NW to the other due to the finite  $\Gamma_{\text{left},\text{right}}$ . Figure 6.10 additionally shows the differential conductance as a function of plunger gate potential for each measurement configuration.

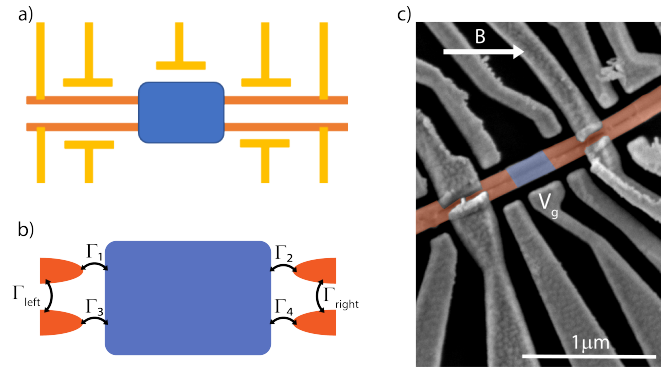


**Figure 6.9: DNW island devices.** a) Schematic of the DNW island devices, that consists of two parallel DNWs (orange). On the NWs Al is epitaxially grown followed by selective etching, leaving only an island of Al (blue). Finally Ti/Au contacts are deposited onto each end of each NW and Au gates are deposited to tune the NW-island couplings as well as the state of the island. b) Model of an DNW Island device, with  $\Gamma_{1,2,3,4}$  being the couplings between the superconducting island and each of the four NW ends, and  $\Gamma_{\text{left},\text{right}}$  being the interlead couplings on each side of the island. c) is a false-color SEM of the first device studies in this chapter, the Q2. Magnetic field direction,  $B$ , is indicated as well as  $V_g$ . Image is taken by A Vekris at  $V_{\text{Acc}} = 5\text{kV}$ .

<sup>1</sup>It would be better to pinch off the terminals, but it was not possible due to gating issues.

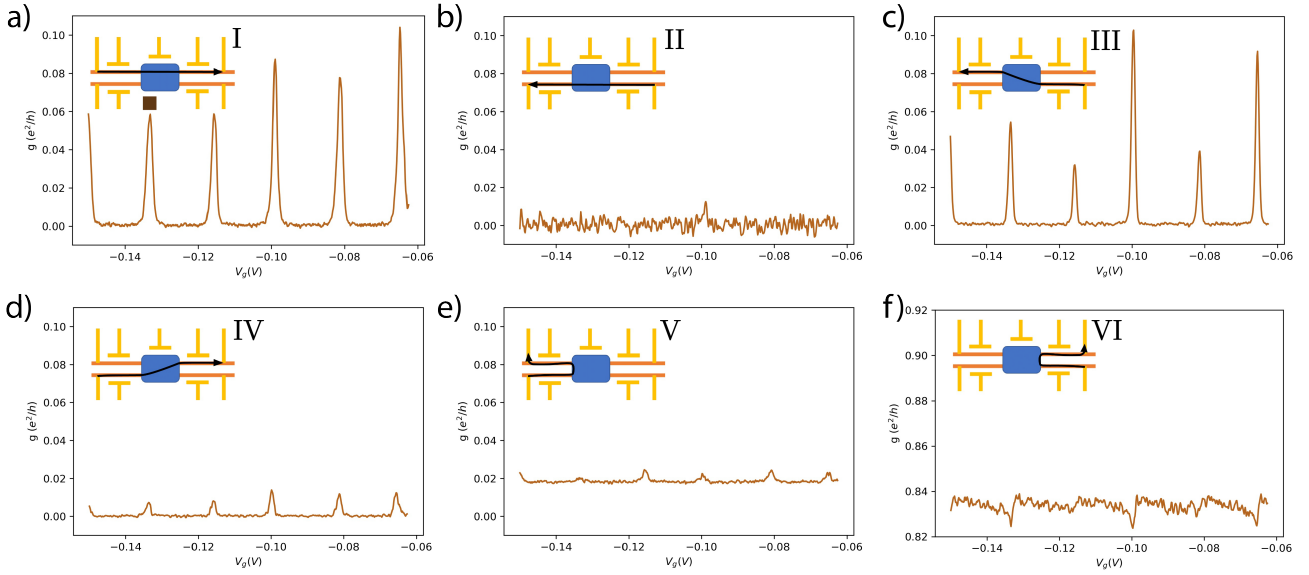


**Figure 6.10: Zero bias differential conductance (linear conductance) traces as a function of gate voltage.** Six different contact configurations were applied (as illustrated in insets with idealized electron paths indicated by the black arrows). The configurations are denoted as a) I, b) II c) III, d) IV, e) V, and f) VI respectively. I, III, IV and V shows clear conductance peaks while, II and VI is more noisy, V and VI both have significant background conductance. Measured at  $V_{ac}$  amplitude  $V_0 = 5 \mu\text{V}$ . Measured at  $T = 30\text{mK}$ .

In the configuration I, Fig. 6.10a), measuring the differential conductance through only the top wire, Coulomb peaks are visible. Configurations III, IV, and V, Fig. 6.10c-e) shows Coulomb peaks too, demonstrating that we have managed to fabricate the first Coulomb blockaded DNW island device and measure the effect in four different 2-terminal contact configurations. Furthermore, the peaks in all the configurations are placed at the same point in  $V_g$ , hence indicating that the Coulomb blockaded object is the same for all the situations. In Appendix Sec. C.1, the zero bias traces for the configurations has been grouped by the couplings they each resemble. Here all the zero-bias traces related to  $\Gamma_3$ , configuration II, IV and V that is, seems to be lower or more noisy than the zero-bias traces not related to  $\Gamma_3$ . This indicates that  $\Gamma_3$  is somewhat asymmetric compared to the other couplings. The troughs in VI could be caused by Fano resonances or maybe an artifact of the RC-filters. When the island is on resonance, the current can run to the falsely assumed floating contacts and into ground through the RC filter that alone has an impedance,  $Z \sim 765 \text{ k}\Omega$  at 77Hz. This results in a differential conductance drop being measured between the two contacts applied for the 2-terminal measurement.

In Fig. 6.11, the base conductances of each configuration as well as the main five peak heights, the couplings and a particular normalized peak, denoted by the brown square in Fig. C.6a), for configuration I, III, IV and V are plotted. A graphical representations of the peaks, base conductances and FWHM used to find the coupling, plotted with the zero-bias traces, can be found in appendix Sec. C.1 for all six configurations. Starting with Fig. 6.11a), the base conductance can provide a rough estimate of the amount of interlead coupling,  $\Gamma_{\text{left,right}}$ . As the figure displays, the base conductance is almost zero for all configurations up until V. At configuration V, the base conductance increase to  $g_{\text{base}} = 0.018 e^2/h$  indicating an increase in interlead coupling. Looking at the inset

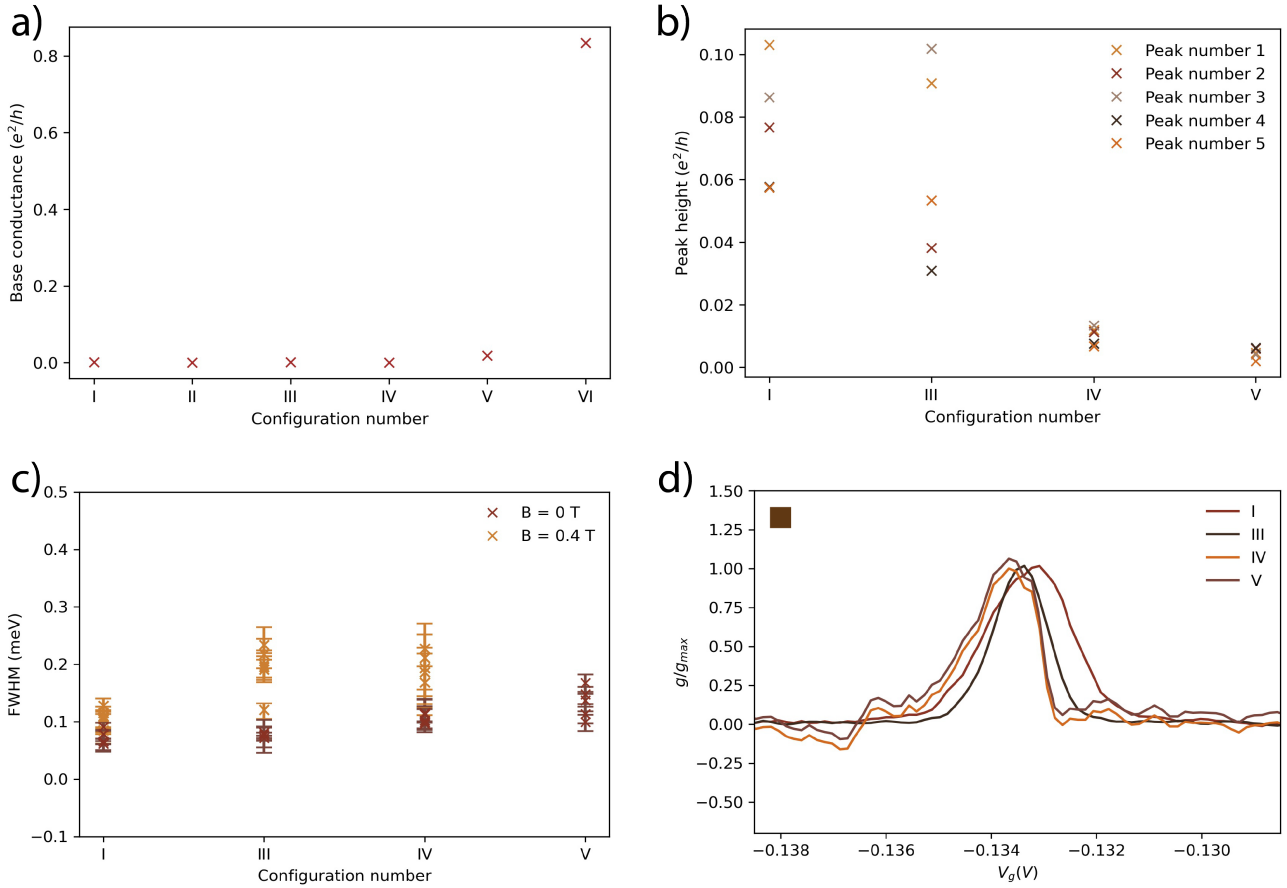


**Figure 6.11: Details from the Zero-bias plots.** a) is the background conductance for the six different configurations, found by taking the averages of all points, except the ones higher than a visually determined threshold, that defines the datapoint above this value as part of a peak. b) is the peak height of the five most prominent peaks for each zero-bias trace. c) is the FWHM of each configuration using the peaks also used in b), to convert them into energies the gate lever arm  $\alpha$  were estimated by  $V_{Add}$  and the peak spacing,  $\Delta V_g$  as described in Sec. 6.2. This is for  $B = 0$  T and  $B = 0.4$  T in.  $B = 0.4$  T is not plotted for configuration V, since the data did not show Coulomb diamonds. The uncertainties are caused by the manual estimation of  $E_{Add}$  divided by the differences in gate potential,  $\Delta V_g$ , as visualized in Fig. 6.12, and multiplied by the FWHM.  $\alpha$  were found from each individual FWHM value, why the uncertainties vary even though they are systematic. d) displays a single Coulomb peak, visible in all configurations, normalized by the peak heights. The origin of a) and b) is shown in appendix Sec. C.1. The peaks and FWHM are found using the `scipy.signal.find_peaks`<sup>22</sup> in python. This function finds all local maxima by simple comparison to neighbour values and can be further tuned by different parameters such as peak prominence which is a measure of how much the peak stand out compared to the surrounding baseline.<sup>23</sup> Thus the uncertainty is incorporated in the data points in a) and b).

in Fig. 6.10e), the current runs only on the left side of the device, allowing  $\Gamma_{left}$  to be a relevant factor. Figure 6.11a) furthermore yields an even greater increase in base conductance for configuration VI,  $g_{base} = 0.833 e^2/h$ . Repeating the method the inset in Fig. 6.10e), shows that the current runs only on the right side of the device, this time allowing  $\Gamma_{right}$  to be a relevant factor, and even a greater one. From the plots in Appendix Sec. C.1, we can furthermore see that the peaks of configuration II is concealed by the base conductance to a degree that makes it unfit for the further analysis. The troughs in configuration VI is not taken into account either, as they are merely an artifact of the transport rather than actual Coulomb peaks.

Figure 6.11b), shows the heights of the five main peaks for each of the different configurations and thus provide

information about the coupling symmetry, i.e. how similar the tunnel barriers for the individual island-NW couplings are. If the couplings are symmetric, having resonances at the same gate voltage, we expect to see a large peak. However if they are asymmetric, with resonances at unequal gate voltages, we expect small peaks. For a perfect symmetry we would expect the peaks to be  $2e^2/h$ . Configuration V has the smallest conductance peaks, showing just very small peaks which we attribute to lowering by the interlead coupling,  $\Gamma_{\text{left}}$ . At last, configuration I and III have largest peaks. The involved couplings are  $\Gamma_1$ ,  $\Gamma_2$ , and  $\Gamma_4$ , agreeing with the understanding that they are more symmetric relative to each other than to  $\Gamma_3$ .

In Fig. 6.11c), the FWHM for all the configurations are shown at zero magnetic field as well as configuration I, III and IV at magnetic field,  $B = 0.4$  T. The FWHM increase with increasing coupling, which is a measure of how much the charge carrier wave functions of the parts involved in the specific measurement overlap. Here, all the FWHM values are the same within the experimental uncertainty. This implies that the object that the charge carriers travel through is the same for all the configurations. The finite field value is chosen as it corresponds to the critical magnetic field.

Figure 6.11d) displays a zoom-in on a specific peak for the four configurations, normalized with respect to peak height to allow us to compare the peak geometry. All the normalized peaks looks very similar, further emphasising the paths through the same object.

From Fig. 6.11 it can be inferred that the FWHM provide a reasonable estimate for the couplings of the different configurations. However, due to the large interlead couplings,  $\Gamma_{\text{left, right}}$ , the path that the charge carriers utilizes cannot be assumed as described in the insets of Fig. 6.10. A possible solution for this could be to include corrections in well-known formulas for such zero bias traces, as described in 2-terminal by Van Heck et al.<sup>81</sup> However, another solution, which were found the most time efficient, were to further study this device in depth, in order to utilize the knowledge achieved in fabrication of a new DNW Island device batch.

Figure 6.12 display the differential conductance as a function of source-drain bias and gate potential, for the same six configurations as illustrated in Fig. 6.10. The general tendency of these spectra is Coulomb diamonds, especially apparent in the configurations, I and III, that had clear zero-bias Coulomb peaks in Fig. 6.10.

In configuration I, the resonances seems to follow the edges of the diamonds and continue into the continuum. The bias spectrum of configuration II does not yield the same evident type of Coulomb diamonds. It does however, show similar resonances, compared to configuration I. These resonances nevertheless seems to disappear near zero bias. Configuration III display a high-contrast bias spectrum with clear Coulomb diamonds. The resonances seems to continue straight into the continuum without any apparent features. Opposed to configuration III, configuration IV yields weaker Coulomb diamonds. At last, for configuration VI, there's no visible Coulomb diamonds, due to the interlead coupling for this configuration, which allows the electrons to run through the wires without entering the island.

In configuration II between  $V_{\text{SD}} \sim -1.2$  mV and  $V_{\text{SD}} \sim -2$  mV (highlighted by the brown square), the conduc-

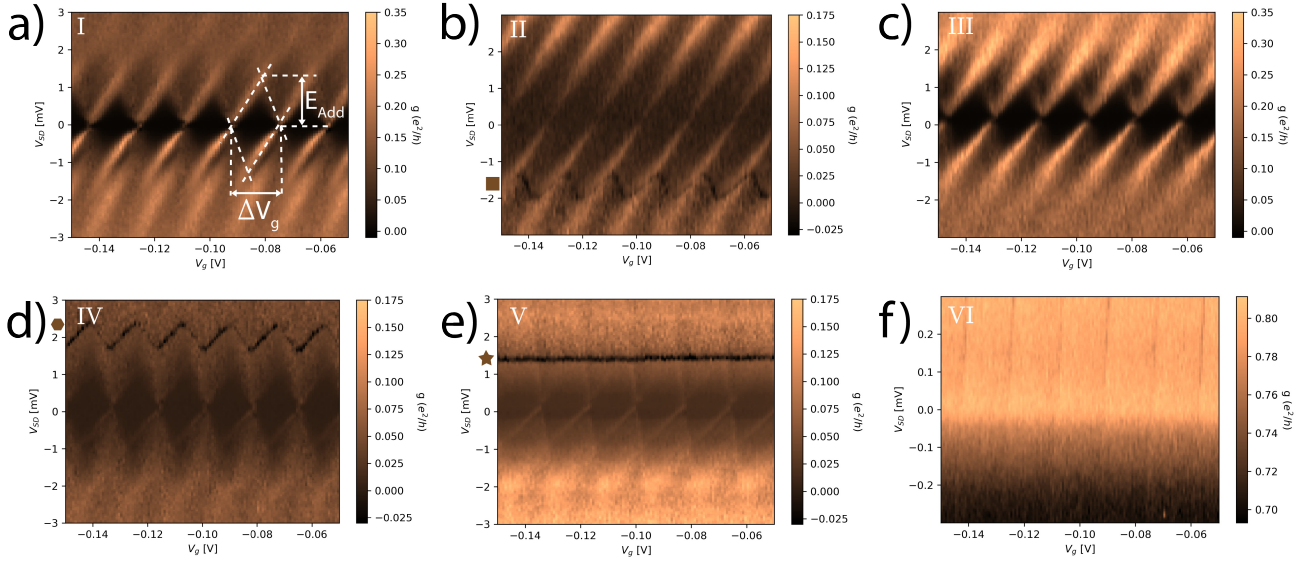


**Figure 6.12: Bias spectra of the six contact configurations.** Differential conductance as a function of bias and plunger gate voltage, measured at  $T = 30\text{mK}$ . The configurations are denoted as a) I, b) II, c) III, d) IV, e) V, and f) VI respectively. I, III, IV and V shows relatively clear Coulomb diamonds while, II and VI is more noisy. NDC can be seen in a gate dependent pattern in II and IV, while it is visible in V without any gate dependency.

tance drop to negative differential conductance (NDC) in a wavelike pattern in bias as a function of gate voltage. This indicates a state of quasiparticle excitation, yielding the NDC, connected to the charging of the island, yielding the gate-dependence. Configuration IV yield the same wavelike NDC structure as configuration II, but this time between  $V_{SD} \sim 1.8\text{ mV}$  and  $V_{SD} \sim 2.5\text{ mV}$  (highlighted by the brown hexagon) and with higher magnitude. The bias difference between the two situations is caused by the current of the two configurations being measured in reverse directions, displayed in the insets of Fig. 6.10b & d). Given the more apparent Coulomb peaks in configuration IV, compared to configuration II, it becomes visible that the wavelike NDC structure follow the Coulomb diamonds. The Coulomb diamonds in configuration V are not very visible, but at the top of them, in bias  $V_{SD} \sim 1.4\text{ mV}$  (highlighted by the brown star), a horizontal line of NDC is displayed. This line of NDC thus seems to be rather independent of the charging of the island, indicating that it is somehow related to the interlead coupling in configuration V.

The gate lever arm were furthermore estimated from configuration I, III, IV and V, followed by averaging, to be  $\alpha = 0.066$ . Only  $B = 0\text{ T}$  was used to find the average  $\alpha$ . Additionally we can estimate  $E_C \sim 1.1\text{ meV}$  from  $E_{Add}$  as described in Sec. 6.2.

One feature, that is slightly visible in the linear conductances vs. gate potential of Fig. 6.10, is that every second distance between the peaks, for configuration I, III, IV and even vaguely indicated in V, is larger than the one before. This is the even-odd spacing alternations that were measured by Higginbotham et al.<sup>39</sup> This phenomena can also be seen in the bias spectra. Figure 6.13a) shows a zoom-in on the near zero bias region of the configuration III bias spectra. Here the even-odd spacing is more apparent. Similar to the SNW findings of Higginbotham

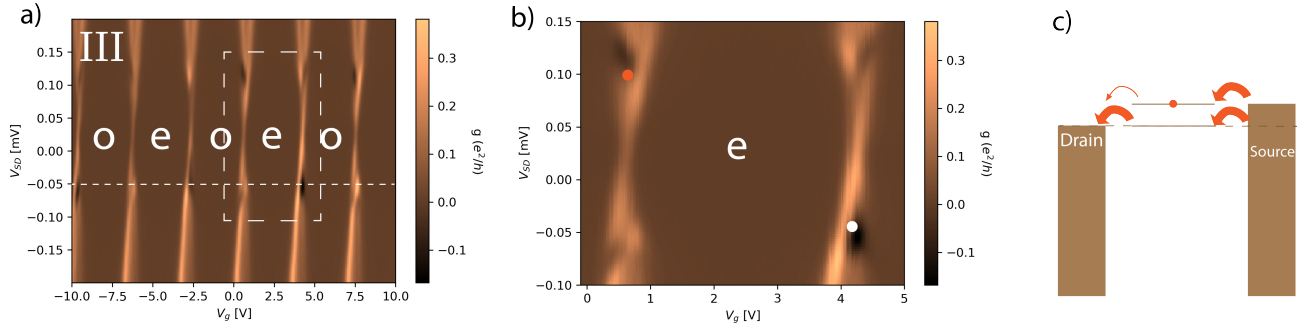


**Figure 6.13: NDC in bias spectrum.** a) is the differential conductance as a function of bias and gate potential for small bias potentials, measured for configuration III at  $T = 30\text{mK}$ . Even-odd parity oscillation is indicated as o: Odd, e: Even. The linecut is used in Fig. 6.16. b) is a zoom-in on the regions marked by the dashed square in a). c) is a schematic to illustrate what happens at the orange dot in b).

et al.<sup>39</sup> displayed in Fig. 6.3b), the NDC is found at the border of the odd-parity Coulomb diamonds. Zooming further in onto the square, indicated by orange in Fig. 6.13a), Fig. 6.13b) shows a close-up bias spectra of the transitions to NDC. Here the areas showing NDC is highlighted with an orange and a white dot. Furthermore, taking the shift,  $\sim 0.025\text{ mV}$  up in  $V_{SD}$ , into account, there is a decrease in conductance for the voltages that would be symmetric to the NDC around 0 bias. This suggests transport through bound states, resulting in slow particle escape. To explain the NDC, Fig. 6.13c) shows the potentials as they would be at the orange dot in Fig. 6.13b). Here the quasiparticle (orange dot) is transported through the level at the Fermi energy, with a high rate (indicated by the large arrows), until the bias is large enough to access the next level. Here the rate is low, and since the Island is Coulomb blocked, the presence of the quasiparticle in the top level blocks for transport through the first level. The upper level can be a subgap state or the continuum. Thus, the slow particle escape results in NDC as described in Eq. 6.11.

### 6.6.3 Modelling of parity oscillations

We now want to study the parity oscillations, that we first noticed in the linear conductance traces vs. gate potential of Fig. 6.10 and later saw in the bias spectra, highlighted in Fig. 6.13a). Taking inspiration from Higginbotham et al.,<sup>39</sup> we want to see if we can see the same features as they presented in this rather different setup. Additionally, we want to see if we can achieve a correlation with their model, that is sufficient enough for us to extract information such as superconducting gap,  $\Delta$ , the energy of the state that inhabit the quasiparticle causing NDC,  $E_0$ , and the lower bound to the quasiparticle poisoning time,  $\tau_p$ .

A zero-bias differential conductance trace in gate potential of configuration III (inset) is shown in Fig. 6.14a). Here the even-odd spacing differences is marked with "e" for even and "o" for odd. From this point, an increase in temperature is displayed in Fig. 6.14b). A feature here, is the broadening of the conductance peaks, but what is not as obvious is that the peaks move in gate voltage for increasing temperature. Thus, already around  $T \sim 0.25\text{ K}$  the even-odd alternation is gone. This is further emphasized in Fig. 6.14c) where the mean even and odd



distances are extracted and plotted as a function of temperature. This shows that at  $T \sim 0.18$  K the distances starts decreasing rapidly, whereafter it indeed saturates at an equal point at  $T \sim 0.25$  K. The insets display the illustrated energy parabolas as a function of normalized gate voltage similar the situation seen in Fig. 6.5d. At low temperature, only the processes without quasiparticle poisoning corresponding to Eq. 6.10 is applied for transport. As the temperature increase, the processes with quasiparticle poisoning seen in Eq. 6.11 starts to contribute, decreasing the spacing difference to a level beneath the experimental error. Applying the model from Higginbotham et al.,<sup>39</sup> following approximation for the differences in free energies used in finding the spacing difference,

$$F_o - F_e \approx -k_B T \ln \tanh \left( 2\rho_{Al} V_{Al} \Delta K_1 \left( \frac{\Delta}{k_B T} \right) + \ln \coth \left( \frac{E_0}{2k_B T} \right) \right) \quad (6.12)$$

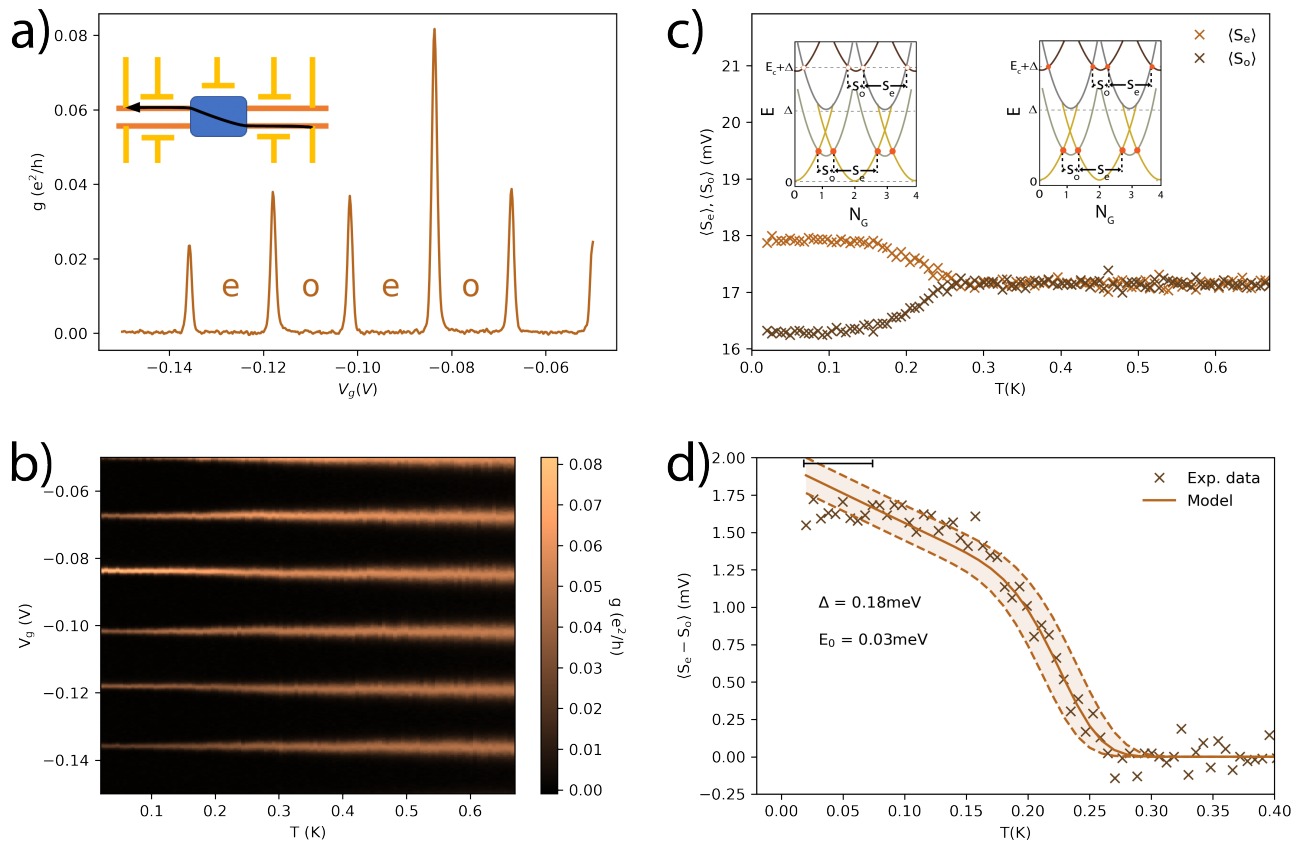


**Figure 6.14: Temperature dependence of a DNW island device.** **a** shows differential conductance as a function of gate potential at  $T = 20$  mK, even and odd parity is denoted in the Coulomb valleys. Inset: Shows the contact configuration, number III, used in this figure. **b** shows the evolution of the zero-bias traces as a function of temperature. **c** is the temperature dependency of the mean even and odd spacing of the Coulomb valleys. The insets display the illustrated transport processes (orange dots) for low (left) and high (right) temperature on the respective energy parabolas. **d** Even-odd Coulomb valley spacing difference as a function of temperature. The line are the model approximation used to simulate the data using  $\Delta$  and  $E_0$  as the model parameters. The parameter fit are made using `scipy.optimize.curve_fit`, which fits  $\Delta$  and  $E_0$ , using nonlinear least squares, as well as outputs the estimated covariance.<sup>21</sup> The dashed plots marks the error. The error bars, for the data points, based on the FWHM of the peaks are smaller than the experimental data points. The full data for **c** and **d** is shown in appendix Sec. C.2, where **d**) for configuration I and IV is displayed as well.

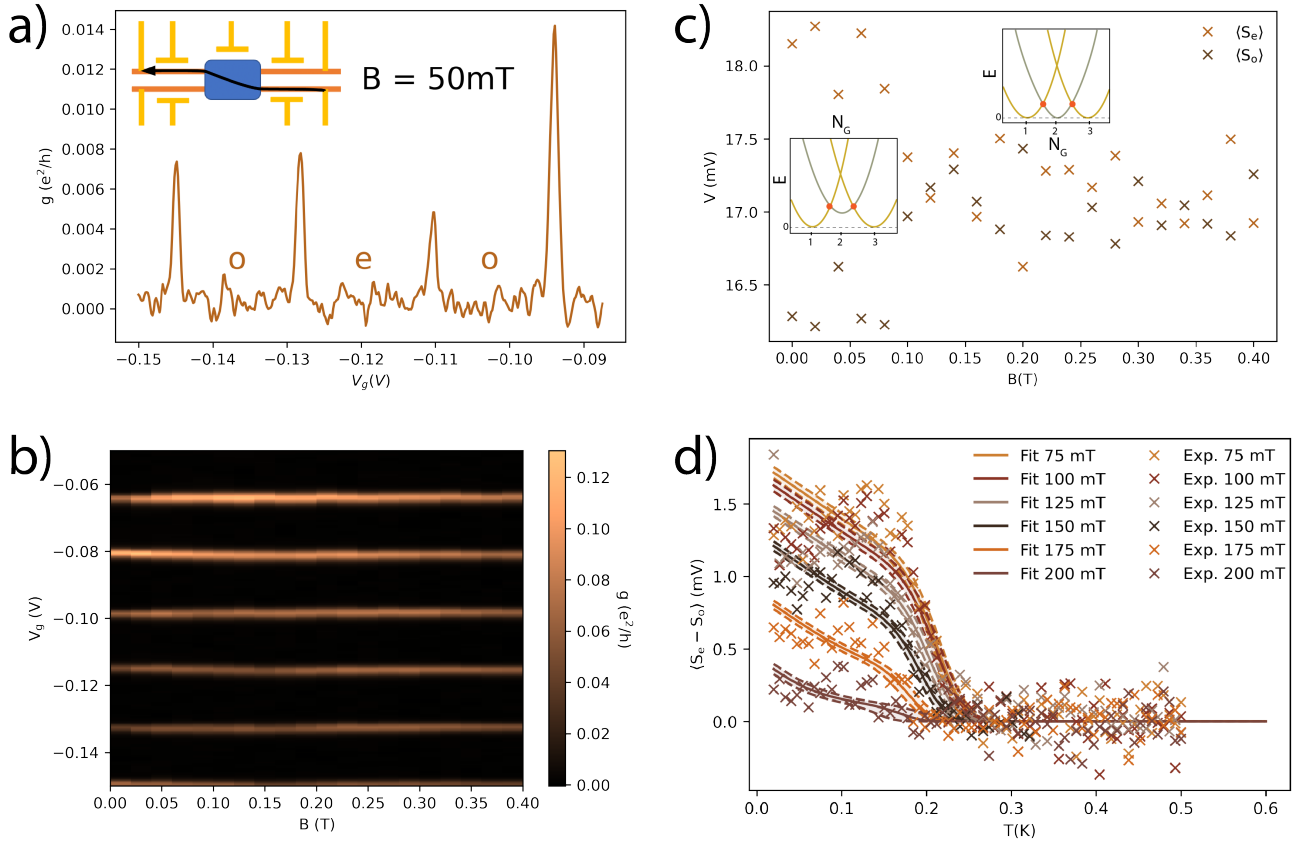


**Figure 6.15: Magnetic dependencies of an island device.** **a** shows differential conductance as a function of gate potential at  $T = 32$  mK and  $B = 50$  mT, even and odd parity is denoted in the Coulomb valleys. Inset: Shows the contact configuration, number III, used in this figure. **b** shows the evolution of the zero-bias traces as a function of magnetic field. **c** is the magnetic field dependency of the mean even and odd spacing of the Coulomb valleys. The insets display the transport processes (orange dots) for low (left) and high (right) magnetic field on the respective energy parabolas. **d** Even-odd Coulomb valley spacing difference as a function of temperatures at different magnetic fields. The parameter fit are made in the same way as in Fig. 6.14d), the dashed plots marks the errors.

proved quite excellent throughout the measured values. Here  $K_1(x)$  is a Bessel functions of the second kind. Figure 6.14d indeed displays this relative agreement between the approximation and the data using  $\rho_{Al} = 23$   $eV^{-1}nm^{-3}$ .  $V = 84.7 \cdot 10^4$   $nm^3$  is estimated from SEM images and the approximate thickness,  $l_{thickness} = 20nm - 3nm = 17nm$ , where the 3nm is an oxidized layer and the 20 nm where determined by the NW growers. Here, the data shows how the even-odd spacing starts out on the saturated level. Raising the temperature then, keeps the saturated level until 0.15K, whereafter it starts decreasing drastically. At around 0.26 K, the data shows that the even-odd spacing is reduced to be equal, hence the zero difference.

The approximation (Eq. 6.12) proved quite excellent at all relevant temperatures, as it follows the same path as the data going into the transition. Here it starts decreasing its slope. This results in the correct settlement of the model, around zero, corresponding to the data, for larger temperatures. One discrepancy between model and data however, is the increase in mean spacing difference as a function of decreasing temperature for low temperatures,  $T < 0.07K$ , as marked by the bar in the top of the plot. This seems to be an effect of the infinite rise

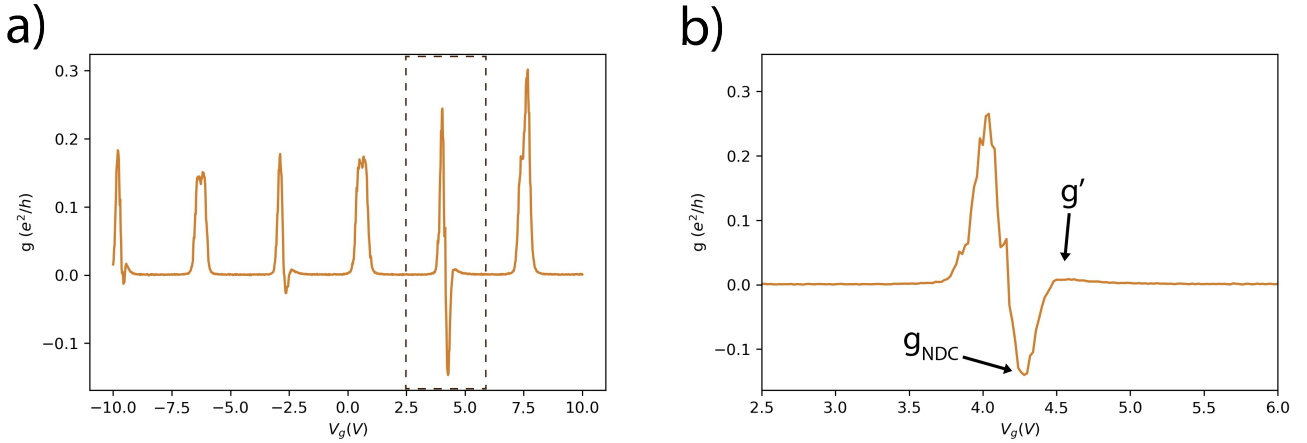


**Figure 6.16: Quasiparticle relaxation time estimation.** a) is the linecut at  $-0.05\text{mV}$  indicated in Fig. 6.13a). b) is a zoom-in on the dashed square seen in a) showing the  $g'$  and  $g_{\text{NDC}}$  peaks.

of the negative logarithmic functions as they approach zero. For the approximation in Eq. 6.12, this is, for the first term, caused by  $K_1(x)$  approaching zero as  $\Delta/(k_B T)$  increase with decreasing  $T$  as well as, for the second term, the logarithmic function approaching zero with  $\coth(E_0/2k_B T)$  approaching 1 with decreasing  $T$ .

From the model, different information about over system is granted. As displayed in Fig. 6.14, the superconducting gap,  $\Delta = 180 \mu\text{eV}$ , the energy of the state,  $E_0 = 30 \mu\text{eV}$  and the effective volume,  $V = 87.4 \times 10^4 \text{ nm}^3$  is extracted. Being capable to repeat the even-odd modelling of Higginbotham et al.<sup>39</sup> on this system, with the DNWs instead of a SNW, furthermore contributes to the understanding that this is indeed a superconducting island.

Now, investigating the magnetic field dependency of the peaks, Fig. 6.15a) displays four conductance peaks as a function of gate potential at magnetic field  $B = 50 \text{ mT}$ . Here the even-odd spacing is still visible. As in the former figure, Fig. 6.15b) shows the development of the zero-bias differential conductance peaks in  $V_g$ , however this time as a function of B-field. This is measured from zero to  $0.4 \text{ T}$ , because other studies of the same batch of DNWs yielded a critical magnetic field  $B_C \sim 0.4 \text{ T}$ . In this plot, the even-odd alternations starts out, at  $B = 0 \text{ T}$ , being relatively visible. At  $\sim 0.1 \text{ T}$  however, the alternations have faded out and the distance is equal for even and odd occupation. This being observable at magnetic field values below  $B_C$ , in addition to round rather than sharp shape of the transition from finite to zero even-odd spacing difference is noticeable. In fact, it looks similar to what Albrecht et al.<sup>3</sup> described as outward rather than inward bending displayed in the upper panel of Fig. 6.7. This is consistent with theoretical models of subgap states approaching the topological phase transition towards Majorana modes.<sup>18,67,75</sup>

The alternations however, begins to fade out quickly as the magnetic field strength is increased until  $B \sim 0.1 \text{ T}$  above which the spacing has evened out. Elaborating this tendency, Fig. 6.15c) shows the mean even and odd spacings respectively, as the magnetic field increases and, similar to the temperature dependency, leads to the converging of the spacings from  $B \sim 0.1 \text{ T}$ . In contrast to the data from Albrecht et al.<sup>2,3</sup> displayed in Fig. 6.6a-

e) and Fig. 6.7, we do not see any oscillations in even-odd peak spacing after the spacing approach zero. This could be due to the lower critical magnetic field of the DNW devices,  $\sim 0.4$  T, compared to the one they had,  $\sim 0.6$  T. As the magnetic field increase, these oscillating states would be approaching each other in energy, thus decreasing their spacing to a point below the experimental resolution. The insets shows the simple illustrated zero-temperature energy parabolas as a function of normalised gate voltage. At zero field and until the spacing converge, left inset, the odd-parity GS parabolas are slightly higher in energy compared to the even-parity GS ones, like the situation seen in the lower (red and black) parabolas of Fig. 6.5b). Here the yellow parabolas corresponds to the pure condensate state  $(N_{cp},0,0)$  and the green parabolas corresponds to  $(N_{cp},0,1)$ , thus the transport processes without quasiparticle poisoning corresponding to Eq. 6.10 as described by Albrecht et al.<sup>3</sup> However as they converge, right inset, the odd-parity GS parabolas have been lowered to 0 energy by the finite magnetic field effectively erasing the spacing difference. Applying the model from Higginbotham et al.<sup>39</sup> once again, Fig. 6.15d) provides information about the magnetic dependency of the mean spacing difference as a function of temperature. Here, similar curves to that of Fig. 6.14d) is show, but for various magnetic fields ranging from 75 mT to 200 mT. In this case, again we see the low temperature rise in the fits, but for higher temperatures than 0.1 K we can see the effect of the magnetic field strength enlarge. As the field increase, the spacing transition starts becoming more and more subtle, with decreasing starting-values and transition slopes. The fits here are generally well-describing the transition of the data as well as the convergence of spacings for larger temperatures. This magnetic field dependency of the spacing difference furthermore adds to the understanding that the achievement of having a superconducting island on the parallel DNW setup is accomplished.

#### 6.6.4 Information in the model

A feature that can be estimated from the model is the single quasiparticle relaxation time,  $\tau_{qp}$ . Figure 6.16 shows the linecut from Fig. 6.13a) where the NDC is visible. Zooming into these features, Fig. 6.16b) denotes the two relevant features,  $g'$  and  $g_{NDC}$ . From these values we can find the R-value as,  $R = (g' + g_{NDC}) / (g' - g_{NDC}) = -0.89$ . This can be roughly estimated quantitatively using fig. S2, that relates the R-value to the single quasiparticle relaxation time, from Higginbotham et al.<sup>39</sup> to give the lower bound  $\tau_{qp} > 0.1 \mu s$ . Here we assume the same parameters as Higginbotham et al.<sup>39</sup>

The model contains four important parameters:  $\rho_{AI}$ ,  $V_{AI}$ ,  $\Delta$ ,  $E_0$ .  $\rho_{AI}$  is the electron density of states in the island,  $V_{AI}$  the volume,  $\Delta$  the superconducting gap and  $E_0$ , the energy of the state inhabiting the quasiparticles causing NDC. All but  $\rho_{AI}$  is plotted below, as we found a realistic value for  $\rho_{AI}$ <sup>39,55</sup> and noted that the parameter affects the model in the same way that the  $V_{AI}$  does.

The model are plotted in Fig. 6.17 for a variation of one parameter value, keeping the two others constant.

While constant,  $V = 87.4 \times 10^4 \text{ nm}^3$ , which is our estimate of the DNW island device volume,  $E = 0.058 \text{ meV}$  corresponding to the value found by Higginbotham et al.<sup>39</sup> and  $\Delta = 0.18 \text{ meV}$ , corresponding to the extracted value from the model fitting at zero B-field, shown in Fig. 6.14d).

In Fig. 6.17a) the dependency of the superconducting gap,  $\Delta$ , is visualized. As  $\Delta$  increase the transition temperature, at what the spacing starts dropping rapidly, seems to increase with it, keeping the even-odd spacing difference for the lowest temperatures constant. The explanation for this is that as the superconducting gap increase, the quasiparticle states increase in energy with it. Another detail, that can be seen in the  $\Delta$  dependency, is that the spacing between the different  $\Delta$  plots increase with temperature, and thus the slope at the transition decrease with superconducting gap.

Looking at the dependence on the energy of the state,  $E_0$ , in Fig. 6.17b), the curves is displaced on the y-axis in contrast to the other two dependencies. Thus, adjusting  $E_0$ , the maximum spacing difference can be tuned. An interesting feature, in this dependency, is that the even-odd spacing difference all approach their zero-level at around 0.35-0.4 K. Thus, the overall tendency of the spacing difference is the same for all energies of the state, but greater in magnitude for larger ones. As the energy of the state increase, the quasiparticle production gets more energy demanding. This results in larger spacing, for low temperatures, since an even-odd cycle is effectively the addition of two quasiparticles. The difference in spacing is decreasing rapidly with increasing temperatures in the low-temperature range. The slope of this low-temperature spacing difference is very negative for large  $E_0$  values, but increase with decreasing  $E_0$ .

The explanation for this would be that for greater  $E_0$  values, a small increase in temperature would promote the likelihood of a few quasiparticles to appear, creating a drastic drop

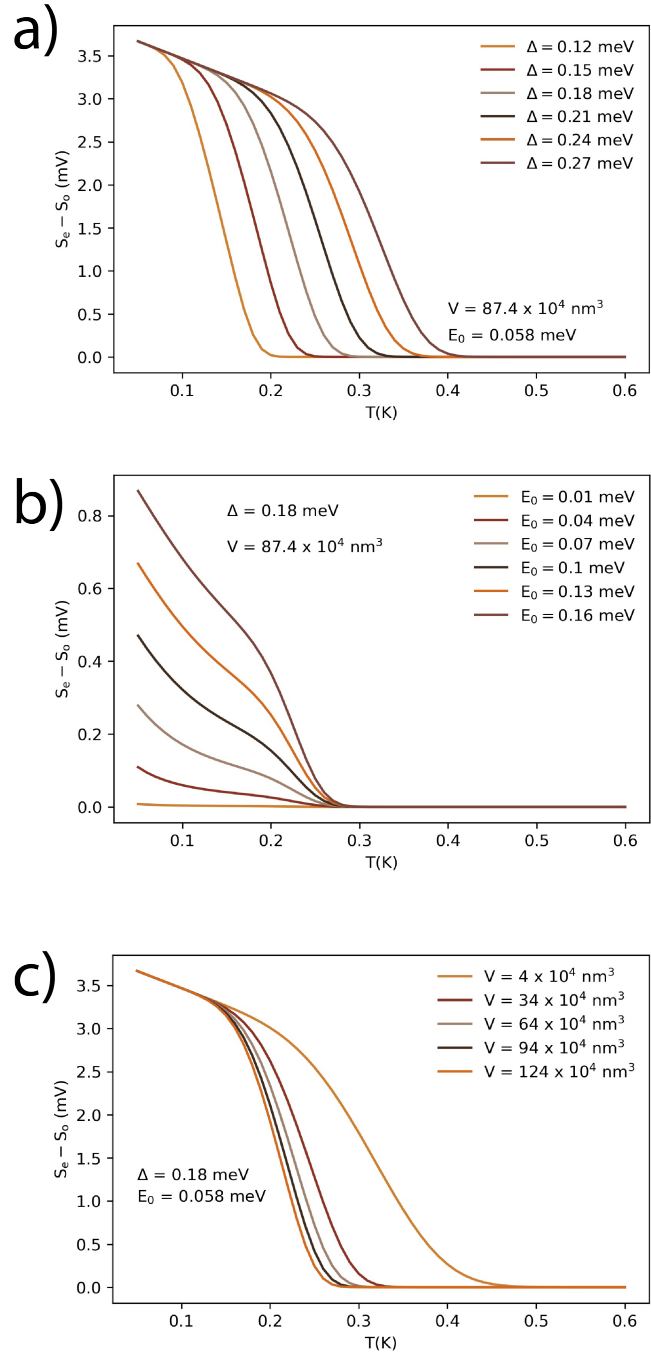


**Figure 6.17: Model dependencies of  $\Delta$ ,  $E_0$ , and  $V$ .** a)  $\Delta$ -dependency at constant  $V$  and  $E_0$ . b)  $E_0$ -dependency at constant  $V$  and  $\Delta$ . c)  $V$ -dependency at constant  $E_0$  and  $\Delta$

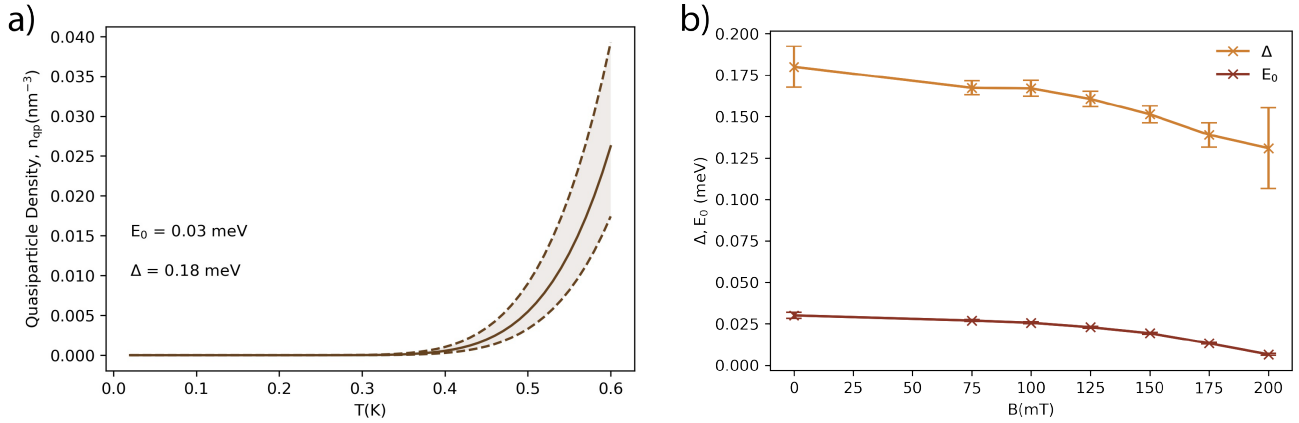


**Figure 6.18: Information from the model.** a) displays the quasiparticle excitation as a function of temperature. The dashed lines indicates the error. b) shows the parameter evolution as a function of B-field extracted from Fig. 6.15. The error arise from the fitting.

in the spacing difference. In the same situation for low  $E_0$  values, the promotion of quasiparticles is not as improbable to achieve and thus, the increase in temperature does not appear that big a relative change.

Further increasing the temperature now enters the transition where the number of quasiparticles stably increase until the even-odd spacing difference is not appearing anymore, hence the zero-difference range.

Moving on to the volume dependency in Fig. 6.17c), the tendency is very similar to that of the superconducting gap. One of the similarities, is that the shift in temperature, between the volume plots, increase with temperature. Thus, the larger the volume, the steeper the slope in the transition. This is explainable as the volume plays a role in the amount of quasiparticles that can be situated on the island. Thus, for smaller islands, the quasiparticle production requires larger thermal energy, and the transition from finite to zero even-odd spacing difference is then dragged out over a broader, and larger, spectrum of temperatures.

Using the model, the quasiparticle density,  $n_{qp}$ , as a function of temperature at zero magnetic field, as well as magnetic dependency of  $\Delta$  and  $E_0$  can be extracted as displayed in Fig. 6.18.

Figure 6.18a) is the quasiparticle density,  $n_{qp}$ , as a function of temperature, found by applying the variable values from the spacing vs. temperature fit in Fig. 6.14d) in Eq. 6.7. The plot reveals an exponential growth as a function of temperature at the temperatures we have measured. Comparing the plot with Fig. 6.14d) reveals that the drastic increase in quasiparticle density, does not have its onset before the spacing transition. At  $\sim 0.3$  K, when the spacing difference is  $\sim 0$ , the exponential growth of quasiparticle density seems to have its onset. Thus, it can be understood that only a very low amount of quasiparticle excitations causes the destruction of even-odd parity.

In Fig. 6.18b) the evolution of  $\Delta$  and  $E_0$  can be seen as a function of magnetic field, based on the values extracted from the fits in Fig. 6.15d). Both of them decrease with increasing field. For the superconducting gap, a decrease as a function of magnetic field is easily explainable as the magnetic field breaks down superconductivity, thus

Parameter	SNW	DNW
$V$ (nm <sup>3</sup> )	$7.4 \times 10^4$	$87.4 \times 10^4$
$\Delta(B=0)$ ( $\mu\text{eV}$ )	180	180
$E_0(B=0)$ ( $\mu\text{eV}$ )	58	30
$\tau_{\text{qp}}$ ( $\mu\text{s}$ )	$>0.1$	$>1$
$\tau_{\text{p}}$ (ms)	$>10$	$>1$

**Table 6.1: Comparison between DNW and SNW island devices.** This table compares the extracted values from the analysis above (DNW) and compares them to the list of the same values from Higginbotham et al.<sup>39</sup> (SNW).

closing the superconducting gap. For the energy of the state, the magnetic field could cause a Zeeman-splitting, separating the state into two by increasing one of the spin states in energy, while decreasing the other. In this case the transport would happen through the lower state, yielding a supposedly lower  $E_0$ .

To compare the DNW Island device investigated above, with the SNW island device fabricated by Higginbotham et al.<sup>39</sup> table 6.1 were set up. In the table, we can see that the volume of the DNW is larger than the one investigated by Higginbotham et al.<sup>39</sup> That we now know, will push the onset of the transition that destroys the even-odd parity to happen at lower temperatures. The  $\Delta$  of the DNW equals that of the SNW. Looking at  $E_0$  the DNW value is almost half the size of the SNW one, resulting in a substantially lower spacing difference before and during the transition. The lower bound on the quasiparticle relaxation time is the same value for both DNW and SNW measurements. This adds to the understanding that the systems are quite similar and can be compared fairly. Furthermore, setting  $T(\text{sat}) = 0.18\text{K}$  we can get an upper bound for the quasiparticle density  $n_{\text{qp}} < 1 \mu\text{m}^{-3}$  for small temperatures. This further yields  $n_{\text{qp}} V_{\text{AI}} < 10^{-3}$ . Then we can find the lower bound for the poisoning time of the bound state,  $\tau_{\text{p}} = \tau_{\text{qp}} / (n_{\text{qp}} V_{\text{AI}}) > 1$  ms. This is an order of magnitude smaller than that of the SNW, which makes sense as the larger volume would make the quasiparticle escape easier due to the increased capacitance.

### 6.6.5 The critical magnetic field

Following the even-odd analysis, we can further provide a proof of the rigidity of the superconducting island fabrication process.

In fact, for a whole other device, shown in Fig. 6.19a),

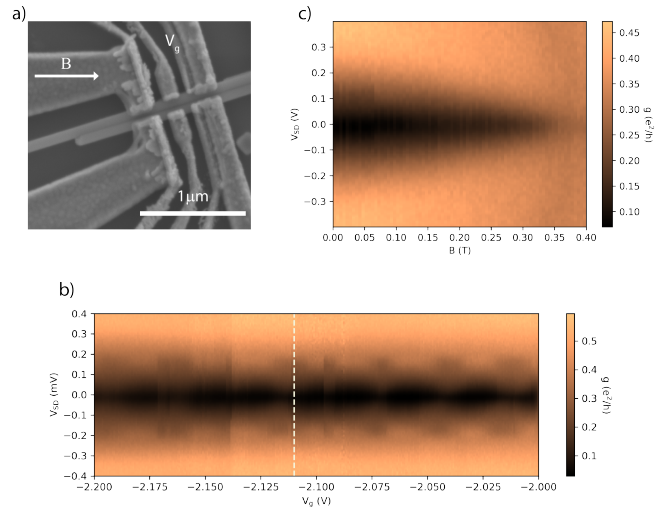


**Figure 6.19: Magnetic field induced closing of the superconducting gap.** a) Scanning electron micrograph, taken at  $V_{\text{Acc}} = 5\text{kV}$  of the measured device. A dielectric separates the top gates from the DNWs. b) Differential conductance as a function of gate,  $V_g$  and bias potential. The white line marks the gate potential where c) is measured. c) Differential conductance vs. bias potential and magnetic field, yielding a critical magnetic field,  $B_C = 0.4\text{T}$ . Measured at  $T = 30\text{mK}$ .

---

with the only similarity of having been made from the same batch of NW growth, we see the closing of the superconducting gap as a function of magnetic field. The measurement is done at the gate potential displayed as the white dashed line in Fig. 6.19b). The closing of the gap is visualized in Fig. 6.19c), showing differential conductance as a function of B-field,  $B$ , and bias potential,  $V_{SD}$ . from where we can extract the critical field of the island devices to be  $\sim 0.4$  T. Furthermore, we can with this critical field measurement add to understanding that the fabrication of the DNW island devices has been accomplished.

## 6.7 Conclusion on DNW Islands

In conclusion we have managed to fabricate the first ever Coulomb blockaded superconducting island device on double nanowires. Furthermore we have shown that we could measure even-odd parity electron filling of the Al island that have been fabricated onto the two parallel DNWs, using four different two-terminal configurations. This difference verifies, due to Cooper pairing of superconductors, that the island is indeed superconducting.

In addition, we have succeeded in a modelling of our DNW island device, based on the work of Higginbotham et al.,<sup>39</sup> yielding a superconducting gap,  $\Delta = 180 \mu\text{eV}$ , an energy of the state giving rise to quasiparticle excitation,  $E_0 = 30 \mu\text{eV}$ , and a lower bound to the poisoning time in this bound state,  $\tau_p > 0.1\text{ms}$ .

Furthermore, on another device we have seen a closing pattern of the gap yielding a critical magnetic field at  $\sim 0.4$  T. The critical magnetic field is another sign of superconductivity, further cementing the fact that we have succeeded in fabricating superconducting islands on DNW systems. As this is one of the major steps towards the observation of the topological Kondo effect, this is of substantial interest for the scientific field of Majorana states.

To continue on the journey of observing the topological Kondo effect, three more steps should be optimized. First, the interlead couplings, here denoted as  $\Gamma_{\text{left, right}}$  should be minimized, as these add to the uncertainty of the charge carrier paths during transport measurements. In terms of measurement, the achievement of this would be validated by the detection of a lower base conductance at the zero-bias traces for configurations analogue to configuration V and VI. This could be optimized by the selection of DNWs with higher spacing/dot count ratio, which can be challenging as a too high rate produces SNWs instead of DNWs. Some sort of insulating capping layer around the DNWs applied after the Al, could add to this. Second, the spin-orbit coupling of the DNWs should be optimized, for a higher probability of opening of the topological gap in the proximitized semiconductors. This could for instance be done, using growth of hybrid epitaxial InAsSb/Al nanowires as described by Sestoft et al.<sup>72</sup> Third, the critical magnetic field should be as large as possible to make space in B-field for the induced superconducting gap to close and re-open in the topological regime. This could be done by using alternative superconductors as NbTiN,<sup>87</sup> Sn,<sup>65</sup> or Pb,<sup>43</sup> instead of Al. Another way to increase the critical magnetic field would be to decrease the Al shell thickness of the DNWs. This could potentially be stabilized by



---

the insulating capping layer, as proposed for the increased DNW spacing/dot count ratio.

---

## 7 Conclusion and outlook

The work presented in this thesis gains information on the DNW hybrid structures, that throughout the last decade has been proposed as a platform for miscellaneous experiments. The fabrication of DNW Superconducting Island devices and Little-Parks tunnel probes are described, the first-mentioned type of device and DNW Josephson Junctions are analysed.

Different parameters affects the successful fabrication of a double nanowire device. One of these is the nanowires spacing/dot count ratio. This effectively defines the surface to surface distance between the NWs. Is this distance small, the coupling between the NWs is large and the device acts like a large SNW device. In contrast if the distance is large, the DNWs is likely to break apart. Thus, an understanding of this ratio is important for future investigations.

In the DNW Josephson Junctions, supercurrent is detected in each NW, at  $T = 30\text{mK}$  and magnetic field,  $B = 0$ , and signatures of multiple Andreev reflections yield a superconducting gap,  $\Delta = 150_{-50}^{+30}\mu\text{eV}$ .

Regarding the DNW Island device, we have presented the first ever Coulomb blockaded superconducting island device based on double nanowires. It showed even-odd electron parity on the island when measured at temperature,  $T = 30\text{mK}$ , and magnetic field,  $B = 0$ . This even-odd parity breaks down with magnetic field and temperature, due to quasiparticle excitation. This we managed to model, using the model presented by Higginbotham et al.,<sup>39</sup> allowing us to extract a rough estimate of the superconducting gap,  $\Delta = 180\mu\text{eV}$ , an energy of the state giving rise to the quasiparticle excitations,  $E_0$ , and a lower bound to the poisoning time,  $\tau_p > 1\text{ms}$ .

The results seen in the DNW Josephson Junction are extremely interesting, as it indicates the ability of the *in-situ* grown hybrid DNWs to favor the separation of Cooper pairs, one electron in each NW, due to the electron-electron interactions. This could be applied for qubit state teleportation. To learn more about the distances of such Cooper pair splitting, an experiment is proposed where DNWs, that branches out in a Y-geometry in one end, is used to increase the distance between superconductor and contact on the NWs. By increasing this distance, the interwire distance increase as well. Thus by detecting the Cooper pair splitting efficiency related to each set of contacts, the maximum distance between the entangled electrons in the Cooper pair can be estimated, by observing when it drops.

Likewise, the results found in the DNW island device are exciting, since the superconducting Island provide a foundation for topological Kondo effect experiments. These are interesting as they provide a smoking gun signature of the non-local quantum dynamics of Majorana zero modes. In order to optimize the DNW island device structures for further experiments, increased DNW spacing/dot count ratio were proposed potentially stabilized by an insulating capping layer to avoid separation into SNWs. Furthermore, increased spin-orbit coupling could be achieved by the use of InAsSb DNWs instead of InAs. Finally, NbTiN, Sn or Pb superconductors were proposed as an alternative to Al, in order to increase the critical magnetic field. This could also

---

be altered by decreasing the thickness of the superconducting layer, which could potentially be stabilized by the before-mentioned insulating capping layer as well.

---

## Appendices

### A Fabrication

#### A.1 Recipes

To fabricate a batch of devices, the steps in Sec. A.2 is applied in an order dependent of the devices For Sample 1 as denoted in Table 4.1, the order, starting from a blank 5x5mm substrate was:

1. Removal of non-exposed resist (AZ1515)
2. Deposition of Qdev898 DNWs as described in Sec. 4.3
3. EL9 resist application.
4. Electron beam exposure for the etching pattern (60000 dot number / 600 field size).
5. Pattern development for EL9 resist
6. Aluminum etching for 9 s in transene D.
7. A6 resist application.
8. Electron beam exposure for the gate and contact deposition (60000 dot number / 600 field size).
9. Pattern development for A6 resist
10. Metal deposition of 5 nm Ti and 200 nm Au. For contacts on InAs and gate deposition (before June 2021)
11. Fast lift-off
12. A6 resist application.
13. Electron beam exposure for the lead (connections to outer leads) deposition (60000 dot number / 600 field size).
14. Pattern development for A6 resist
15. Metal deposition of 5 nm Ti and 270 nm Au. (before June 2021)
16. Fast lift-off

For Sample 2 as denoted in Table 4.1, the order, starting from a blank 5x5mm substrate was:

1. Removal of non-exposed resist (AZ1515)

- 
2. Deposition of Qdev898 DNWs as described in Sec. 4.3
  3. EL9 resist application.
  4. Electron beam exposure for the etching pattern (60000 dot number / 600 field size).
  5. Pattern development for EL9 resist
  6. Aluminum etching
  7. A6 resist application.
  8. Electron beam exposure for the Al contact deposition (60000 dot number / 600 field size).
  9. Pattern development for A6 resist
  10. Metal deposition of 5 nm Ti and 220 nm Au.
  11. Fast lift-off
  12. Discarded due to large pattern offset.

For Sample 3 as denoted in Table 4.1, the order, starting from a blank 5x5mm substrate was:

1. Removal of non-exposed resist (AZ1515)
2. Deposition of Qdev898 DNWs as described in Sec. 4.3
3. Discarded due to large SNW yield. Better suited for other fabrications.

For Sample 4 as denoted in Table 4.1, the order, starting from a blank 5x5mm substrate was:

1. Removal of non-exposed resist (AZ1515)
2. Deposition of Qdev898 DNWs as described in Sec. 4.3
3. EL9 resist application.
4. Electron beam exposure for the etching pattern (60000 dot number / 600 field size).
5. Pattern development for EL9 resist
6. Aluminum etching
7. A6 resist application.
8. Electron beam exposure for the Al contact deposition (60000 dot number / 600 field size).

- 
9. Pattern development for A6 resist
  10. Metal deposition of 5 nm Ti and 200 nm Au on Al.
  11. Overnight liftoff
  12. A6 resist application.
  13. Electron beam exposure for contacts on InAs and gate deposition (60000 dot number / 600 field size).
  14. Pattern development for A6 resist
  15. Metal deposition of 5 nm Ti and 220 nm Au. For contacts on InAs and gate deposition (before June 2021)
  16. Overnight liftoff
  17. A6 resist application.
  18. Electron beam exposure for the lead (connections to outer leads) deposition (60000 dot number / 600 field size).
  19. Pattern development for A6 resist
  20. Metal deposition of 5 nm Ti and 300 nm Au. (before June 2021)
  21. Fast lift-off
  22. A6 resist application.
  23. Electron beam exposure for the lead (connections to outer leads) repairs (60000 dot number / 600 field size).
  24. Pattern development for A6 resist
  25. Metal deposition of 5 nm Ti and 200 nm Au. (before June 2021) Angled (+3° for the first half, -3° for the second half)
  26. Fast lift-off

For Sample 5 as denoted in Table 4.1, the order, starting from a blank 5x5mm substrate was:

1. Removal of non-exposed resist (AZ1515).
2. Deposition of Qdev905 SNWs as described in Sec. 4.3.
3. A6 resist application.

- 
4. Electron beam exposure for the gate and contact deposition connected to the outer leads (60000 dot number / 600 field size).
  5. Removal of non-exposed A6 resist.
  6. A6 resist application.
  7. Electron beam exposure for the gate and contact deposition (60000 dot number / 600 field size).
  8. Removal of non-exposed A6 resist.
  9. Discarded due to alignment issues.

For Sample 6 as denoted in Table 4.1, the order, starting from a blank 5x5mm substrate was:

1. Removal of non-exposed resist (AZ1515).
2. Deposition of Qdev905 SNWs as described in Sec. 4.3.
3. A6 resist application.
4. Electron beam exposure for the gate and contact deposition connected to the outer leads (60000 dot number / 600 field size).
5. Pattern development for A6 resist
6. Metal deposition of 5 nm Ti and 200 nm Au. For contacts on InAs and gate deposition (before June 2021)
7. Fast lift-off

For Sample 7 as denoted in Table 4.1, the order, starting from a blank 5x5mm substrate was:

1. Removal of non-exposed resist (AZ1515).
2. Deposition of Qdev905 SNWs as described in Sec. 4.3.
3. A6 resist application.
4. Electron beam exposure for the gate and contact deposition connected to the outer leads (60000 dot number / 600 field size).
5. Pattern development for A6 resist
6. Metal deposition of 5 nm Ti and 200 nm Au. For contacts on InAs and gate deposition (before June 2021)
7. Fast lift-off

---

Sample 8, 9 and 10 were fabricated by A. Vekris, who did not follow the exact same steps as I did. It is noted when something different from the steps I used used was taking place. For sample 8, as denoted in Table 4.1, starting from a blank 5x5mm substrate:

1. Removal of non-exposed resist (AZ1515) by dipping it in NMP for 7 minutes.
2. Deposition of Qdev939 DNWs as described in Sec. 4.3.
3. EL9 resist application.
4. Electron beam exposure for the Al etching (60000 dot number / 300 field size).
5. Pattern development for EL9 resist.
6. Al etching for 9 s.
7. A6 resist application.
8. Electron beam exposure for the gate and contact deposition (240000 dot number / 600 field size). Area dose:  $1000 \mu\text{C}/\text{cm}^2$ .
9. Pattern development for A6 resist.
10. Metal deposition of 5 nm Ti and 205 nm Au. For contacts on Al and gate deposition.
11. Fast lift-off.
12. A6 resist application.
13. Electron beam exposure for the lead (connections to outer leads) deposition (60000 dot number / 300 field size). Area dose:  $1000 \mu\text{C}/\text{cm}^2$ .
14. Pattern development for A6 resist.
15. Metal deposition of 5 nm Ti and 250 nm Au.
16. Fast lift-off.

For Sample 9, as denoted in Table 4.1, starting from a blank 5x5mm substrate:

1. Removal of non-exposed resist (AZ1515) by dipping it in NMP for 7 minutes.
2. Deposition of Qdev939 DNWs as described in Sec. 4.3.
3. EL9 resist application.



- 
4. Electron beam exposure for the Al etching (60000 dot number / 300 field size).
  5. Pattern development for EL9 resist.
  6. Al etching for 9 s.
  7. A6 resist application.
  8. Electron beam exposure for the gate and contact deposition (240000 dot number / 600 field size). Area dose:  $1000 \mu\text{C}/\text{cm}^2$ .
  9. Pattern development for A6 resist.
  10. Metal deposition of 5 nm Ti and 205 nm Au. For contacts on InAs and gate deposition (before June 2021)
  11. Fast lift-off (1h 15min in NMP)
  12. A6 resist application.
  13. Electron beam exposure for the lead (connections to outer leads) deposition (60000 dot number / 300 field size). Area dose:  $1000 \mu\text{C}/\text{cm}^2$ .
  14. Pattern development for A6 resist.
  15. Removal of non-exposed A6 resist,
  16. A6 resist application.
  17. Electron beam exposure for the lead (connections to outer leads) deposition (60000 dot number / 600 field size). Area dose:  $1000 \mu\text{C}/\text{cm}^2$ .
  18. Pattern development for A6 resist.
  19. Metal deposition of 5 nm Ti and 250 nm Au.
  20. Fast lift-off (2.5h in NMP)
  21. A6 resist application.
  22. Electron beam exposure for repairs (connections to outer leads) deposition (60000 dot number / 600 field size). Area dose:  $1000 \mu\text{C}/\text{cm}^2$ .
  23. Pattern development for A6 resist.
  24. Metal deposition of 5 nm Ti and 300 nm Au.

---

25. Fast lift-off (1.5h in NMP)

For Sample 10, as denoted in Table 4.1, starting from a blank 5x5mm substrate:

1. Removal of non-exposed resist (AZ1515) by dipping it in NMP for 7 minutes.
2. Deposition of Qdev939 DNWs as described in Sec. 4.3.
3. EL9 resist application.
4. Electron beam exposure for the Al etching (60000 dot number / 300 field size).
5. Pattern development for EL9 resist.
6. Al etching for 9 s.
7. Fast lift-off
8. A6 resist application.
9. Electron beam exposure for the gate and contact deposition (240000 dot number / 600 field size). Area dose:  $1000 \mu\text{C}/\text{cm}^2$ .
10. Pattern development for A6 resist.
11. Metal deposition of 5 nm Ti and 205 nm Au. For contacts on InAs and gate deposition (after June 2021)
12. Fast lift-off (1h 15min in NMP)
13. A6 resist application.
14. Electron beam exposure for the lead (connections to outer leads) deposition (60000 dot number / 600 field size). Area dose:  $1000 \mu\text{C}/\text{cm}^2$ .
15. Pattern development for A6 resist.
16. Metal deposition of 5 nm Ti and 250 nm Au for leads.
17. Fast lift-off (2h in NMP)
18. A6 resist application.
19. Electron beam exposure for repairs (connections to outer leads) deposition (60000 dot number / 600 field size). Area dose:  $1000 \mu\text{C}/\text{cm}^2$ .
20. Pattern development for A6 resist for less critical depositions.

- 
21. Metal deposition of 5 nm Ti and 300 nm Au for leads.
  22. Fast lift-off (1.5h in NMP)
  23. Spin A2 at 4000rpm 45 s
  24. Bake 2 minutes at 115 °C
  25. Spin A2 at 4000rpm 45 s
  26. Bake 2 minutes at 115 °C
  27. Electron beam exposure for ALD windows (20000 dot number / 300 field size). Area dose: 8000  $\mu\text{C}/\text{cm}^2$ .  
Beam current = 2nA
  28. Development as for A6 but 60s in MIBK:IPA 1:3, 2 min ashing
  29. ALD 60 cycles, 10 h prebake at 90 degrees ( HfO<sub>2</sub>: pulsetime 0.2, H<sub>2</sub>O; 0.02) (takes 4hours +X hours prebake)
  30. Fast lift-off (2h 45 min, important: sample upside down)
  31. Ashed for 2 min
  32. A6 resist application
  33. Electron beam exposure for the gate and contact deposition (240000 dot number / 600 field size). Area dose: 1000  $\mu\text{C}/\text{cm}^2$ .
  34. Pattern development for A6 resist (ash for 45 s)
  35. Removal of A6 resist.
  36. A6 resist application
  37. Electron beam exposure for the gate and contact deposition (240000 dot number / 600 field size). Area dose: 1000  $\mu\text{C}/\text{cm}^2$ .
  38. Pattern development for A6 resist (ash for 45 s)
  39. Metal deposition of 5 nm Ti and 180 nm Au for topgates.
  40. Fast lift-off (1h in NMP)

---

## A.2 Fabrication steps

### Removal of non-exposed resist

If the resist is EL9 or A6:

1. Immerse for 2 min in Dioxylene.
2. Immerse for 2 min in Acetone.
3. Immerse for 1 min in IPA.
4. N<sub>2</sub> blowdry.

If the resist is on a blank substrate (AZ1505 resist):

1. Set a bath to 60 deg.
2. Immerse the blank substrate in the heated NMP for 7 min.
3. Immerse the substrate in room temperature IPA for 1 minute.
4. N<sub>2</sub> blowdry.
5. Ash for 2 min.

### Resist application

If the resist are later applied for selective etching:

1. Ash in oxygen plasma for 1 min.
2. Spin 1 drop EL9 at 4000 rpm for 45 s, using a NW low acceleration program.
3. Bake at 185°C for 2 minutes.

If the resist are later applied for metal deposition:

1. Ash in oxygen plasma for 1 min.
2. Spin 1 drop A6 at 4000 rpm for 45 s, using a NW low acceleration program.
3. Bake at 185°C for 4 minutes.

### Electron beam Exposure:

From the smallest distance of the intended pattern,  $d_{\min}$ , find the resolution,  $D_{\text{res}}$  needed as  $D_{\text{res}} = d_{\min}/10$ .

From  $D_{\text{res}}$  determine the field size,  $d_{\text{field}}$  and pixel number,  $n_{\text{pixel}}$  as,  $D_{\text{res}} = d_{\text{field}}/n_{\text{pixel}}$ . Use dose: 400  $\mu\text{C}/\text{cm}^2$ ,

---

Beam Current = 500pA and Objective lens aperture (OLAP) = 40  $\mu\text{m}$ .

### **Pattern development**

For EL9 resist:

1. Immerse for 40 s in MIBK:IPA 1:3.
2. N<sub>2</sub> blowdry.
3. Ash in oxygen plasma 1 min.
4. Post bake 120°C for 60 s.

For A6 resist used for gate, contact or similar critical deposition:

1. Immerse for 30 s in MIBK:IPA 1:3.
2. Immerse for 30 s in IPA 1:3.
3. N<sub>2</sub> blowdry.
4. Ash in oxygen plasma 30 s.

For A6 resist used for lead or other less critical deposition:

1. Immerse for 30 s in MIBK:IPA 1:3 (+15 s per extra A6 layer, spinned on top of the first layer).
2. Immerse for 30 s in IPA.
3. N<sub>2</sub> blowdry.
4. Ash in oxygen plasma 60 s.

### **Aluminum etching**

1. Set a bath at 55 degrees.
2. Prepare two beakers of equal volume of transene D and MQ water respectively.
3. Place the two beakers in the bath and put lid on them.
4. Prepare a third beaker of MQ at room temperatur.
5. Measured the temperature on the bottom of the MQ beaker.
6. At 50 degrees C, dip the sample in the transene D for 8.5 seconds.
7. MQ rinse for 30 sec on 50 C bath.

---

8. MQ rinse for 30 sec on room temperature beaker.

9. N<sub>2</sub> blowdry.

### **Metal deposition**

For all contacts and gates on InAs fabricated before June 2021:

1. Milling process using 7 W for 7 min w. Ar flow (RFetch7watts7min).
2. Deposition of Ti.
3. Deposition of Au.

For all contacts on InAs and gates fabricated after June 2021:

1. Milling process using 15 W for 8 min. w. Ar flow (ShivRFetch).
2. Deposition of Ti.
3. Deposition of Au.

For all contacts on Al:

1. Milling process using 25 W for 9 min. w. Ar flow (ShivRFetch).
2. Deposition of Ti.
3. Deposition of Au.

For leads connecting the contacts on the devices to the outer leads:

1. Deposition of Ti.
2. Deposition of Au.

### **Lift-off**

For fast (~2h) liftoff:

1. Heat a beaker with NMP in a bath set to 80 deg.
2. Leave the blank substrate in the heated NMP for 1.5h.
3. Blow the metal thin film away with air in a pipette.
4. Immerse the substrate in room temperatur Acetone for minimum 1 minute. Using the pipette to create flow around the devices, enhances the chances of removing all excess metal.

5. Immerse the substrate in room temperature IPA for minimum 1 minute. Using the pipette to create flow around the devices, enhances the chances of removing all excess metal.

6. N<sub>2</sub> blowdry.

For over-night liftoff:

1. Leave the blank substrate in Room temperature NMP overnight.

2. Blow the metal thin film away with air in a pipette.

3. Immerse the substrate in room temperature Acetone for minimum 1 minute. Using the pipette to create flow around the devices, enhances the chances of removing all excess metal.

4. Immerse the substrate in room temperature IPA for minimum 1 minute. Using the pipette to create flow around the devices, enhances the chances of removing all excess metal.

5. N<sub>2</sub> blowdry.

### A.3 Ready Devices

Figure A.3, displays the devices on Sample 4, that are ready for measurement.

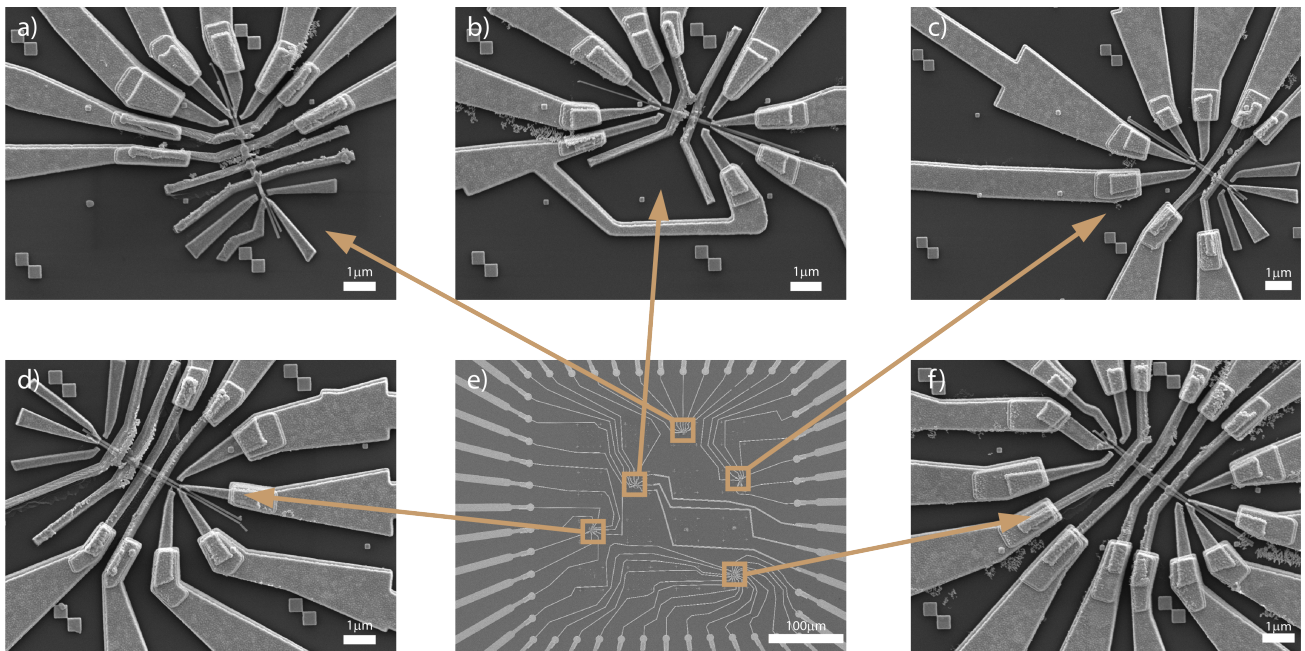


**Figure A.1: Overview of the devices ready for measurement.** This figure displays the devices located on Sample 4, as denoted in Table 4.1. e) Displays a SEM overview of the sample area, corresponding to Fig. 4.7. From here arrows are pointed out from different locations to the respective zoom-in on the devices located on the Sample.

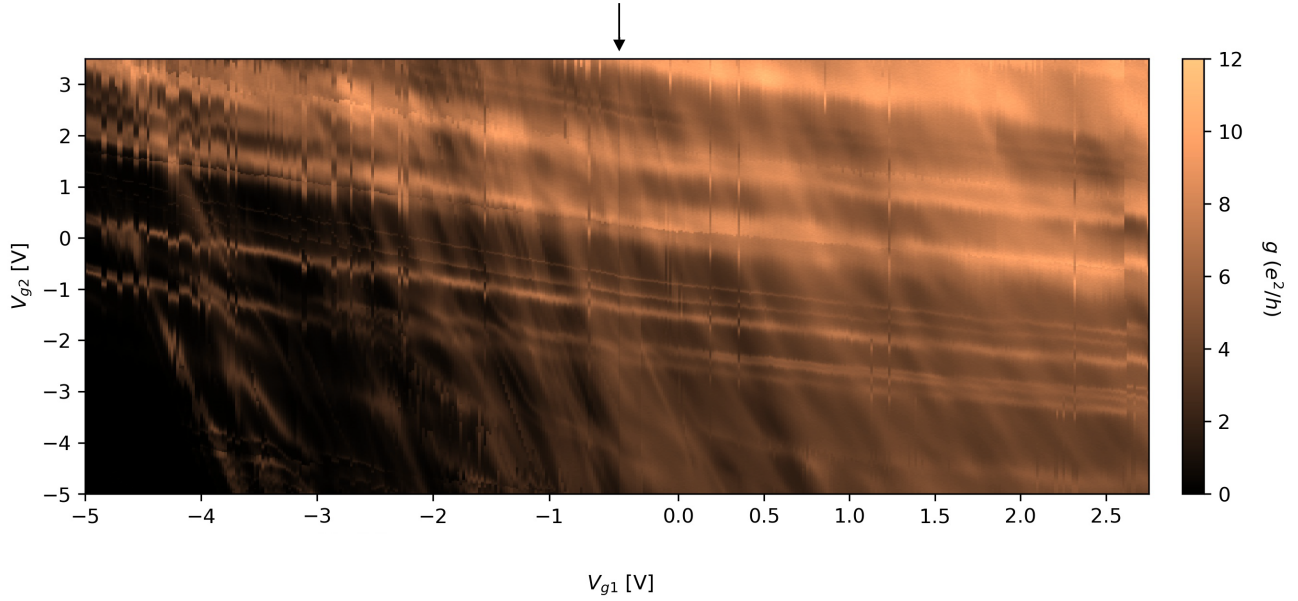


**Figure B.2: Gate sweep of the JJ device.** Differential conductance as a function of  $V_{g1}$  and  $V_{g2}$ . This is two sweeps merged together, where the arrow indicates. Be aware that the  $V_{g1}$  axis differs slightly on either side of the merge.

## B Additional data on DNW Josephson Junctions

### B.1 Gatesweep of the Josephson junction

In Fig. B.2 a gate sweep, used to get an overview over the features of the JJ device, is displayed. The area discussed in Sec. 5.4 is just located just beside (in positive  $V_{g1}$ ) direction.

### B.2 Additional linecuts in 2-terminal voltage bias

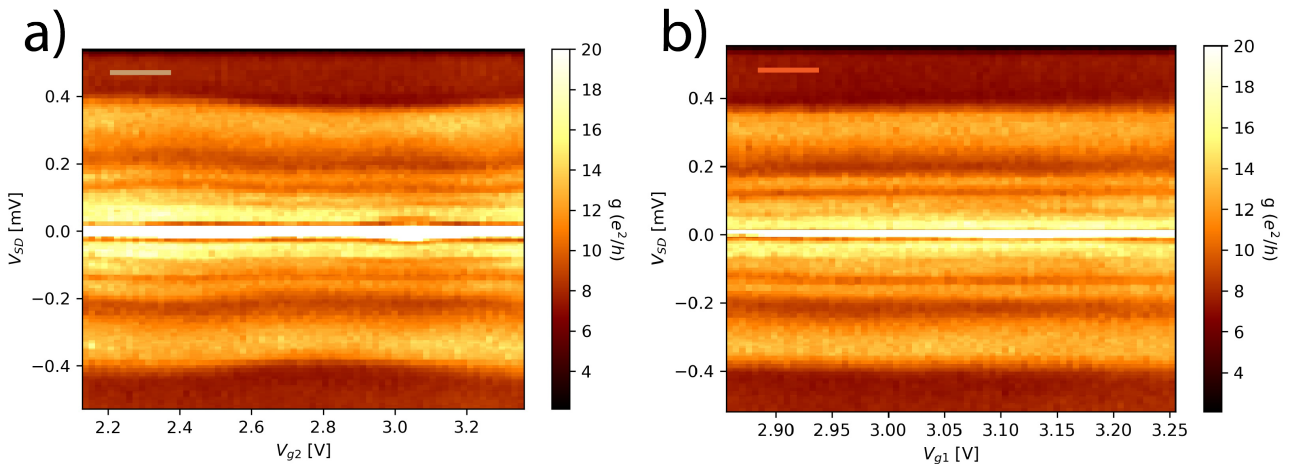


**Figure B.3: Gate sweep of the JJ device.** differential conductance,  $g$ , as a function of bias potential,  $V_{SD}$ , and gate potentials,  $V_{g2}$  for a) and  $V_{g1}$  for b). They are corresponding to the brown, a), and orange, b), arrows in Fig. 5.6a)

In Fig. B.3 two additional bias spectra from Sec. 5.4 is displayed, corresponding to the brown, a), and orange, b), arrows in Fig. 5.6a), they are discussed in the main text, indicating supercurrent and multiple Andreev



reflections.

### B.3 Additional 4-terminal current bias spectra

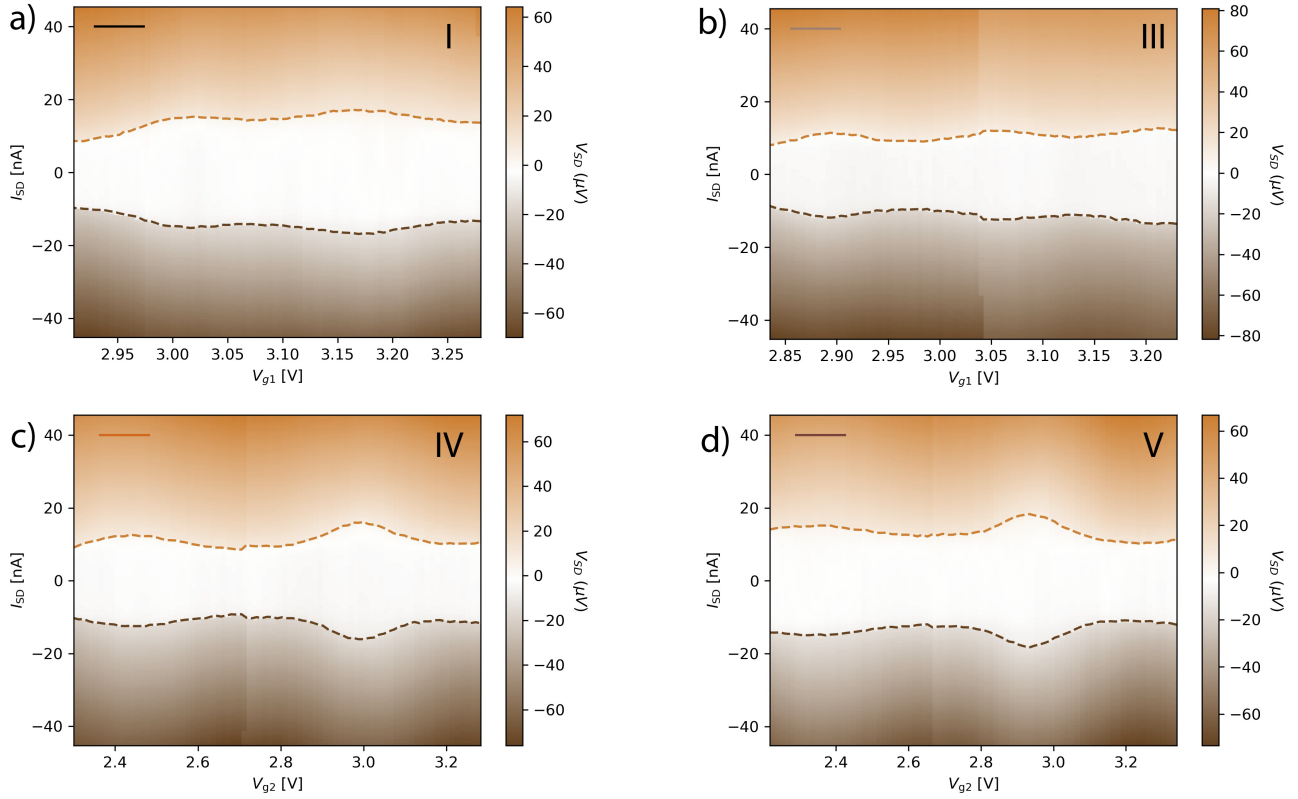











**Figure B.4: Current bias spectra.** Voltage as a function of current bias,  $I_{SD}$  and gate potential,  $V_{g1}$  a) and b) and  $V_{g2}$  c) and d). They correspond to the arrows depicted in Fig. 5.7a).

In Fig. B.4 four additional current bias spectra from Sec. 5.4 is displayed, corresponding to the arrows, I, III, IV and V in Fig. 5.7a), they are discussed in the main text, showing supercurrent.

### B.4 Josephson junctions publication

Below, the publication, from Vekris et al.<sup>85</sup> that I have contributed to during this thesis, is presented.

Josephson junctions in double nanowires bridged by *in-situ* deposited superconductors

Alexandros Vekris <sup>1,2</sup> Juan Carlos Estrada Saldaña <sup>1</sup> Thomas Kanne <sup>1</sup> Mikelis Marnauza <sup>1</sup> Dags Olsteins,<sup>1</sup>  
Furong Fan <sup>3</sup> Xiaobo Li,<sup>3</sup> Thor Hvid-Olsen <sup>1</sup> Xiaohui Qiu,<sup>4,5</sup> Hongqi Xu <sup>3,6</sup> Jesper Nygård <sup>1</sup>  
and Kasper Grove-Rasmussen <sup>1,\*</sup>

<sup>1</sup>Center For Quantum Devices, Niels Bohr Institute, University of Copenhagen, 2100 Copenhagen, Denmark


<sup>2</sup>Sino-Danish Center for Education and Research (SDC) SDC Building, Yanqihu Campus, University of Chinese Academy of Sciences, 380 Huaibeizhuang, Huairou District, 101408 Beijing, China

<sup>3</sup>Beijing Key Laboratory of Quantum Devices, Key Laboratory for the Physics and Chemistry of Nanodevices and Department of Electronics, Peking University, Beijing 100871, China

<sup>4</sup>CAS Key Laboratory of Standardization and Measurement for Nanotechnology, National Center for Nanoscience and Technology, Beijing 100190, China

<sup>5</sup>CAS Center for Excellence in Nanoscience, National Center for Nanoscience and Technology, Beijing 100190, China

<sup>6</sup>Beijing Academy of Quantum Information Sciences, 100193 Beijing, China

 (Received 5 May 2021; revised 23 July 2021; accepted 10 August 2021; published 10 September 2021)

We characterize parallel double quantum dot Josephson junctions based on closely spaced double nanowires bridged by *in-situ* deposited superconductors. The parallel double dot behavior occurs despite the proximity of the two nanowires and the potential risk of nanowire clamping during growth. By tuning the charge filling and lead couplings, we map out the parallel double quantum dot Yu-Shiba-Rusinov phase diagram. Our quasi-independent two-wire hybrids show promise for the realization of exotic topological phases.

DOI: [10.1103/PhysRevResearch.3.033240](https://doi.org/10.1103/PhysRevResearch.3.033240)

## I. INTRODUCTION

Double Rashba-nanowires bridged by superconductors are at the center of proposals for qubits [1], coupled subgap states [2], and exotic topological superconducting phases based on Majorana zero modes (MZMs) [3–16]. Researchers have theorized on the existence of a topological Kondo phase in such wires when the bridging superconductor is in Coulomb blockade [3,4,15,17] and, more recently, described a device hosting parafermions [6]. Realization of these proposals should benefit from material science developments, resulting in improved nanowire-superconductor interfaces with low quasiparticle poisoning rates [18–20].

These clean interfaces have been used in the pursuit of MZMs in single nanowires [19,21] and, more recently, for coupling single and serial quantum dots (QDs) defined on single nanowires to superconductors to realize one and two-impurity Yu-Shiba-Rusinov (YSR) models [22–26]. YSR states, belonging to the class of Andreev bound states [23–25,27–39], arise in the limit of large Coulomb charging energy,  $U > \Delta$ , as a result of the virtual excitation of a quasiparticle into the edge of the superconducting gap [40,41]. This quasiparticle can exchange-fluctuate with a localized spin in

the QD, and if the exchange coupling is strong (i.e., when the Kondo temperature,  $T_K$ , is larger than  $\sim 0.3\Delta$ ), the ground state (GS) changes from a doublet to a singlet [42]. In Josephson junctions (JJs), this induces a  $\pi$ -0 phase-shift change in the superconducting phase difference [22,23,43–59].

Devices which use pairs of QDs placed in a parallel configuration [60–62] and coupled to common superconducting leads have been extensively studied with the purpose of producing entangled electron states through Cooper pair splitting [63–66]. However, the behavior of the switching current,  $I_{sw}$ , in the presence of YSR screening [23,37,67] in parallel double QDs remains to be investigated.

In this paper, we characterize superconductivity in closely spaced pairs of InAs nanowires bridged by a thin epitaxial superconducting aluminum film deposited *in situ* [68]. To do so, we fabricate two side-by-side JJs out of one pair of nanowires and demonstrate that each nanowire hosts a single QD, through which supercurrent flows. From the charge stability diagram and magnetic field measurements, we establish that the interwire tunneling at the junction is negligible with an upper bound of  $\sim 50 \mu\text{eV}$ . The YSR physics is analyzed through the gate dependence of the linear conductance and  $I_{sw}$ , where we find that the common superconducting leads screen *individually* each QD, hinting at individual YSR clouds instead of a single one extending over the two QDs. We furthermore show indications of supercurrent interference when the GS parities of the QDs are different, reminiscent of a superconducting quantum interference device (SQUID) at zero magnetic field.

The paper is structured in sections. In Sec. II, we introduce the YSR double QD phase diagram and measurements

\*k\_grove@nbi.ku.dk

TABLE I. Parameters for shells W, X, Y of device 1. The charging energies,  $U_{L,R}$ , are extracted from Coulomb diamond spectroscopy. The total tunneling rates of each QD,  $\Gamma_{L,R}$ , are obtained by (a) fitting the even side of Coulomb diamonds in the normal state or (b) from the full width at half maximum of the corresponding Coulomb peak. The Kondo temperature,  $T_K$ , is obtained by (c) fitting the Kondo peak (when applicable) or by (d) using the equation  $T_K = \frac{1}{2k_B} \sqrt{\Gamma U} e^{\pi \epsilon_0 (\epsilon_0 + U) / \Gamma U}$ , with  $\Gamma_{L,R}$ ,  $U_{L,R}$  as known values, and  $\epsilon_0 = \epsilon_{L,R}$  the level position of the corresponding QD. Extraction methods are presented in detail in SM, Sec. III. From the charge stability diagram, we extract similar side-gate and back-gate capacitances for the left and right QD in the order of  $C_{gl,gr,bg} \sim 1$  aF and thus the charging energies are dominated by the source and drain capacitances.

Shell	$U_L$ (meV)	$U_R$ (meV)	$\Gamma_L$ (meV)	$\Gamma_R$ (meV)	$\frac{\Gamma_L}{U_L}$	$\frac{\Gamma_R}{U_R}$	$k_B T_{K_L}$ (meV)	$k_B T_{K_R}$ (meV)	$\frac{k_B T_{K_L}}{0.3\Delta}$	$\frac{k_B T_{K_R}}{0.3\Delta}$
W	$3.8 \pm 0.5$	$2.3 \pm 0.3$	$0.23 \pm 0.02^a$	$0.6 \pm 0.1^b$	$0.06 \pm 0.01$	$0.26 \pm 0.05$	$(3.1 \pm 0.3) \times 10^{-5d}$	$0.03 \pm 0.01^d$	$6 \times 10^{-4}$	0.5
X	$3.7 \pm 0.5$	$1.1 \pm 0.3$	$0.33 \pm 0.01^a$	$0.55 \pm 0.05^d$	$0.09 \pm 0.01$	$0.5 \pm 0.1$	$(8 \pm 1) \times 10^{-5d}$	$0.07 - 0.18^{c,a}$	0.001	3.2
Y	$3.6 \pm 0.5$	$1.1 \pm 0.3$	$1.05 \pm 0.01^a$	$0.55 \pm 0.05^d$	$0.29 \pm 0.04$	$0.5 \pm 0.1$	$0.06 \pm 0.02^d$	$0.07 - 0.18^c$	1	3.2

<sup>a</sup>Using method (d), we extract 0.06 meV.

of two double QD shells in different coupling regimes are presented, establishing weak interdot coupling. In Sec. III, we show signatures of interference between the supercurrents flowing through each junction. In Sec. IV, we demonstrate the YSR screening evolution of  $I_{sw}$ . Finally, in Sec. V we present our conclusions and provide perspectives of our paper.

## II. CHARACTERIZATION OF THE PARALLEL QUANTUM-DOT JOSEPHSON JUNCTION

In this section, we outline the device layout and demonstrate the Josephson effect and weak interdot tunneling in device 1. Data from an additional device (device 2) is shown in the Supplemental Material (SM) [69,70].

Figure 1(a) shows a falsely colored scanning electron microscopy (SEM) image of device 1. Two 80-nm InAs nanowires (in green), grown close to each other in a molecular beam epitaxy chamber and each covered on three of its facets by an *in-situ* deposited 17-nm-thick layer of aluminum (in blue) [68], are individually picked with a micromanipulator and deposited on a Si/SiOx substrate with an oxide thickness of 275 nm. A resist mask is defined by electron beam lithography to selectively etch Al using the commercial etchant Transene-D, creating a parallel double JJ with  $\approx 100$ -nm-wide bare sections of the two nanowires as weak links. Ti/Au 5 nm/250-nm-thick contacts and individual nanowire side gates are deposited after a subsequent lithography step. Prior to the metal deposition step and without breaking vacuum, the Al native oxide is removed by argon milling to establish a good contact between Ti/Au and Al. The devices are measured in a dilution refrigerator at base temperature  $T = 30$  mK.

QDs are formed when the two nanowires are brought near depletion with the use of the individual side-gate voltages,  $V_{gL}$  and  $V_{gR}$ . The side gates are also used as plunger gates of the QDs. A global back gate  $V_{bg}$  is used to tune the coupling between the contacts and the QDs, allowing us to explore different coupling regimes. The combination of side gates and back gate also makes it easier to obtain a double QD shell structure. In Fig. 1(b), we sketch the tunneling rates of the QDs to the common superconducting leads (SC),  $\Gamma_{L1}$ ,  $\Gamma_{L2}$ ,  $\Gamma_{R1}$ , and  $\Gamma_{R2}$ , which may vary among different shells of the QDs and can be tuned by  $V_{bg}$ . The QDs may also be coupled

to each other by an interdot tunnel coupling,  $t_d$ . We identify the different shells by the letters W, X, Y. QD parameters extracted for these are given in Table I. For an overview of the different shells explored, see SM, Sec. I.

The source and the drain contacts of the device each branch out into two leads as shown in Fig. 1(a), enabling us to characterize the parallel JJs [71] in a four-terminal configuration (at the level of the leads) by applying a current,  $I_{bias}$ , from source to drain leads and measuring the voltage response,  $V$ , in a different pair of leads. In this way, we obtain  $I_{bias} - V$  curves which switch from a supercurrent branch at low  $I_{bias}$  to a high-slope dissipative branch at  $I_{sw}$ . Two such curves are shown in Figs. 1(c) and 1(d) for the open and Coulomb blockaded regimes, respectively. We measure  $I_{sw}$  up to 35 nA in the former regime and up to approximately 500 pA in the latter regime. Figure 1(d) is measured with QD<sub>L</sub> in Coulomb blockade and QD<sub>R</sub> near a Coulomb resonance. Note that the supercurrent exhibits hysteresis, as the switching is found at different currents for positive and negative applied bias. In the Coulomb blockade, the supercurrent branch shows a finite slope,  $R_S$ , which increases with  $\sim 1/I_{sw}$ ; however, this does not affect our identification of  $I_{sw}$  as a jump in the curve down to 5 pA (see SM, Sec. II). In our analysis below (Sec. III), we do not claim quantitative estimates of the critical current,  $I_c$  (which may be larger), but merely address the qualitative behavior of  $I_{sw}$ . From independent  $I_{bias} - V$  measurements in the open regime, we estimate an upper bound of the contact resistance between the metal-lead and the hybrid-nanowire in the order of 20  $\Omega$  (see SM for discussion).

As a guide to the different GS configurations accessed in this paper, we show in Fig. 1(e) a sketch of the phase diagram of the parallel double quantum dot (DQD) JJ versus coupling to the leads when the two QDs have *independent* GSs ( $t_d = 0$ ). The sketch corresponds to odd occupancy (1,1) of the QDs and it is valid for the large level-spacing regime,  $\Delta E_i > U_i$ , where  $i$  stands for left and right QDs. The independent-GS case is applicable to our device as most  $I_{sw}$  measurements are done away from the triple points of the QDs, where the effect of a finite  $t_d$  is negligible. GS changes occur when the total tunneling rates  $\Gamma_{L,R}$  of each of the QDs to the common superconducting leads surpass a threshold which depends on  $U_{L,R}/\Delta$  [31], where  $\Delta$  is the superconducting gap. Above this threshold, the spin of each QD is individually screened by the superconducting

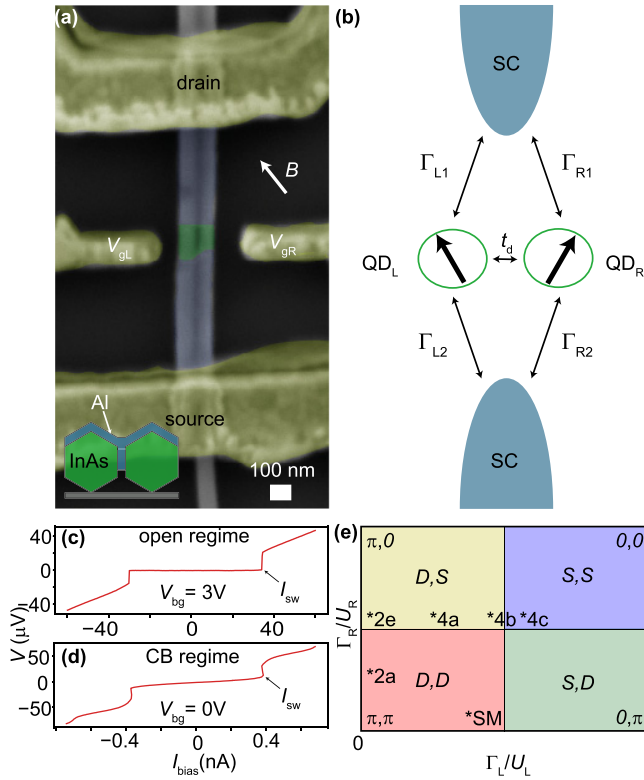


FIG. 1. (a) Scanning electron micrograph of device 1. Two nanowires with common superconducting leads form two parallel Josephson junctions. Side-by-side quantum dots serve as weak links for each JJ. The direction of an external in-plane magnetic field,  $B$ , when applied, is indicated by an arrow and has an angle of  $45^\circ$  with the device. In inset, a schematic cross section of the double nanowire is shown, indicating facets of the nanowires covered by Al at the leads. (b) Sketch of the two side QDs coupled to two superconducting leads. Interdot tunnel coupling,  $t_d$ , may be present. The GS parity of the left (L) and right (R) QDs is changed by tuning their level positions,  $\epsilon_L$  and  $\epsilon_R$ , or by increasing the total tunneling rates of each QD to the leads,  $\Gamma_L = \Gamma_{L1} + \Gamma_{L2}$  and  $\Gamma_R = \Gamma_{R1} + \Gamma_{R2}$ . (c,d)  $I_{\text{bias}} - V$  curves measured at  $V_{\text{bg}} = 3\text{ V}$  and  $V_{\text{bg}} = 0\text{ V}$  showing switching current,  $I_{\text{sw}}$ , in the open and in the Coulomb blocked regimes, respectively.  $I_{\text{bias}}$  is swept from negative to positive. (e) Sketch of the GS phase diagram depending on the tunneling rates  $\Gamma_i$  ( $i = L, R$ ) between the leads and the two QDs, when  $t_d = 0$  and each QD has an unpaired electron.  $D$  stands for doublet and  $S$  for singlet. The expected phase shift in the Josephson current-phase relationship of each QD JJ,  $0$  or  $\pi$ , is indicated. The qualitative  $\Gamma_L, \Gamma_R$  positions of different shells from Figs. 2, 4 and SM, Sec. VI (device 2) are indicated by asterisks.

leads via the YSR mechanism [2,72]. For a doublet GS, the current-phase relationship is  $\pi$  shifted, e.g.,  $I = I_c \sin(\phi + \pi)$  [45,47,49,54], as indicated in Fig. 1(e). The simple analysis above is valid when a single-level Coulomb-blockaded QD acts as a weak link instead of, e.g., a quantum point contact (single barrier), where a nonsinusoidal current-phase relationship applies [73].

To estimate  $t_d$ , we first investigate via two-terminal voltage-biased differential conductance ( $dI/dV$ ) measurements two shells corresponding to the two leftmost quadrants

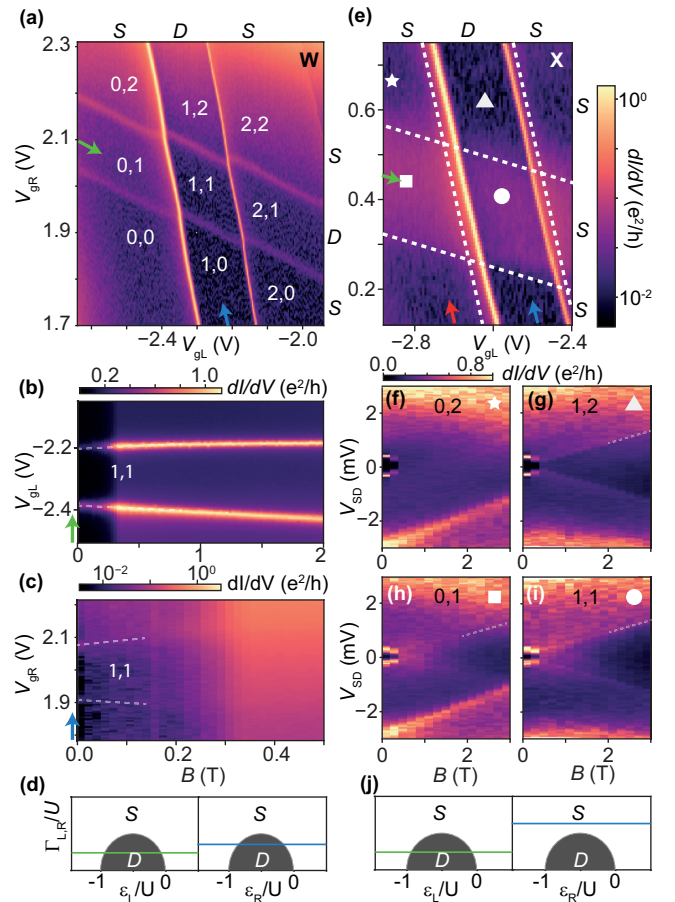


FIG. 2. (a), (e) Color maps of two-terminal, voltage-biased zero-bias differential conductance,  $dI/dV$ , in the superconducting state for shells W (a) and X (e) versus left and right QD plunger gates. In (a), charges  $N_L, N_R$  correspond to the charge occupation of the highest unoccupied energy level of each QD. In (e), white dashed lines represent the position of the Coulomb lines measured at  $B = 2\text{ T}$ . (b), (c) Zero-bias  $dI/dV$  color maps showing the magnetic field,  $B$ , dependence of parity transition lines which enclose the 1,1 charge sector in (a) versus plunger gate voltages of the (b) left and (c) right QDs, obtained by sweeping the gates along the green and blue arrows, shown in (a). For simplicity, only  $V_{\text{gL}}$  and  $V_{\text{gR}}$  are, respectively, shown. (f)–(i) Color maps of  $dI/dV$  versus magnetic field,  $B$ , and source-drain bias voltage,  $V_{\text{sd}}$ , taken in four different charge sectors indicated by symbols in (e). Higher  $B$  field measurement of (h) can be found in SM Sec. III. Dashed lines are added as a guide to the eye. (d), (j) Pairs of phase-diagram sketches for independent left and right QDs. Horizontal color-coded lines in each pair indicate qualitatively  $\Gamma_L$  ( $\Gamma_R$ ) versus left (right) QD level position  $\epsilon_L$  ( $\epsilon_R$ ) in the stability diagrams of (a) and (e), respectively, following the arrows shown.

of the DQD phase diagram in Fig. 1(e). The two-terminal  $dI/dV$  is recorded using standard lock-in amplifier techniques with an AC excitation of  $2\text{ }\mu\text{V}$ . Figure 2(a) shows a color map of  $dI/dV$  at source-drain bias  $V_{\text{SD}} = 0$  of shell W in the superconducting state versus  $V_{\text{gL}}$  and  $V_{\text{gR}}$ , which represents the stability diagram of the two QDs in the weakly-coupled regime where  $\Gamma_{L,R} \ll U_{L,R}$  (see Table I for shell parameters). Since the slope of the supercurrent branch,  $R_S$ , is empirically related in our device to  $1/I_{\text{sw}}$ , we can use

$R_S = 1/(dI/dV(V_{SD} = 0))$  as an indicator of the magnitude of  $I_{sw}$ . This is particularly relevant in the Coulomb-blockade regime, when  $I_{sw}$  is small and  $R_S$  is significant (see SM, Sec. II). We only use this empirical relation to comment on the voltage-biased measurements in Fig. 2. We observe approximately vertical and horizontal conductance lines which overlap and displace each other at their crossings, without exhibiting any significant bending. The displacement is a signature of a finite interdot charging energy, while the lack of bending indicates that  $t_d \approx 0$  (with an upper limit of  $50 \mu V$  based on the width of the sharpest conductance lines). No signatures of crossed-Andreev reflection (CAR) or of elastic cotunneling [74] are observed in this measurement. We interpret these lines as GS parity transition lines, which indicate changes of parity in the left and right QDs, respectively. The lines separate nine different and well-defined parity sectors. We assign corresponding effective left and right QD charges,  $N_L, N_R$ , to each of these sectors based on the shell-filling pattern of the stability diagram in larger plunger-gate ranges (see SM, Sec. I). The charges obtained in this way are indicated in Fig. 2(a). These charges correspond to the charge occupation of the highest unoccupied energy level of each QD.

To assign GS parities to these nine sectors, and to determine independently if, in addition to interdot charging energy, there is a significant  $t_d$ , we trace the evolution of the parity transition lines of the 1,1 charge sector against  $B$ . In the case of the singlet GS, i.e., when the spins of the two QDs are exchange-coupled (finite  $t_d$ ), these lines are expected to come together with  $B$  [75]. Instead, as shown in the zero-bias  $dI/dV$  color maps in Figs. 2(b) and 2(c), the parity transition lines enclosing the 1,1 charge sector split apart with  $B$ , i.e., the two QDs are independent doublets, despite the relative proximity of the two nanowires. The splitting of the parity lines occurs both in the case when the parity of the left (right) QD is varied and the right (left) QD is kept in the doublet GS [see green and blue arrow, respectively, in Fig. 2(a)]. The GS (singlet  $S$  or doublet  $D$ ) of the other eight charge sectors are indicated on the top and right exterior parts of the stability-diagram color map in Fig. 2(a).

Given the decoupling between the two QDs, we can approximate their phase diagrams by those of two independent single QDs. Neglecting the interdot charging energy, we sketch in Fig. 2(d) the well-known single-QD phase diagrams for the GS of the left and right QDs versus QD level position,  $\epsilon_{L,R}$ , and versus the total tunneling rate of each QD to the leads,  $\Gamma_{L,R}$ , over their charging energy,  $U_{L,R}$ . The doublet dome has an upper height limit of  $\Gamma_{L,R}/U_{L,R} = 1/2$  in the infinite  $\Delta$  limit, and its height decreases in the  $U \gg \Delta$  limit (i.e., the YSR regime) to which our QDs belong [34,76]. In the left phase diagram, the horizontal green line which crosses the doublet dome indicates a cut where  $\epsilon_L$  is varied and  $\epsilon_R$  is kept fixed such that the GS parity of the right QD is a doublet, and the GS parity of the left QD is variable. This line represents schematically the gate trajectory in Fig. 2(b), as indicated with the green arrow, which is collinear to the green arrow in Fig. 2(a), and which varies the parity of the left QD as  $S$ - $D$ - $S$  while keeping the parity of the right QD as  $D$ . A similar relation exists between the horizontal blue line in the right phase diagram and the gate trajectory (blue arrow) in Fig. 2(c), also collinear to the corresponding arrow

in Fig. 2(a). From these phase diagrams, we note that parity transitions are strictly equal to Coulomb degeneracies only at zero  $\Gamma_{L,R}$ . The measurements above confirm the expected DQD behavior for low lead couplings, which shows a  $D, D$  ground for charge state 1,1 corresponding to the lower left quadrant of the phase diagram in Fig. 1(e).

Next, we investigate a shell with different couplings to the leads (shell X) which belongs to the upper left quadrant of phase diagram in Fig. 1(e). Figure 2(e) shows the zero-bias  $dI/dV$  color map in the superconducting state versus the plunger gates of the two QDs of shell X. The two horizontal GS-parity transition lines, which bounded the green trajectory in the case of shell W, are absent in the case of shell X, and are instead replaced by a band of enhanced conductance. The conductance band is cut two times by approximately vertical conductance lines, which correspond to GS-parity transition lines of the left QD.

The parity of the band of enhanced conductance in the stability diagram is determined from the  $B$  evolution of the differential conductance in the normal state versus  $V_{sd}$  at two fixed gate voltages. These two gate voltages are indicated by a square (charge states 0,1) and a circle (1,1) in the stability diagram, and their  $B$  dependence is, respectively, shown in Figs. 2(h) and 2(i). As a control experiment, the  $B$  dependence for two fixed gate voltages above the conductance band indicated by a star (0,2) and a triangle (1,2) in the stability diagram, is shown in Figs. 2(f) and 2(g). The four measurements show closing of the superconducting gap at  $B = 0.4$  T, which is consistent with the jump in the zero-bias  $dI/dV$  signal in Figs. 2(b) and 2(c) at  $B \approx 0.4$  T. However, whereas Figs. 2(g)–2(i) (1,2 0,1 1,1) display conductance steps near zero bias which split with  $B$  field in the normal state, there is no such splitting in Fig. 2(f), consistent with even filling of both dots. We assign effective QD charge numbers to the charge stability diagram from a  $B = 2$  T measurement (see SM, Sec. III) and overlay the Coulomb lines obtained, which delimit the nine charge sectors [white dashed lines in Fig. 2(e)].

We note an additional important difference in the data of the low-bias splitting states. In Fig. 2(g) (1,2), the splitting can be traced back to zero bias at  $B = 0$ , while in Fig. 2(h) (0,1) the splitting is traced to zero bias only at a finite field of  $\approx 1$  T. The pair of features whose splitting can be traced to a  $B = 0$  onset in Fig. 2(g) (1,2) correspond to cotunneling steps of the odd-occupied left QD experiencing Zeeman splitting. In turn, the pair of features which starts to split at 1 T in Fig. 2(h) corresponds to the Zeeman splitting of a Kondo resonance in the right QD. The splitting ensues when  $E_Z \sim k_B T_{K_R}$  [77]. Notice that the Kondo resonance is also visible in the data after the gap closure at  $B = 0.4$  T. From the splitting, we find a  $g$ -factor  $g \sim 8.5 \pm 0.1$ . Table I shows that  $k_B T_{K_R} > 0.3\Delta$  for shell X, which is consistent with a YSR singlet state in the right QD in the superconducting state.

The  $B$ -dependence data in Figs. 2(f)–2(i) therefore allows us to assign the GS to the QDs,  $D$  or  $S$ , in each of the nine sectors in Fig. 2(e). We indicate schematically by a green and blue horizontal line in the two individual-QD phase diagrams in Fig. 2(j) the GS along the gate trajectories collinear to the same-colored arrows in the color map of Fig. 2(e). The green (blue) gate trajectory, which goes along (perpendicular to) the

band of enhanced conductance intersects twice (goes above) the doublet dome, leading to two (zero) parity transitions.

### III. SUPERCURRENT INTERFERENCE FOR DIFFERENT QUANTUM-DOT PARITIES

We switch back to the four-terminal measurement configuration to correlate the intrinsic phase of each JJ with the magnitude of  $I_{sw}$ . In Fig. 3, we show  $I_{sw}$  versus plunger gate voltages, where  $I_{sw}$  is extracted in a similar fashion as in Fig. 1(d). In Figs. 3(a) and 3(c) [Figs. 3(b) and 3(d)], the plunger gate voltages are swept along trajectories which vary the occupation in the left (right) QD while keeping the occupation of the right (left) QD fixed, following the green (red, blue) arrows in Figs. 2(a) and 2(e), i.e., for shells W and X, respectively. For reference, we assign the expected phase shift in the current-phase relationship,  $\pi$  or  $0$ , based on the measured GS parities of the two QDs. This phase shift is accurate when at least one QD is in Coulomb blockade. The value of  $I_{sw}$  at the parity transitions may include a contribution due to the presence of bound states crossing zero energy. Hence, the magnitude of  $I_{sw}$  on transitions should not be taken into account.

The common phenomenology in the data is as follows. After a smooth buildup of  $I_{sw}$  toward a  $0 \rightarrow \pi$  transition, the current abruptly drops at the edge of the  $\pi$  domain, resulting in an asymmetric  $I_{sw}$  peak [49]. A pair of asymmetric peaks is seen in the data in Figs. 3(a)–3(c), as one of the QDs experiences parity transitions and therefore a sequence of  $0 - \pi - 0$  phase-shift changes. If the parity stays unchanged, such peaks are absent, as in Fig. 3(d). Instead,  $I_{sw}$  is smoothly

enhanced toward odd occupation of the right QD, which is YSR screened (i.e.,  $k_B T_K > 0.3\Delta$ ) [54]. Interestingly, when comparing the red and blue traces in Fig. 3(d), which correspond to different phase shifts ( $\pi$  and  $0$ , respectively) in the JJ formed by the left QD, we observe that  $I_{sw}$  is stronger near  $V_{gR} = 0.4$  V. Note that  $V_{gR} = 0.4$  V corresponds to the 1,1 charge state for the blue trace, and to the 0,1 charge state for the red trace. The exact magnitude of  $I_{sw}$  in that gate value for the red and blue curves is consistent with what is found in Fig. 3(c) in the ( $\square$ ) and ( $\circ$ ), respectively. We can interpret the reduction in  $I_{sw}$  at  $V_{gR} = 0.4$  V in the blue trace with respect to the red trace by considering the double nanowire device as a SQUID at zero threaded magnetic flux [45,47,54]. The  $I_c$  of a SQUID with a sinusoidal current-phase relation at zero flux can be written as [54]

$$I_c = \sqrt{(I_{c1} - I_{c2})^2 + 4I_{c1}I_{c2} \left| \cos\left(\frac{\delta_1 + \delta_2}{2}\right) \right|^2}, \quad (1)$$

where  $I_{c1,2}$  are the critical currents of the two JJs and  $\delta_{1,2}$  are the intrinsic phase shifts ( $0$  or  $\pi$ ) of the junctions. As a result, the total  $I_c$  is given by  $I_{c\square} = I_{c1} + I_{c2}$  when the DQD is in the  $0,0$  phase and  $I_{c\circ} = I_{c1} - I_{c2}$  in the  $\pi,0$  phase. These equations can explain the findings in Figs. 3(c) and 3(d), as  $I_{sw}$  is enhanced when both JJs have the same intrinsic phase, and it is weaker when the two JJs have different phases.

### IV. SCREENING EVOLUTION OF SWITCHING CURRENT

Finally, we demonstrate individual control of the couplings between the SC leads and the QDs, realizing the transition from the upper left (one screened spin in 1,1) to upper right quadrant (both spins screened) in the YSR phase diagram depicted in Fig. 1(e). Whereas the changes in GS parity in Fig. 2 occurred primarily by changing the side-gate voltages to go from shell W to shell X, here the changes occur within a unique shell. This is done in a shell identified as Y, using  $V_{bg}$  as a tuning knob of  $\Gamma_{L,R}$ . In Figs. 4(a)–4(c), we show color maps representing parity stability diagrams at different  $V_{bg}$  analogous to those in Figs. 2(a) and 2(e); however, instead of plotting a measurement of voltage-biased  $dI/dV$ , we directly plot a four-terminal measurement of  $I_{sw}$  versus plunger-gate voltages. To obtain each color map, we measure the  $I_{bias} - V$  characteristic at each plunger gate voltage coordinate (i.e., at each pixel in the color map) and extract  $I_{sw}$  as in the example in Fig. 1(d).

In Fig. 4(a), the  $I_{sw}$  parity stability diagram shows two  $I_{sw}$  peaks which correspond to two parity transitions of the left QD. The lack of right-QD parity transition lines indicates that the right QD is YSR screened. We corroborate that this is indeed the case from a measurement of  $T_{KR}$  at  $B = 0.4$  T in the normal state, and we find  $k_B T_{KR} > 0.3\Delta$  (see Table I). We also note that, although faintly visible here, a two-terminal  $dI/dV$  measurement of the stability diagram in otherwise the same conditions as here displays an horizontal band of (weakly) enhanced conductance, which is the same phenomenology identified in Fig. 2(d) with YSR spin screening. However, the enhancement is weak enough to preclude resolution of  $I_{sw}$ , and therefore a similar band of  $I_{sw}$  only shows at the right part of Fig. 4(a) ( $V_{gL} \approx -2.95$  V,  $V_{gR} \approx 0.45$  V).

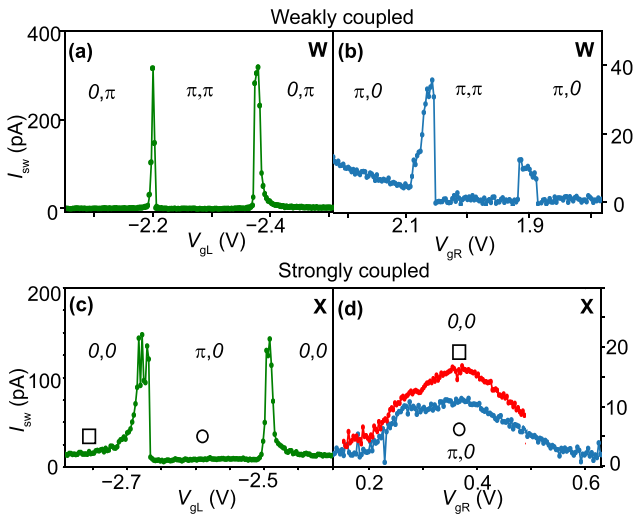


FIG. 3. (a)–(d) Extracted  $I_{sw}$  versus plunger-gate voltage trajectories collinear to same-colored arrows in [(a), (b)] Fig. 2(a), shell W, and (c), (d) Fig. 2(e), shell X. In (d), two traces are shown to illustrate the decrease in  $I_{sw}$  as a consequence of the subtracting effect of a  $\pi$  phase shift in one of the QD Josephson junctions. The red curve is offset on the gate axis to correct for the cross talk between the gates and the QDs. The  $I_{sw}$  is extracted by measuring the  $I_{bias} - V$  curve from negative to positive current for each gate value, and is identified as the switching on the positive current branch.

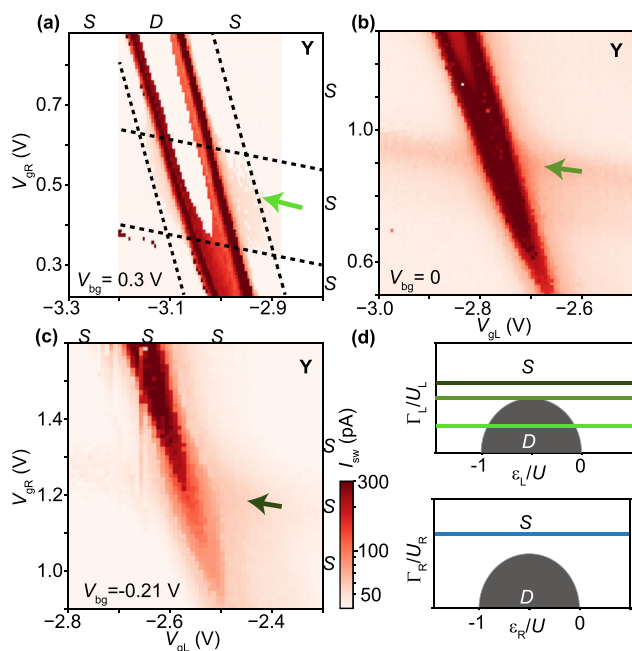


FIG. 4. (a)–(c) Color maps of  $I_{sw}$  as a function of the plunger gates of the two QDs, taken at three different  $V_{bg}$  values in shell Y. In (a), Coulomb lines positions (black dashed lines) are obtained from a normal-state two-terminal differential conductance measurement at  $B = 2$  T. To keep shell Y in frame, the effect of  $V_{bg}$  has been compensated by changing  $V_{gL}$  and  $V_{gR}$ . In (a) and (c), the GS of the two independent QDs is indicated on the exterior side of the color maps. (d) Independent-QD phase-diagram sketches as function tunneling rate  $\Gamma_{L,R}$  and QD level position,  $\epsilon_{L,R}$ , for the left QD (top panel) and right QD (lower panel). In the top panel, green-shaded horizontal lines indicate qualitatively  $\Gamma_L$  in directions collinear to the arrows of the same color in (a)–(c). The blue line indicates qualitatively  $\Gamma_R$  in (a)–(c). Note that decreasing the back-gate voltage results in stronger coupling to the left superconducting lead. The  $I_{sw}$  is extracted by measuring the  $I_{bias} - V$  curve from zero to positive current for each gate point.

Reducing  $V_{bg}$  alters the  $I_{sw}$  parity stability diagram by bringing the two  $I_{sw}$  peaks (parity lines) of the left QD closer together, as shown in Fig. 4(b). Note that a faint, approximately horizontal band of  $I_{sw}$  is observed along the direction pointed by the dark-green arrow, which comes as a result of enhancement of  $I_{sw}$  due to YSR spin-screening of the right QD. In Fig. 4(c), further reduction of  $V_{bg}$  leads to merging of the parity lines into a vertical band of  $I_{sw}$  across the whole plot. At this point, the spins of both QDs are YSR screened into singlets. We have therefore traced the phase diagram shown in Fig. 1(e), where either one spin of a QD or both are screened by the YSR mechanism, triggering a phase change in the current-phase relation of the JJs. Additional data on the magnetic field dependence of this shell can be found in the SM, Sec. IV.

## V. CONCLUSIONS AND OUTLOOK

In conclusion, we have demonstrated parallel QD JJs fabricated out of a double-nanowire platform in which the nanowires are bridged by an *in-situ* deposited superconductor.

We mapped out the parallel QD YSR phase diagram via conductance and switching current measurements showing the tunability of the GS of each JJ from doublet to singlet. The analysis also revealed that the nanowires are predominantly decoupled with an upper bound on the dot tunnel coupling in the order of  $t_d \leq 50 \mu\text{eV}$  for the specific charge states studied in two devices (see SM, Sec. VI). A lower bound is hard to identify due to the lack of evident anticross in device 1, but in device 2 the lower bound of  $t_d$  is estimated to be in the same order of magnitude as the upper bound. In general, other shells may be stronger coupled at higher gate voltages and the interdot tunnel coupling may be increased by adjusting nanowire growth parameters [68]. Finally, we showed indications of switching current addition and subtraction via appropriate choice of GSs of the two dots involving the YSR singlet state, i.e.,  $0, 0$  and  $\pi, 0$  (phase difference) regimes, respectively.

The above observations of basic superconducting properties in *in-situ* made hybrid double nanowire material open up for more advanced experiments addressing a number of recent theoretical proposals. In parallel double-QD Cooper-pair splitters [63,78], the CAR mechanism responsible for the splitting is weakened by an increase in the distance between the tunneling points from the superconductor into the two QDs [79]. The proximity of the nanowires set by growth [68] and the cleanness of the Al-InAs interface may turn out to be beneficial for CAR, which is also the basis for creating coupled YSR states in these systems [2,80]. The latter is investigated in a parallel work on the same hybrid double nanowire material [68] as used in this paper [67]. The hybrid double nanowires are furthermore prime candidates for realizing several species of topological subgap states [5,6]. For finite CAR, the requirements for entering the topological regime hosting Majorana bound states have been shown to be lowered [8,12], and parafermions may be achieved in a regime where CAR dominates over local Andreev processes [6]. In superconducting islands fabricated in our hybrid double nanowires, the topological Kondo effect can be pursued [3,4,15], and in JJs as here demonstrated, nonstandard types of Andreev bound states have been predicted [14] in the topological regime. Furthermore, a  $\varphi_0$  junction geometry can be investigated in the double nanowire platform by implementing the double nanowires in a SQUID. As an ending remark, we note that double nanowires can also be made with a full superconducting shell [68,81], relevant for investigating flux-induced subgap states [24,82,83].

## ACKNOWLEDGMENTS

We thank Gorm Steffensen, Jens Paaske, Michele Burdello, and Constantin Schrade for useful discussions and Xinyan Wang for experimental contribution. We acknowledge the support of the Sino-Danish Center, the European Union’s Horizon 2020 research and innovation program under the Marie Skłodowska-Curie Grant Agreement No. 832645, QuantERA SuperTop (NN 127900), the European Union’s Horizon 2020 research and innovation programme FETOpen Grant No. 828948 (AndQC), the Danish National Research Foundation, Villum Foundation (Research Grant No. 25310), the Ministry of Science and Technology of China through the

National Key Research and Development Program of China (Grants No. 2017YFA0303304 and No. 2016YFA0300601), the National Natural Science Foundation of China (Grant No.

11874071), the Beijing Academy of Quantum Information Sciences (Grant No. Y18G22), Carlsberg Foundation and the Independent Research Fund Denmark.

- [1] D. Aasen, M. Hell, R. V. Mishmash, A. Higginbotham, J. Danon, M. Leijnse, T. S. Jespersen, J. A. Folk, C. M. Marcus, K. Flensberg, and J. Alicea, Milestones toward Majorana-Based Quantum Computing, *Phys. Rev. X* **6**, 031016 (2016).
- [2] N. Y. Yao, C. P. Moca, I. Weymann, J. D. Sau, M. D. Lukin, E. A. Demler, and G. Zaránd, Phase diagram and excitations of a Shiba molecule, *Phys. Rev. B* **90**, 241108(R) (2014).
- [3] B. Béri and N. R. Cooper, Topological Kondo Effect with Majorana Fermions, *Phys. Rev. Lett.* **109**, 156803 (2012).
- [4] A. Altland and R. Egger, Multiterminal Coulomb-Majorana Junction, *Phys. Rev. Lett.* **110**, 196401 (2013).
- [5] E. Gaidamauskas, J. Paaske, and K. Flensberg, Majorana Bound States in Two-Channel Time-Reversal-Symmetric Nanowire Systems, *Phys. Rev. Lett.* **112**, 126402 (2014).
- [6] J. Klinovaja and D. Loss, Time-reversal invariant parafermions in interacting Rashba nanowires, *Phys. Rev. B* **90**, 045118 (2014).
- [7] H. Ebisu, B. Lu, J. Klinovaja, and Y. Tanaka, Theory of time-reversal topological superconductivity in double Rashba wires: Symmetries of Cooper pairs and Andreev bound states, *Prog. Theor. Exp. Phys.* **2016**, 083101 (2016).
- [8] C. Schrade, M. Thakurathi, C. Reeg, S. Hoffman, J. Klinovaja, and D. Loss, Low-field topological threshold in Majorana double nanowires, *Phys. Rev. B* **96**, 035306 (2017).
- [9] C. Reeg, J. Klinovaja, and D. Loss, Destructive interference of direct and crossed Andreev pairing in a system of two nanowires coupled via an  $s$ -wave superconductor, *Phys. Rev. B* **96**, 081301(R) (2017).
- [10] C. Schrade and L. Fu, Parity-controlled  $2\pi$  Josephson Effect Mediated by Majorana Kramers Pairs, *Phys. Rev. Lett.* **120**, 267002 (2018).
- [11] M. Thakurathi, P. Simon, I. Mandal, J. Klinovaja, and D. Loss, Majorana Kramers pairs in Rashba double nanowires with interactions and disorder, *Phys. Rev. B* **97**, 045415 (2018).
- [12] O. Dmytruk, M. Thakurathi, D. Loss, and J. Klinovaja, Majorana bound states in double nanowires with reduced Zeeman thresholds due to supercurrents, *Phys. Rev. B* **99**, 245416 (2019).
- [13] M. Thakurathi, D. Chevallier, D. Loss, and J. Klinovaja, Transport signatures of bulk topological phases in double Rashba nanowires probed by spin-polarized STM, *Phys. Rev. Research* **2**, 023197 (2020).
- [14] P. Kotetes, M. T. Mercaldo, and M. Cuoco, Synthetic Weyl Points and Chiral Anomaly in Majorana Devices With Non-standard Andreev-Bound-State Spectra, *Phys. Rev. Lett.* **123**, 126802 (2019).
- [15] M. Papaj, Z. Zhu, and L. Fu, Multichannel charge Kondo effect and non-Fermi-liquid fixed points in conventional and topological superconductor islands, *Phys. Rev. B* **99**, 014512 (2019).
- [16] A. Haim and Y. Oreg, Time-reversal-invariant topological superconductivity in one and two dimensions, *Phys. Rep.* **825**, 1 (2019).
- [17] M. R. Galpin, A. K. Mitchell, J. Temaismithi, D. E. Logan, B. Béri, and N. R. Cooper, Conductance fingerprint of Majorana fermions in the topological Kondo effect, *Phys. Rev. B* **89**, 045143 (2014).
- [18] P. Krogstrup, N. L. B. Ziino, W. Chang, S. M. Albrecht, M. H. Madsen, E. Johnson, J. Nygård, C. M. Marcus, and T. S. Jespersen, Epitaxy of semiconductor–superconductor nanowires, *Nat. Mater.* **14**, 400 (2015).
- [19] S. M. Albrecht, A. P. Higginbotham, M. Madsen, F. Kuemmeth, T. S. Jespersen, J. Nygård, P. Krogstrup, and C. M. Marcus, Exponential protection of zero modes in Majorana islands, *Nature (London)* **531**, 206 (2016).
- [20] A. P. Higginbotham, S. M. Albrecht, G. Kiršanskas, W. Chang, F. Kuemmeth, P. Krogstrup, T. S. Jespersen, J. Nygård, K. Flensberg, and C. M. Marcus, Parity lifetime of bound states in a proximitized semiconductor nanowire, *Nat. Phys.* **11**, 1017 (2015).
- [21] M. T. Deng, S. Vaitiekėnas, E. B. Hansen, J. Danon, M. Leijnse, K. Flensberg, J. Nygård, P. Krogstrup, and C. M. Marcus, Majorana bound state in a coupled quantum-dot hybrid-nanowire system, *Science* **354**, 1557 (2016).
- [22] J. C. Estrada Saldaña, A. Vekris, G. Steffensen, R. Žitko, P. Krogstrup, J. Paaske, K. Grove-Rasmussen, and J. Nygård, Supercurrent in a Double Quantum Dot, *Phys. Rev. Lett.* **121**, 257701 (2018).
- [23] J. C. Estrada Saldaña, A. Vekris, R. Žitko, G. Steffensen, P. Krogstrup, J. Paaske, K. Grove-Rasmussen, and J. Nygård, Two-impurity Yu-Shiba-Rusinov states in coupled quantum dots, *Phys. Rev. B* **102**, 195143 (2020).
- [24] M. Valentini, F. Peñaranda, A. Hofmann, M. Brauns, R. Hauschild, P. Krogstrup, P. San-Jose, E. Prada, R. Aguado, and G. Katsaros, Non-topological zero bias peaks in full-shell nanowires induced by flux tunable Andreev states, *Science* **373**, 82 (2021).
- [25] J. C. Estrada Saldaña, A. Vekris, V. Sosnovtseva, T. Kanne, P. Krogstrup, K. Grove-Rasmussen, and J. Nygård, Temperature induced shifts of Yu–Shiba–Rusinov resonances in nanowire-based hybrid quantum dots, *Commun. Phys.* **3**, 125 (2020).
- [26] D. Razmadze, E. C. T. O’Farrell, P. Krogstrup, and C. M. Marcus, Quantum Dot Parity Effects in Trivial and Topological Josephson Junctions, *Phys. Rev. Lett.* **125**, 116803 (2020).
- [27] M. R. Buitelaar, T. Nussbaumer, and C. Schönberger, Quantum Dot in the Kondo Regime Coupled to Superconductors, *Phys. Rev. Lett.* **89**, 256801 (2002).
- [28] R. S. Deacon, Y. Tanaka, A. Oiwa, R. Sakano, K. Yoshida, K. Shibata, K. Hirakawa, and S. Tarucha, Tunneling Spectroscopy of Andreev Energy Levels in a Quantum Dot Coupled to a Superconductor, *Phys. Rev. Lett.* **104**, 076805 (2010).
- [29] R. S. Deacon, Y. Tanaka, A. Oiwa, R. Sakano, K. Yoshida, K. Shibata, K. Hirakawa, and S. Tarucha, Kondo-enhanced Andreev transport in single self-assembled InAs quantum dots contacted with normal and superconducting leads, *Phys. Rev. B* **81**, 121308(R) (2010).
- [30] J.-D. Pillet, C. H. L. Quay, P. Morfin, C. Bena, A. L. Yeyati, and P. Joyez, Andreev bound states in supercurrent-carrying carbon nanotubes revealed, *Nat. Phys.* **6**, 965 (2010).



- [31] E. J. H. Lee, X. Jiang, M. Houzet, R. Aguado, C. M. Lieber, and S. De Franceschi, Spin-resolved Andreev levels and parity crossings in hybrid superconductor–semiconductor nanostructures, *Nat. Nanotechnol.* **9**, 79 (2014).
- [32] A. Jellinggaard, K. Grove-Rasmussen, M. H. Madsen, and J. Nygård, Tuning Yu-Shiba-Rusinov states in a quantum dot, *Phys. Rev. B* **94**, 064520 (2016).
- [33] S. Li, N. Kang, P. Caroff, and H. Q. Xu,  $0-\pi$  phase transition in hybrid superconductor–InSb nanowire quantum dot devices, *Phys. Rev. B* **95**, 014515 (2017).
- [34] E. J. H. Lee, X. Jiang, R. Žitko, R. Aguado, C. M. Lieber, and S. De Franceschi, Scaling of subgap excitations in a superconductor–semiconductor nanowire quantum dot, *Phys. Rev. B* **95**, 180502(R) (2017).
- [35] Z. Su, A. B. Tacla, M. Hocevar, D. Car, S. R. Plissard, E. P. A. M. Bakkers, A. J. Daley, D. Pekker, and S. M. Frolov, Andreev molecules in semiconductor nanowire double quantum dots, *Nat. Commun.* **8**, 585 (2017).
- [36] J. Gramich, A. Baumgartner, and C. Schönberger, Andreev bound states probed in three-terminal quantum dots, *Phys. Rev. B* **96**, 195418 (2017).
- [37] K. Grove-Rasmussen, G. Steffensen, A. Jellinggaard, M. H. Madsen, R. Žitko, J. Paaske, and J. Nygård, Yu-Shiba-Rusinov screening of spins in double quantum dots, *Nat. Commun.* **9**, 2376 (2018).
- [38] Z. Su, R. Žitko, P. Zhang, H. Wu, D. Car, S. R. Plissard, S. Gazibegovic, G. Badawy, M. Hocevar, J. Chen, E. P. A. M. Bakkers, and S. M. Frolov, Erasing odd-parity states in semiconductor quantum dots coupled to superconductors, *Phys. Rev. B* **101**, 235315 (2020).
- [39] E. Prada, P. San-Jose, M. W. A. de Moor, A. Geresdi, E. J. H. Lee, J. Klinovaja, D. Loss, J. Nygård, R. Aguado, and L. P. Kouwenhoven, From Andreev to Majorana bound states in hybrid superconductor–semiconductor nanowires, *Nat. Rev. Phys.* **2**, 575 (2020).
- [40] R. Žitko, J. S. Lim, R. López, and R. Aguado, Shiba states and zero-bias anomalies in the hybrid normal–superconductor Anderson model, *Phys. Rev. B* **91**, 045441 (2015).
- [41] G. Kiršanskas, M. Goldstein, K. Flensberg, L. I. Glazman, and J. Paaske, Yu-Shiba-Rusinov states in phase-biased superconductor–quantum dot–superconductor junctions, *Phys. Rev. B* **92**, 235422 (2015).
- [42] K. Satori, H. Shiba, O. Sakai, and Y. Shimizu, Numerical renormalization group study of magnetic impurities in superconductors, *J. Phys. Soc. Jpn.* **61**, 3239 (1992).
- [43] J. Bauer, A. Oguri, and A. C. Hewson, Spectral properties of locally correlated electrons in a Bardeen–Cooper–Schrieffer, *J. Phys.: Condens. Matter* **19**, 486211 (2007).
- [44] A. V. Rozhkov, D. P. Arovas, and F. Guinea, Josephson coupling through a quantum dot, *Phys. Rev. B* **64**, 233301 (2001).
- [45] J. A. Van Dam, Y. V. Nazarov, E. P. A. M. Bakkers, S. De Franceschi, and L. P. Kouwenhoven, Supercurrent reversal in quantum dots, *Nature (London)* **442**, 667 (2006).
- [46] F. S. Bergeret, A. L. Yeyati, and A. Martín-Rodero, Interplay between Josephson effect and magnetic interactions in double quantum dots, *Phys. Rev. B* **74**, 132505 (2006).
- [47] J.-P. Cleuziou, W. Wernsdorfer, V. Bouchiat, T. Ondarçuhu, and M. Monthieux, Carbon nanotube superconducting quantum interference device, *Nat. Nanotechnol.* **1**, 53 (2006).
- [48] K. Grove-Rasmussen, H. I. Jørgensen, and P. E. Lindelof, Kondo resonance enhanced supercurrent in single wall carbon nanotube Josephson junctions, *New J. Phys.* **9**, 124 (2007).
- [49] H. I. Jørgensen, T. Novotný, K. Grove-Rasmussen, K. Flensberg, and P. E. Lindelof, Critical current  $0-\pi$  transition in designed Josephson quantum dot junctions, *Nano Lett.* **7**, 2441 (2007).
- [50] A. Eichler, R. Deblock, M. Weiss, C. Karrasch, V. Meden, C. Schönberger, and H. Bouchiat, Tuning the Josephson current in carbon nanotubes with the Kondo effect, *Phys. Rev. B* **79**, 161407(R) (2009).
- [51] S. De Franceschi, L. Kouwenhoven, C. Schönberger, and W. Wernsdorfer, Hybrid superconductor–quantum dot devices, *Nat. Nanotechnol.* **5**, 703 (2010).
- [52] R. Žitko, M. Lee, R. López, R. Aguado, and M.-S. Choi, Josephson current in strongly correlated double quantum dots, *Phys. Rev. Lett.* **105**, 116803 (2010).
- [53] A. Martín-Rodero and A. Levy Yeyati, Josephson and Andreev transport through quantum dots, *Adv. Phys.* **60**, 899 (2011).
- [54] R. Maurand, T. Meng, E. Bonet, S. Florens, L. Marty, and W. Wernsdorfer, First-Order  $0-\pi$  Quantum Phase Transition in the Kondo Regime of a Superconducting Carbon-Nanotube Quantum Dot, *Phys. Rev. X* **2**, 011009 (2012).
- [55] B.-K. Kim, Y.-H. Ahn, J.-J. Kim, M.-S. Choi, M.-H. Bae, K. Kang, J. S. Lim, R. López, and N. Kim, Transport Measurement of Andreev Bound States in a Kondo-Correlated Quantum Dot, *Phys. Rev. Lett.* **110**, 076803 (2013).
- [56] R. Delagrangé, D. J. Luitz, R. Weil, A. Kasumov, V. Meden, H. Bouchiat, and R. Deblock, Manipulating the magnetic state of a carbon nanotube Josephson junction using the superconducting phase, *Phys. Rev. B* **91**, 241401(R) (2015).
- [57] R. Delagrangé, R. Weil, A. Kasumov, M. Ferrier, H. Bouchiat, and R. Deblock,  $0-\pi$  Quantum transition in a carbon nanotube Josephson junction: Universal phase dependence and orbital degeneracy, *Physica B* **536**, 211 (2018).
- [58] V. Meden, The Anderson–Josephson quantum dot—a theory perspective, *J. Phys.: Condens. Matter* **31**, 163001 (2019).
- [59] J. C. Estrada Saldaña, R. Žitko, J. P. Cleuziou, E. J. H. Lee, V. Zannier, D. Ercolani, L. Sorba, R. Aguado, and S. De Franceschi, Charge localization and reentrant superconductivity in a quasi-ballistic InAs nanowire coupled to superconductors, *Sci. Adv.* **5**, eaav1235 (2019).
- [60] S. Baba, J. Sailer, R. S. Deacon, A. Oiwa, K. Shibata, K. Hirakawa, and S. Tarucha, Superconducting transport in single and parallel double InAs quantum dot Josephson junctions with nb-based superconducting electrodes, *Appl. Phys. Lett.* **107**, 222602 (2015).
- [61] R. S. Deacon, A. Oiwa, J. Sailer, S. Baba, Y. Kanai, K. Shibata, K. Hirakawa, and S. Tarucha, Cooper pair splitting in parallel quantum dot Josephson junctions, *Nat. Commun.* **6**, 7446 (2015).
- [62] B. Probst, F. Domínguez, A. Schroer, A. L. Yeyati, and P. Recher, Signatures of nonlocal cooper-pair transport and of a singlet-triplet transition in the critical current of a double-quantum-dot Josephson junction, *Phys. Rev. B* **94**, 155445 (2016).
- [63] L. Hofstetter, S. Csonka, J. Nygård, and C. Schönberger, Cooper pair splitter realized in a two-quantum-dot Y-junction, *Nature (London)* **461**, 960 (2009).

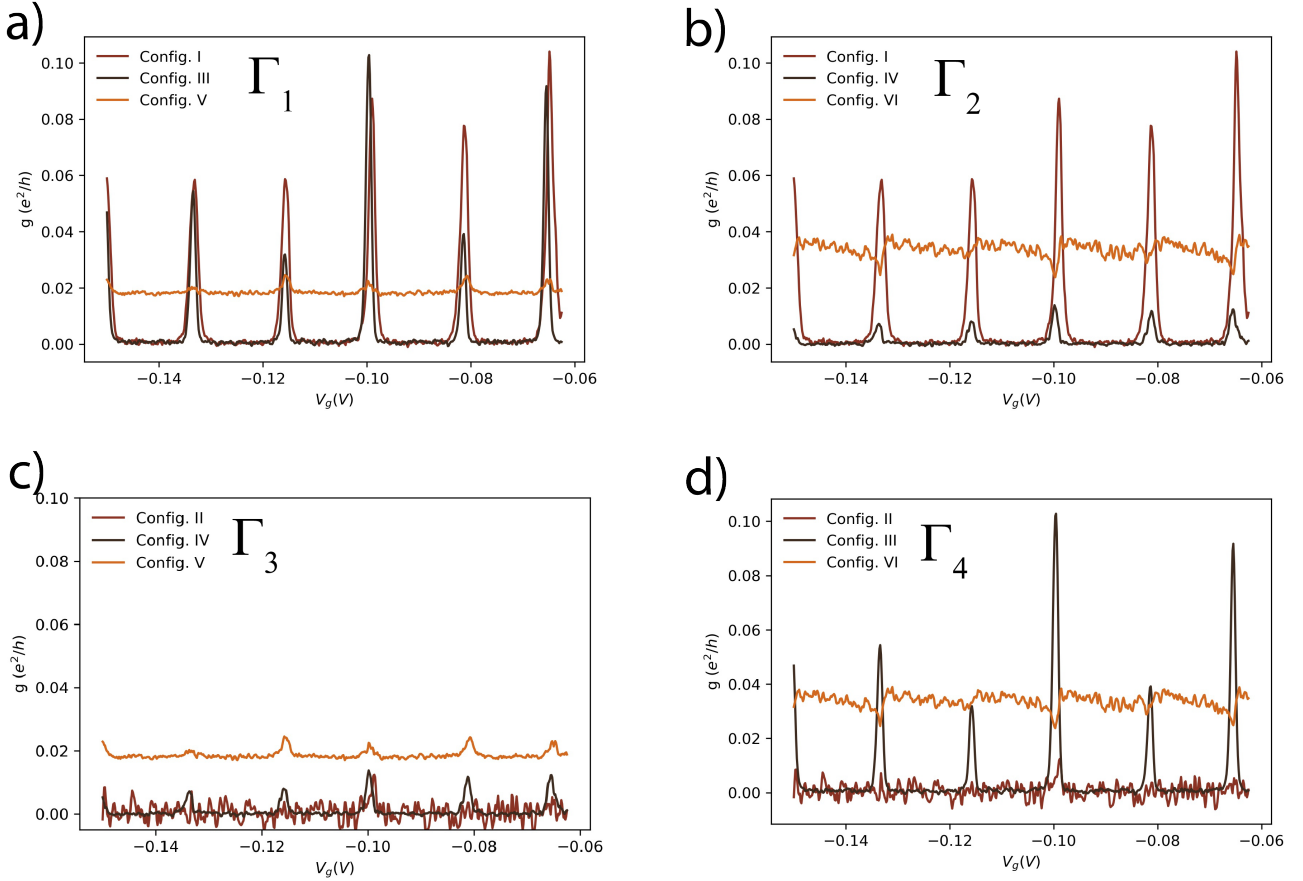
- [64] A. Das, Y. Ronen, M. Heiblum, D. Mahalu, A. V. Kretinin, and H. Shtrikman, High-efficiency Cooper pair splitting demonstrated by two-particle conductance resonance and positive noise cross-correlation, *Nat. Commun.* **3**, 1165 (2012).
- [65] S. Baba, C. Jünger, S. Matsuo, A. Baumgartner, Y. Sato, H. Kamata, K. Li, S. Jeppesen, L. Samuelson, H. Q. Xu, C. Schönenberger, and S. Tarucha, Cooper-pair splitting in two parallel InAs nanowires, *New J. Phys.* **20**, 063021 (2018).
- [66] K. Ueda, S. Matsuo, H. Kamata, S. Baba, Y. Sato, Y. Takeshige, K. Li, S. Jeppesen, L. Samuelson, H. Xu, and S. Tarucha, Dominant nonlocal superconducting proximity effect due to electron-electron interaction in a ballistic double nanowire, *Sci. Adv.* **5**, eaaw2194 (2019).
- [67] O. Kürtössy, Z. Scherübl, G. Fülöp, I. Endre Lukács, T. Kanne, J. Nygård, P. Makk, and S. Csonka, Andreev molecule in parallel InAs nanowires, [arXiv:2103.14083](https://arxiv.org/abs/2103.14083).
- [68] T. Kanne, D. Olsteins, M. Marnauza, A. Vekris, J. C. Estrada Saldaña, S. Loric, R. D. Schlosser, D. Ross, S. Csonka, K. Grove-Rasmussen, and J. Nygård, Double nanowires for hybrid quantum devices, [arXiv:2103.13938](https://arxiv.org/abs/2103.13938).
- [69] See Supplemental Material at <http://link.aps.org/supplemental/10.1103/PhysRevResearch.3.033240> for methods for analyzing the data and additional measurements.
- [70] Additional data as well as raw data used to produce the figures and Supplemental figures from the paper can be found at the repository ERDA of the University of Copenhagen at <https://doi.org/10.17894/ucph.9cfe99c5-c548-481c-bb19-dd544f53d46a>.
- [71] S. Guiducci, M. Carrega, F. Taddei, G. Biasiol, H. Courtois, F. Beltram, and S. Heun, Full electrostatic control of quantum interference in an extended trenched Josephson junction, *Phys. Rev. B* **99**, 235419 (2019).
- [72] R. Žitko, O. Bodensiek, and T. Pruschke, Effects of magnetic anisotropy on the subgap excitations induced by quantum impurities in a superconducting host, *Phys. Rev. B* **83**, 054512 (2011).
- [73] C. W. J. Beenakker and H. van Houten, The superconducting quantum point contact, in *Nanostructures and Mesoscopic Systems*, edited by W. P. Kirk and M. A. Reed (Academic Press, Cambridge, MA, USA, 1992), pp. 481–497.
- [74] Z. Scherübl, G. Fülöp, C. P. Moca, J. Gramich, A. Baumgartner, P. Makk, T. Elalaily, C. Schönenberger, J. Nygård, G. Zaránd, and S. Csonka, Large spatial extension of the zero-energy Yu–Shiba–Rusinov state in a magnetic field, *Nat. Commun.* **11**, 1834 (2020).
- [75] H. I. Jørgensen, K. Grove-Rasmussen, K.-Y. Wang, A. M. Blackburn, K. Flensberg, P. E. Lindelof, and D. A. Williams, Singlet–triplet physics and shell filling in carbon nanotube double quantum dots, *Nat. Phys.* **4**, 536 (2008).
- [76] T. Meng, S. Florens, and P. Simon, Self-consistent description of Andreev bound states in Josephson quantum dot devices, *Phys. Rev. B* **79**, 224521 (2009).
- [77] A. Kogan, S. Amasha, D. Goldhaber-Gordon, G. Granger, M. A. Kastner, and H. Shtrikman, Measurements of Kondo and Spin Splitting in Single-Electron Transistors, *Phys. Rev. Lett.* **93**, 166602 (2004).
- [78] L. G. Herrmann, F. Portier, P. Roche, A. L. Yeyati, T. Kontos, and C. Strunk, Carbon Nanotubes as Cooper-Pair Beam Splitters, *Phys. Rev. Lett.* **104**, 026801 (2010).
- [79] P. Recher, E. V. Sukhorukov, and D. Loss, Andreev tunneling, Coulomb blockade, and resonant transport of nonlocal spin-entangled electrons, *Phys. Rev. B* **63**, 165314 (2001).
- [80] Z. Scherübl, A. Pályi, and S. Csonka, Transport signatures of an Andreev molecule in a quantum dot-superconductor-quantum dot setup, *Beilstein J. Nanotechnol.* **10**, 363 (2019).
- [81] A. Vekris, J. C. Estrada Saldaña, J. de Bruijckere, S. Loric, T. Kanne, M. Marnauza, D. Olsteins, J. Nygård, and K. Grove-Rasmussen, Asymmetric little-parks oscillations in double nanowires, [arXiv:2106.01181](https://arxiv.org/abs/2106.01181).
- [82] S. Vaitiekėnas, G. W. Winkler, B. van Heck, T. Karzig, M.-T. Deng, K. Flensberg, L. I. Glazman, C. Nayak, P. Krogstrup, R. M. Lutchyn, and C. M. Marcus, Flux-induced topological superconductivity in full-shell nanowires, *Science* **367**, eaav3392 (2020).
- [83] F. Peñaranda, R. Aguado, P. San-Jose, and E. Prada, Even-odd effect and Majorana states in full-shell nanowires, *Phys. Rev. Research* **2**, 023171 (2020).

## C Additional data on DNW Island Devices

Here you can find all the appendices related to the Island chapter

### C.1 Grouping of zero-bias conductance peaks by coupling

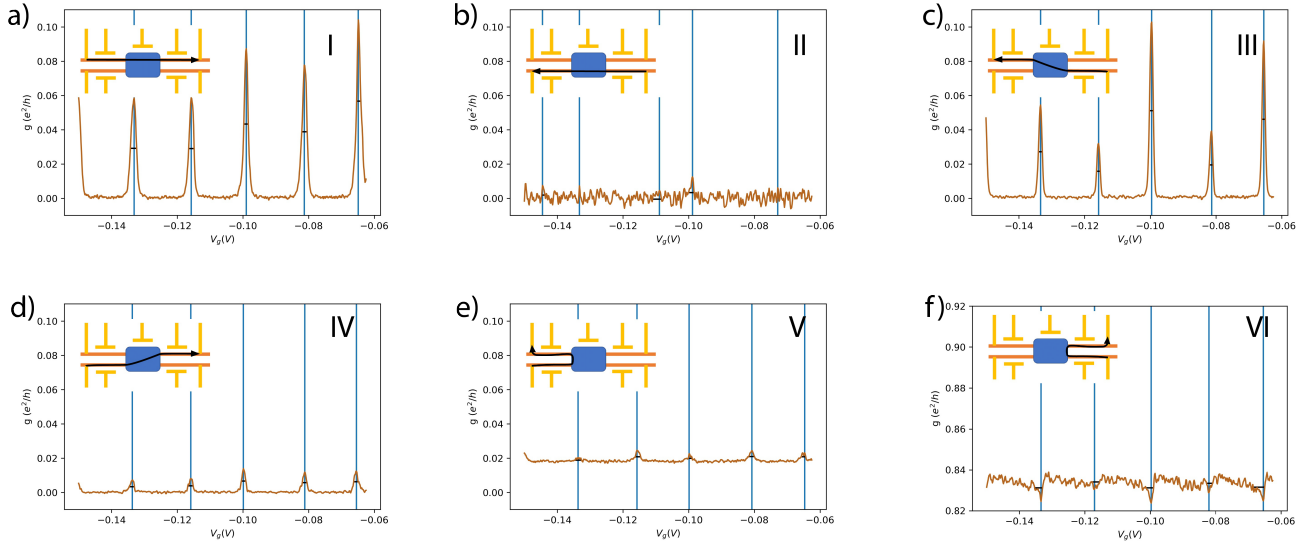
Figure C.5 displays the grouping of the zero-bias traces as described in sec. 6.6.2. Here all traces involving  $\Gamma_3$ , Fig. C.5c) is lower and more noisy than the rest of the couplings.



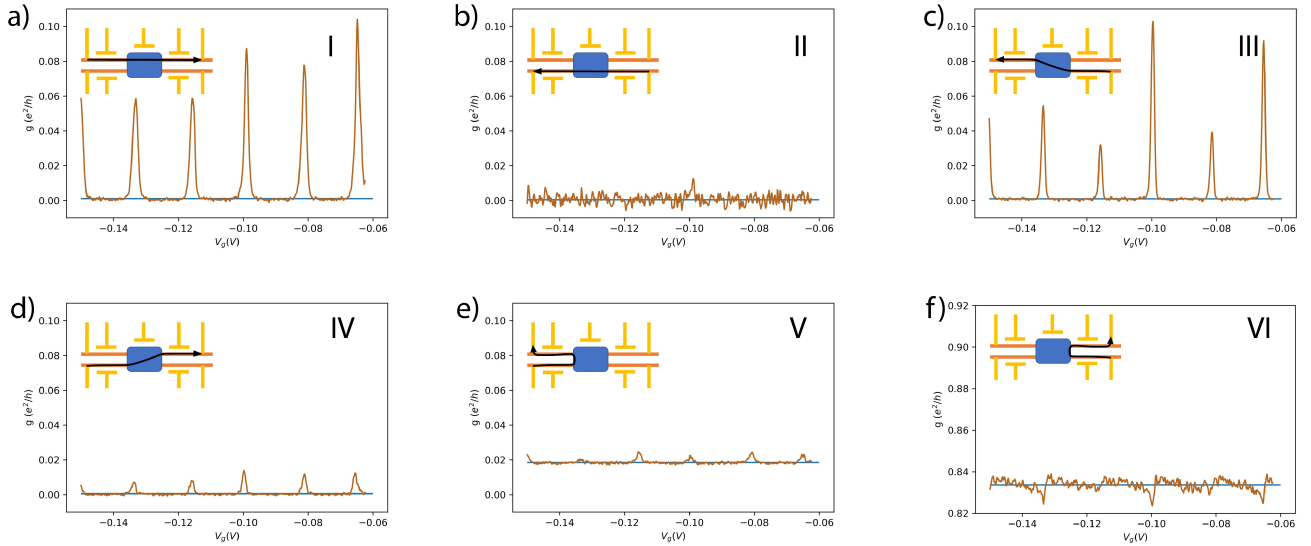
**Figure C.5: Zero bias peaks involving the specific couplings.** The three zero-bias traces involving a)  $\Gamma_1$  b)  $\Gamma_2$  c)  $\Gamma_3$  and d)  $\Gamma_4$ . In b) and d) the trace of configuration VI is shifted down by  $0.8 e^2/h$

Figure C.6 displays the locations of the exact peaks (blue lines) described in Sec. 6.6.2 and their FWHMs (black lines). In C.6b) it is apparent how the peak fitting is locating peaks caused by noise for configuration II. Furthermore, as depicted in C.6f) the peak localization for configuration VI is adjusted to find dips instead of peaks.

Figure C.7 displays the base conductance of the peaks in relation to the actual peaks described in Sec. 6.6.2.



**Figure C.6: Peak identification of the zero-bias traces for a DNW Island device.** The blue vertical lines define the exact positions of the peaks, described in Sec. 6.6.2, and the black horizontal lines defines their FWHM.



**Figure C.7: Base identification of the zero-bias traces for a DNW Island device.** The blue horizontal lines define the exact positions of the base, described in Sec. 6.6.2

## C.2 Zero-bias peaks conductance peaks

In Fig. C.8, the full data set used in Fig. 6.14b & c) are displayed. The deflections of the last data points is the result of switching, which is a change in effective potential on the device.

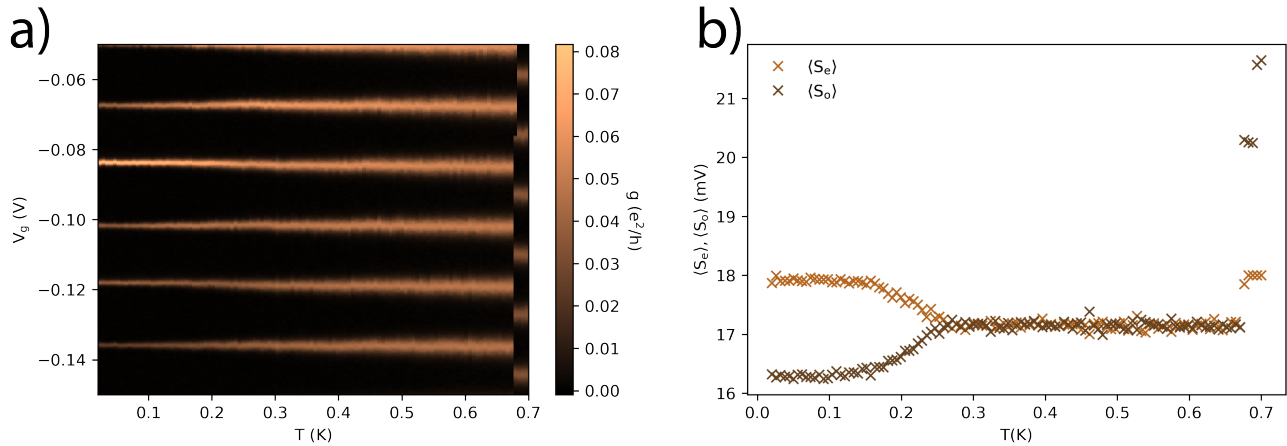


**Figure C.8: Full temperature dependence data.** In this figure the full data set used in Fig. 6.14b & c) are displayed. The deflections of the last data points is the result of switching, which is a change in effective potential on the device.

## References

- <sup>1</sup> David Aasen, Michael Hell, Ryan V. Mishmash, Andrew Higginbotham, Jeroen Danon, Martin Leijnse, Thomas S. Jespersen, Joshua A. Folk, Charles M. Marcus, Karsten Flensberg, and Jason Alicea. Milestones toward majorana-based quantum computing. *Physical Review X*, 6(3), 2016.
- <sup>2</sup> S. M. Albrecht, A. P. Higginbotham, M. Madsen, F. Kuemmeth, T. S. Jespersen, J. Nygård, P. Krogstrup, and C. M. Marcus. Exponential protection of zero modes in majorana islands. *Nature*, 531(7593):206–209, 2016.
- <sup>3</sup> S. M. Albrecht, E. B. Hansen, A. P. Higginbotham, F. Kuemmeth, T. S. Jespersen, J. Nygård, P. Krogstrup, J. Danon, K. Flensberg, and C. M. Marcus. Transport signatures of quasiparticle poisoning in a majorana island. *Physical Review Letters*, 118(13), 2017.
- <sup>4</sup> D. V. Averin and Yu. V. Nazarov. *Macroscopic Quantum Tunneling of Charge and Co-Tunneling*, pages 217–247. Springer US, Boston, MA, 1992.
- <sup>5</sup> S. Baba, C. Junger, S. Matsuo, A. Baumgartner, Y. Sato, H. Kamata, K. Li, S. Jeppesen, L. Samuelson, H. Q. Xu, C. Schonenberger, and S. Tarucha. Cooper-pair splitting in two parallel inas nanowires. *New Journal of Physics*, 20:8, 2018.
- <sup>6</sup> S. Baba, S. Matsuo, H. Kamata, R. S. Deacon, A. Oiwa, K. Li, S. Jeppesen, L. Samuelson, H. Q. Xu, and S. Tarucha. Gate tunable parallel double quantum dots in inas double-nanowire devices. *Applied Physics Letters*, 111(23):233513, 2017.
- <sup>7</sup> J. Bardeen, L. N. Cooper, and J. R. Schrieffer. Theory of superconductivity. *Physical Review*, 108(5):1175–1204, 1957.

- 
- <sup>8</sup> Graham Batey and Gustav Teleberg. Principles of dilution refrigeration - a brief technology guide. Report, [https://nanoscience.oxinst.com/assets/uploads/NanoScience/Brochures/Principles%20of%20dilution%20refrigeration\\_Sept15.pdf](https://nanoscience.oxinst.com/assets/uploads/NanoScience/Brochures/Principles%20of%20dilution%20refrigeration_Sept15.pdf), 2015.
- <sup>9</sup> M. Benito and Guido Burkard. Hybrid superconductor-semiconductor systems for quantum technology. *Applied Physics Letters*, 116(19):190502, 2020.
- <sup>10</sup> M. R. Buitelaar. *Electron Transport in Multiwall Carbon Nanotubes*. Thesis, 2004.
- <sup>11</sup> B. Béri and N. R. Cooper. Topological kondo effect with majorana fermions. *Physical Review Letters*, 109(15), 2012.
- <sup>12</sup> P. Caroff, K. A. Dick, J. Johansson, M. E. Messing, K. Deppert, and L. Samuelson. Controlled polytypic and twin-plane superlattices in iii-v nanowires. *Nature Nanotechnology*, 4(1):50–55, 2009.
- <sup>13</sup> Jaeyoon Cho and Kun Woo Kim. Quantum phase transition and entanglement in topological quantum wires. *Scientific Reports*, 7(1), 2017.
- <sup>14</sup> John Clarke. The proximity effect between superconducting and normal thin films in zero field. *Le Journal de Physique Colloques*, 29(C2):C2–3–C2–16, 1968.
- <sup>15</sup> A. A. Clerk, K. W. Lehnert, P. Bertet, J. R. Petta, and Y. Nakamura. Hybrid quantum systems with circuit quantum electrodynamics. *Nature Physics*, 16(3):257–267, 2020.
- <sup>16</sup> John F. Cochran and D. E. Mapother. Superconducting transition in aluminum. *Physical Review*, 111(1):132–142, 1958.
- <sup>17</sup> S. Csonka, L. Hofstetter, F. Freitag, S. Oberholzer, C. Schönenberger, T. S. Jespersen, M. Aagesen, and J. Nygård. Giant fluctuations and gate control of the g-factor in inas nanowire quantum dots. *Nano Letters*, 8(11):3932–3935, 2008.
- <sup>18</sup> S. Das Sarma, Jay D. Sau, and Tudor D. Stanescu. Splitting of the zero-bias conductance peak as smoking gun evidence for the existence of the majorana mode in a superconductor-semiconductor nanowire. *Physical Review B*, 86(22), 2012.
- <sup>19</sup> Shadi A. Dayeh, David P. R. Aplin, Xiaotian Zhou, Paul K. L. Yu, Edward T. Yu, and Deli Wang. High electron mobility inas nanowire field-effect transistors. *Small*, 3(2):326–332, 2007.
- <sup>20</sup> R. S. Deacon, A. Oiwa, J. Sailer, S. Baba, Y. Kanai, K. Shibata, K. Hirakawa, and S. Tarucha. Cooper pair splitting in parallel quantum dot josephson junctions. *Nature Communications*, 6(1):7446, 2015.

- 
- <sup>21</sup> SciPy developers. `scipy.optimize.curve_fit`. Web Page 10-01, [https://docs.scipy.org/doc/scipy/reference/generated/scipy.optimize.curve\\_fit.html](https://docs.scipy.org/doc/scipy/reference/generated/scipy.optimize.curve_fit.html), 2021.
- <sup>22</sup> SciPy developers. `scipy.signal.find_peaks`. Web Page 09-02, [https://docs.scipy.org/doc/scipy/reference/generated/scipy.signal.find\\_peaks.html](https://docs.scipy.org/doc/scipy/reference/generated/scipy.signal.find_peaks.html), 2021.
- <sup>23</sup> SciPy developers. `scipy.signal.peak_prominences`. Web Page 09-02, [https://docs.scipy.org/doc/scipy/reference/generated/scipy.signal.peak\\_prominences.html](https://docs.scipy.org/doc/scipy/reference/generated/scipy.signal.peak_prominences.html), 2021.
- <sup>24</sup> Kimberly A. Dick, Claes Thelander, Lars Samuelson, and Philippe Caroff. Crystal phase engineering in single inas nanowires. *Nano Letters*, 10(9):3494–3499, 2010.
- <sup>25</sup> Olesia Dmytruk, Manisha Thakurathi, Daniel Loss, and Jelena Klinovaja. Majorana bound states in double nanowires with reduced zeeman thresholds due to supercurrents. *Physical Review B*, 99(24), 2019.
- <sup>26</sup> Julian Eisenstein. Superconducting elements. *Reviews of Modern Physics*, 26(3):277–291, 1954.
- <sup>27</sup> OMEGA Engineering. Gpib. Web Page 09-02, <https://www.omega.co.uk/temperature/z/overviewieee.html>, 2021.
- <sup>28</sup> C. Fasth, A. Fuhrer, L. Samuelson, Vitaly N. Golovach, and Daniel Loss. Direct measurement of the spin-orbit interaction in a two-electron inas nanowire quantum dot. *Physical Review Letters*, 98(26), 2007.
- <sup>29</sup> K. Flensberg, J. Bindslev Hansen, and M. Octavio. Subharmonic energy-gap structure in superconducting weak links. *Physical Review B*, 38(13):8707–8711, 1988.
- <sup>30</sup> S. M. Frolov, M. J. Manfra, and J. D. Sau. Topological superconductivity in hybrid devices. *Nature Physics*, 16(7):718–724, 2020.
- <sup>31</sup> Liang Fu. Electron teleportation via majorana bound states in a mesoscopic superconductor. *Physical Review Letters*, 104(5), 2010.
- <sup>32</sup> L. J. Geerligs, V. F. Anderegg, J. Romijn, and J. E. Mooij. Single cooper-pair tunneling in small-capacitance junctions. *Physical Review Letters*, 65(3):377–380, 1990.
- <sup>33</sup> David J. Griffiths and Darrell F. Schroeter. *Introduction to Quantum Mechanics*. Cambridge University Press, Cambridge, 3 edition, 2018.
- <sup>34</sup> K. Grove-Rasmussen, T.S. Jespersen, A. Jellinggaard, and J. Nygård. *Hybrid Superconducting Devices Based on Quantum Wires*, book section 16, pages 459–491. Oxford University Press, first edition, 2017.

- 
- <sup>35</sup> Esben Bork Hansen, Jeroen Danon, and Karsten Flensberg. Probing electron-hole components of subgap states in coulomb blockaded majorana islands. *Physical Review B*, 97(4), 2018.
- <sup>36</sup> R. Hanson, L. P. Kouwenhoven, J. R. Petta, S. Tarucha, and L. M. K. Vandersypen. Spins in few-electron quantum dots. *Reviews of Modern Physics*, 79(4):1217–1265, 2007.
- <sup>37</sup> B van Heck, A R Akhmerov, F Hassler, M Burrello, and C W J Beenakker. Coulomb-assisted braiding of majorana fermions in a josephson junction array. *New Journal of Physics*, 14:035019, 2012.
- <sup>38</sup> Sebastian Heedt, Marina Quintero-Pérez, Francesco Borsoi, Alexandra Fursina, Nick Van Loo, Grzegorz P. Mazur, Michał P. Nowak, Mark Ammerlaan, Kongyi Li, Svetlana Korneychuk, Jie Shen, May An Y. Van De Poll, Ghada Badawy, Sasa Gazibegovic, Nick De Jong, Pavel Aseev, Kevin Van Hoogdalem, Erik P. A. M. Bakkers, and Leo P. Kouwenhoven. Shadow-wall lithography of ballistic superconductor–semiconductor quantum devices. *Nature Communications*, 12(1), 2021.
- <sup>39</sup> A. Higginbotham, P., S. Albrecht, M., G. Kiršanskas, W. Chang, F. Kuemmeth, P. Krogstrup, T. Jespersen, S., J. Nygård, K. Flensberg, and C. Marcus, M. Parity lifetime of bound states in a proximitized semiconductor nanowire. *Nature Physics*, 11(12):1017–1021, 2015.
- <sup>40</sup> L. Hofstetter, S. Csonka, J. Nygård, and C. Schönenberger. Cooper pair splitter realized in a two-quantum-dot y-junction. *Nature*, 461(7266):960–963, 2009.
- <sup>41</sup> R. Hützen, A. Zazunov, B. Braunecker, A. Levy Yeyati, and R. Egger. Majorana single-charge transistor. *Physical Review Letters*, 109(16), 2012.
- <sup>42</sup> Thomas Ihn. *Semiconductor nanostructures : Quantum states and electronic transport*, book section Quantum dots, pages 341–407. Oxford University Press, 2010.
- <sup>43</sup> Thomas Kanne, Mikelis Marnauza, Dags Olsteins, Damon J. Carrad, Joachim E. Sestoft, Joeri De Bruijkere, Lunjie Zeng, Erik Johnson, Eva Olsson, Kasper Grove-Rasmussen, and Jesper Nygård. Epitaxial pb on inas nanowires for quantum devices. *Nature Nanotechnology*, 16(7):776–781, 2021.
- <sup>44</sup> Thomas Kanne, Dags Olsteins, Mikelis Marnauza, Alexandros Vekris, Juan Carlos Estrada Saldana, Sara Loric, Rasmus D. Schlosser, Daniel Ross, Szabolcs Csonka, Kasper Grove-Rasmussen, and Jesper Nygård. Double nanowires for hybrid quantum devices. 2021.
- <sup>45</sup> Kento Ueda, Sadashige Matsuo, Hiroshi Kamata, Shoji Baba, Yosuke Sato, Yuusuke Takeshige, Kan Li, Sören Jeppesen, Lars Samuelson, Hongqi Xu, and Seigo Tarucha. Dominant nonlocal superconducting proximity effect due to electron-electron interaction in a ballistic double nanowire. *Science Advances*, 5(10):eaaw2194, 2019.



- 
- <sup>46</sup> Alexei Kitaev and John Preskill. Topological entanglement entropy. *Physical Review Letters*, 96(11), 2006.
- <sup>47</sup> Jelena Klinovaja and Daniel Loss. Time-reversal invariant parafermions in interacting rashba nanowires. *Physical Review B*, 90(4), 2014.
- <sup>48</sup> Leo P. Kouwenhoven, Charles M. Marcus, Paul L. McEuen, Seigo Tarucha, Robert M. Westervelt, and Ned S. Wingreen. *Mesoscopic Electron Transport*, book section ELECTRON TRANSPORT IN QUANTUM DOTS, pages 105–214. Springer Netherlands, 1997.
- <sup>49</sup> P. Krogstrup, N. L. B. Ziino, W. Chang, S. M. Albrecht, M. H. Madsen, E. Johnson, J. Nygård, C. Marcus, M., and T. S. Jespersen. Epitaxy of semiconductor–superconductor nanowires. *Nature Materials*, 14(4):400–406, 2015.
- <sup>50</sup> Olivér Kürtössy, Zoltán Scherübl, Gergő Fülöp, István Endre Lukács, Thomas Kanne, Jesper Nygård, Péter Makk, and Szabolcs Csonka. Andreev molecule in parallel inas nanowires. *Nano Letters*, 2021.
- <sup>51</sup> L. A. Landau, S. Plugge, E. Sela, A. Altland, S. M. Albrecht, and R. Egger. Towards realistic implementations of a majorana surface code. *Physical Review Letters*, 116(5), 2016.
- <sup>52</sup> S. Li, N. Kang, D. X. Fan, L. B. Wang, Y. Q. Huang, P. Caroff, and H. Q. Xu. Coherent charge transport in ballistic insb nanowire josephson junctions. *Scientific Reports*, 6(1):24822, 2016.
- <sup>53</sup> J. G. Lu, J. M. Hergenrother, and M. Tinkham. Magnetic-field-induced crossover from 2etoepiodicity in the superconducting single-electron transistor. *Physical Review B*, 53(6):3543–3549, 1996.
- <sup>54</sup> Roman M. Lutchyn, Jay D. Sau, and S. Das Sarma. Majorana fermions and a topological phase transition in semiconductor-superconductor heterostructures. *Physical Review Letters*, 105(7), 2010.
- <sup>55</sup> V. F. Maisi, S. V. Lotkhov, A. Kemppinen, A. Heimes, J. T. Muhonen, and J. P. Pekola. Excitation of single quasiparticles in a small superconducting al island connected to normal-metal leads by tunnel junctions. *Physical Review Letters*, 111(14), 2013.
- <sup>56</sup> Manisha Thakurathi, Pascal Simon, Ipsita Mandal, Jelena Klinovaja, and Daniel Loss. Majorana kramers pairs in rashba double nanowires with interactions and disorder. *Physical Review B*, 97(4), 2018.
- <sup>57</sup> B. T. Matthias, T. H. Geballe, and V. B. Compton. Superconductivity. *Reviews of Modern Physics*, 35(1):1–22, 1963.
- <sup>58</sup> Jan Petter Morten, Arne Brataas, and Wolfgang Belzig. Circuit theory of crossed andreev reflection. *Physical Review B*, 74(21), 2006.

- 
- <sup>59</sup> Jingwei Mu, Shaoyun Huang, Zhi-Hai Liu, Weijie Li, Ji-Yin Wang, Dong Pan, Guang-Yao Huang, Yuanjie Chen, Jianhua Zhao, and H. Q. Xu. A highly tunable quadruple quantum dot in a narrow bandgap semiconductor inas nanowire. *Nanoscale*, 13(7):3983–3990, 2021.
- <sup>60</sup> Włodzimierz Nakwaski. Effective masses of electrons and heavy holes in gaas, inas, alas and their ternary compounds. *Physica B: Condensed Matter*, 210(1):1–25, 1995.
- <sup>61</sup> H. A. Nilsson, P. Samuelsson, P. Caroff, and H. Q. Xu. Supercurrent and multiple andreev reflections in an insb nanowire josephson junction. *Nano Letters*, 12(1):228–233, 2012.
- <sup>62</sup> Malin Nilsson, Luna Namazi, Sebastian Lehmann, Martin Leijnse, Kimberly A. Dick, and Claes Thelander. Single-electron transport in inas nanowire quantum dots formed by crystal phase engineering. *Physical Review B*, 93(19), 2016.
- <sup>63</sup> Yuval Oreg, Gil Refael, and Felix Von Oppen. Helical liquids and majorana bound states in quantum wires. *Physical Review Letters*, 105(17), 2010.
- <sup>64</sup> A. Osterloh, Luigi Amico, G. Falci, and Rosario Fazio. Scaling of entanglement close to a quantum phase transition. *Nature*, 416(6881):608–610, 2002.
- <sup>65</sup> M. Pendharkar, B. Zhang, H. Wu, A. Zarassi, P. Zhang, C. P. Dempsey, J. S. Lee, S. D. Harrington, G. Badawy, S. Gazibegovic, R. L. M. Op Het Veld, M. Rossi, J. Jung, A.-H. Chen, M. A. Verheijen, M. Hocevar, E. P. A. M. Bakkers, C. J. Palmstrøm, and S. M. Frolov. Parity-preserving and magnetic field-resilient superconductivity in insb nanowires with sn shells. *Science*, 372(6541):508–511, 2021.
- <sup>66</sup> R. M. Potok, I. G. Rau, Hadas Shtrikman, Yuval Oreg, and D. Goldhaber-Gordon. Observation of the two-channel kondo effect. *Nature*, 446(7132):167–171, 2007.
- <sup>67</sup> Diego Rainis, Luka Trifunovic, Jelena Klinovaja, and Daniel Loss. Towards a realistic transport modeling in a superconducting nanowire with majorana fermions. *Physical Review B*, 87(2), 2013.
- <sup>68</sup> Christopher Reeg, Jelena Klinovaja, and Daniel Loss. Destructive interference of direct and crossed andreev pairing in a system of two nanowires coupled via an s-wave superconductor. *Physical Review B*, 96(8), 2017.
- <sup>69</sup> T. Sand-Jespersen, J. Paaske, B. M. Andersen, K. Grove-Rasmussen, H. I. Jørgensen, M. Aagesen, C. B. Sørensen, P. E. Lindelof, K. Flensberg, and J. Nygård. Kondo-enhanced andreev tunneling in inas nanowire quantum dots. *Physical Review Letters*, 99(12), 2007.
- <sup>70</sup> Jay D. Sau, Brian Swingle, and Sumanta Tewari. Proposal to probe quantum nonlocality of majorana fermions in tunneling experiments. *Physical Review B*, 92(2), 2015.

- 
- <sup>71</sup> Constantin Schrade, Manisha Thakurathi, Christopher Reeg, Silas Hoffman, Jelena Klinovaja, and Daniel Loss. Low-field topological threshold in majorana double nanowires. *Physical Review B*, 96(3), 2017.
- <sup>72</sup> Joachim E. Sestoft, Thomas Kanne, Aske Nørskov Gejl, Merlin Von Soosten, Jeremy S. Yodh, Daniel Sherman, Brian Tarasinski, Michael Wimmer, Erik Johnson, Mingtang Deng, Jesper Nygård, Thomas Sand Jespersen, Charles M. Marcus, and Peter Krogstrup. Engineering hybrid epitaxial inassb/al nanowires for stronger topological protection. *Physical Review Materials*, 2(4), 2018.
- <sup>73</sup> Jie Shen, Sebastian Heedt, Francesco Borsoi, Bernard Van Heck, Sasa Gazibegovic, Roy L. M. Op Het Veld, Diana Car, John A. Logan, Mihir Pendharkar, Senja J. J. Ramakers, Guanzhong Wang, Di Xu, Daniël Bouman, Attila Geresdi, Chris J. Palmstrøm, Erik P. A. M. Bakkers, and Leo P. Kouwenhoven. Parity transitions in the superconducting ground state of hybrid insb–al coulomb islands. *Nature Communications*, 9(1), 2018.
- <sup>74</sup> M J L Sourribes, I Isakov, M Panfilova, and P A Warburton. Minimization of the contact resistance between inas nanowires and metallic contacts. *Nanotechnology*, 24(4):045703, 2013.
- <sup>75</sup> Tudor D. Stanescu, Roman M. Lutchyn, and S. Das Sarma. Dimensional crossover in spin-orbit-coupled semiconductor nanowires with induced superconducting pairing. *Physical Review B*, 87(9), 2013.
- <sup>76</sup> Boris V. Svistunov, Egor S. Babaev, and Nikolay V. Prokof'Ev. *Superfluid States of Matter*. CRC Press, 2015.
- <sup>77</sup> C. Thelander, T. Mårtensson, M. T. Björk, B. J. Ohlsson, M. W. Larsson, L. R. Wallenberg, and L. Samuelson. Single-electron transistors in heterostructure nanowires. *Applied Physics Letters*, 83(10):2052–2054, 2003.
- <sup>78</sup> M. Tinkham. *Introduction to Superconductivity*. Dover Books on Physics. Dover Publications, INC, Mineola, New York, 2 edition, 2004.
- <sup>79</sup> Michael Tinkham. *Introduction to superconductivity*. 1996.
- <sup>80</sup> M. T. Tuominen, J. M. Hergenrother, T. S. Tighe, and M. Tinkham. Even-odd electron number effects in a small superconducting island: Magnetic-field dependence. *Physical Review B*, 47(17):11599–11602, 1993.
- <sup>81</sup> B. Van Heck, R. M. Lutchyn, and L. I. Glazman. Conductance of a proximitized nanowire in the coulomb blockade regime. *Physical Review B*, 93(23), 2016.
- <sup>82</sup> Vlatko Vedral. Quantum entanglement. *Nature Physics*, 10(4):256–258, 2014.
- <sup>83</sup> Alexandros Vekris. *Supercurrent and Screening of Spins in a Double Quantum Dot Josephson Junction*. Masters thesis, Niels-Bohr Institute, 2018.

- 
- <sup>84</sup> Alexandros Vekris, Juan Carlos Estrada Saldaña, Joeri de Bruijkere, Sara Loric, Thomas Kanne, Mikelis Marnauza, Dags Olsteins, Jesper Nygård, and Kasper Grove-Rasmussen. Asymmetric little–parks oscillations in full shell double nanowires. *Scientific Reports*, 11(1):19034, 2021.
- <sup>85</sup> Alexandros Vekris, Juan Carlos Estrada Saldaña, Thomas Kanne, Mikelis Marnauza, Dags Olsteins, Furong Fan, Xiaobo Li, Thor Hvid-Olsen, Xiaohui Qiu, Hongqi Xu, Jesper Nygård, and Kasper Grove-Rasmussen. Josephson junctions in double nanowires bridged by in-situ deposited superconductors. *Physical Review Research*, 3(3), 2021.
- <sup>86</sup> Sagar Vijay and Liang Fu. Teleportation-based quantum information processing with majorana zero modes. *Physical Review B*, 94(23), 2016.
- <sup>87</sup> Hao Zhang, Önder Gül, Sonia Conesa-Boj, Michał P. Nowak, Michael Wimmer, Kun Zuo, Vincent Mourik, Folkert K. De Vries, Jasper Van Veen, Michiel W. A. De Moor, Jouri D. S. Bommer, David J. Van Woerkom, Diana Car, Sébastien R Plissard, Erik P.A.M. Bakkers, Marina Quintero-Pérez, Maja C. Cassidy, Sebastian Koelling, Srijit Goswami, Kenji Watanabe, Takashi Taniguchi, and Leo P. Kouwenhoven. Ballistic superconductivity in semiconductor nanowires. *Nature Communications*, 8(1), 2017.
- <sup>88</sup> Zhi Zhang, Ping-Ping Chen, Wei Lu, and Jin Zou. Defect-free thin inas nanowires grown using molecular beam epitaxy. *Nanoscale*, 8(3):1401–1406, 2016.